DESIGN, ANALYZE AND CONTROL OF NOVEL STATOR-PM ELECTRICAL MACHINES

TIANTIAN SHENG

PhD

The Hong Kong Polytechnic University

2018

The Hong Kong Polytechnic University

Department of Electrical Engineering

Design, Analyze and Control of Novel Stator-PM Electrical Machines

Tiantian Sheng

A thesis submitted in partial fulfilment of the requirements for the degree of Doctor of Philosophy

March, 2018

CERTIFICATE OF ORIGINALITY

I hereby declare that this thesis is my own work and that, to the best of my knowledge and belief, it reproduces no material previously published or written, nor material that has been accepted for the award of any other degree or diploma, except where due acknowledgement has been made in the text.

_____(Signed)

Tiantian Sheng_____(Name of student)

Abstract

Stator-PM machines have advantages in long track linear motion and in harsh environment applications, since they apply the robust rotor without PMs or windings. Generally, there are four types of stator-PM machines, naming double salient machine, flux reversal machine, flux switching machine and stator-PM Vernier machine. It is found that there are some common characteristics existing in stator-PM machines. Firstly, it is found that the winding flux in some stator-PM machines is biased. Secondly, some staor-PM machines apply the short-circuit or open-circuit equivalent magnetic path. Thirdly, it is found that the torque density for most of the stator-PM machines is relatively lower than rotor-PM machines. So in this thesis, these three topics are addressed. The main contribution of this thesis is listed as below, 1) developing novel biased flux machines based on biased flux characteristic, 2) developing doubly complementary machines to avoid open-circuit or short-circuit magnetic path, 3) exploring new topologies with torque density higher than conventional rotor-PM machines for low speed applications.

The biased flux actually is the unique characteristic for stator-PM machines. Since the exciting flux is biased, the biased current can be used to modulate the exciting field and generate the torque. Based on this characteristic, the research about biased flux machine design, analyze and control is chapter 2. Firstly, the definition of biased flux machine is given. Secondly, a set of biased flux machines have been developed. Two methods have been proposed to design and analyze the biased flux machines, which are magnetic path construction method and magnetic field modulation method. One NNSS 12/11 biased flux machine have been designed and built. The detailed performances such as back-EMF, electromagnetic torque, cogging torque and efficiency have been tested. One novel control based on zero-sequence current is also developed. It is verified that with this control, the speed range of the prototype can be expanded as 1.6 times. Meanwhile, the concept of transferring other machines such as electrical exciting and hybrid exciting machines into biased flux machines to remove the DC exciting windings is also proposed and demonstrated.

To overcome the disadvantages of the machines with open-circuit or short-circuit magnetic path, a new type of stator-PM doubly complementary machines (DCMs) are proposed. These machines have two complementarities as one exists in complementary rotors and the other exists in the basic units belonging to same phases. The first one applies the complementary rotors to construct a consecutive switching path for permanent magnet exciting flux, so that shorted or open magnetic path is avoided to reduce cogging torque and improve PM utilization. The second one is designed to reduce back-EMF harmonics and improve the torque density. The topology, working principle, characteristics and design methodology for DCMs are presented. Simulation and experiments are conducted for a 12/11(stator teeth/rotor teeth) DCMs to evaluate its performance and verify this design methodology. It is revealed that this machine could obtain good sinusoidal back-EMF waveform, small torque ripple and high PM utilization factor due to the doubly complementary characteristic. By transferring the doubly complementary idea into disc machines, a novel disc machine is also proposed for direct drive application. It is shown that the torque density of machine is high and the efficiency is more than 90% at rated speed.

To further improve the torque density of stator-PM machines, one novel kind of Vernier machines with consequent-pole PMs in slots is proposed in Chapter 4 and the influence of different combinations of rotor

and winding poles is compared. These machines have the paralleled magnetic path, which means the armature field will not pass through PMs. So the risk of demagnetization is eliminated and the armature reaction is intensified to improve the torque. Meanwhile, the simple structure makes these machines mechanically reliable and endurable. The principle of the proposed machines is introduced and the combinations of different winding and rotor poles are discussed. One prototype with 24 slots, 2 winding pole-pairs and 22 rotor pole-pairs has been built and tested. The results show that the torque density for prototype could reach 3 Nm/kg under nature cooling condition and the efficiency could get higher than 90%. Meanwhile, the total harmonic distortion (THD) for back electromotive force (back-EMF) is only about 5%, cogging torque is only about 0.8% and electromagnetic torque ripple is merely 5%. The comparion of this prototype with industrial applied fractional slot concentrated winding permanent magnetic machine is presented. It is shown that this stator-PM machine has 10.5% higher torque density.

In to further improve the torque density of stator-PM machines, one novel dual-PM excitation Vernier machine with short-pitch distributed-windings was studied in Chapter 5. The special parallel magnetic path constructed by the dual-PM structure could increase the equivalent permeance of the air-gap to better utilize the magnetomotive force (MMF) for torque improvement. The distributed-winding could increase the electrical gear ratio of the machine for speed scaling-down and torque turning up. Meanwhile, the short- pitch coils are applied to eliminate back-EMF harmonics to reduce torque ripple. The principle and characteristics of the proposed machine are introduced in detail. Some essential issues such as the torque percentages contributed by the excitation field harmonics, the effect of the shot-pitch coils and the torque comparison of dual-PM Vernier machine with conventional rotor-PM Vernier machines are introduced. The tested prototype has shown that this machine has good potential for direct-drive application as the torque density could reach 6 Nm/kg under nature ventilation, the total harmonic distortion (THD) for back-EMF is less than 4%, the torque ripple is less than 4% and the efficiency is about 90% under rated speed.

Keywords: Stator-PM machines, biased flux machines, doubly complementary machines, stator-PM Vernier machines, dual-PM exciting machines.

Publications arising from the thesis

[1] T. Sheng and S. Niu, "Design of Doubly Complementary Stator-PM Machine with High Magnet Utilization Factor for Low Cost Applications," *IEEE Trans.Energy. Convers.*, vol. PP, no. 99, pp. 1-1.

[2] T. Sheng, S. Niu, W. Fu and Q. F. Lin, "Topology Exploration and Torque Component Analysis of Double Stator Biased Flux Machines Based on Magnetic Field Modulation Mechanism," *IEEE Trans.Energy. Convers.*, vol. PP, no. 99, pp. 1-1.

[3] T. Sheng, S. Niu and S. Yang, "A Novel Design Method for the Electrical Machines With Biased DC Excitation Flux Linkage," *IEEE Trans.Magn.*, vol. 53, no. 6, pp. 1-4, June 2017.

[4] T. Sheng, S. Niu and W. N. Fu, "A novel design method for the electrical machines with biased DC excitation flux linkage," *2016 IEEE Conference on Electromagnetic Field Computation (CEFC)*, Miami, FL, 2016, pp. 1-1.

[5] T. Sheng, S. Niu and W. N. Fu, "A novel disc machine with axial biased flux and complementary salient rotors," *2016 IEEE Conference on Electromagnetic Field Computation (CEFC)*, Miami, FL, 2016, pp. 1-1.

[6] T. Sheng and S. Niu, "Design and analysis of novel double stator biased flux machines," *2016 Eleventh International Conference on Ecological Vehicles and Renewable Energies (EVER)*, Monte Carlo, 2016, pp. 1-10.

[7] T. Sheng, S. Niu, "A Novel Zero-Sequence-Current Based Dual-Stator Biased-Flux Machine for Electric Vehicles" *IEEE Trans.Energy. Convers.*, under revision.

[8] T. Sheng, S. Niu and W. Fu, "Design and Comparison of Slot-PM Consequent Pole Vernier Machines with Paralleled Magnetic Path" *IEEE Trans. Ind. Electron.*, under review.

[9] T. Sheng, S. Niu, "Design and Experimental Verification of Robotic Used Dual-PM Vernier Machine with Short-pitched and Distributed Stator Winding" *IEEE Trans.Energy. Convers.*, under review.

Acknowledgements

With time flying, my PhD program is coming to the end. At the moment I am going to finish this thesis, I want to give my appreciations to the people and organizations which have helped me wholeheartedly.

Firstly, thanks for my supervisors Professor Niu Shuangxia and Professor Fu Weinong. It is you gave me the platform to conduct my research and direct my exploration in the machine design and analysis.

Secondly, sincere appreciations are delivered for Hong Kong government, PolyU and Hong people. Thanks for the strong supports for my PhD program, as I can put all of my energy in the academic research without financially burden.

Thirdly, thanks for my family and my friends, your company and encouragement are the power source for my electrical machine research.

Fourthly, thanks for the mental tutors I meet in my life journey, my high school class adviser Song Bing, master program supervisor Wang Xiaolin and senior fellow apprentice Liu Lei. Your spirit will direct me in my left whole life.

Wish all of you have a bright career and happy life. Sincerely.

For the memory of this unforgettable time.

Tiantian Sheng, March, 2018.

Table of contents

Figure List

Table List

Chapter 1 Introduction

In this chapter, firstly, the backgrounds of stator-PM machines are presented to demonstrate the significance of this research. In which, the development for this kind of machines are introduced in detail. Secondly, the research strategy and main contents of this thesis are listed.

1.1 Backgrounds of this Research

1.1.1 Development of Stator-PM Machines

Electrical machines (EM) have been developed for more than 200 years, various machines with different structure have been proposed. According to different classification criteria, the commonly used machines can be divided into different groups. For example, according to the drive model, EMs can be identified as DC motors and AC motors [1]-[2]. According to the stator and rotor flux rotation velocity, EMs can be classified as asynchronous machines and synchronous machines [3]-[4]. According to the permanent magnet (PM) material, electrical machines can be divided as PM machines and non-PM machines [5]-[6]. According to the position of the PM, permanent magnet machines can be divided into two categories, namely rotor-PM and stator-PM machines [7]-[8]. In recent years, due to the development of the high performance permanent magnet materials such as rare-earth and neodymium iron boron (NdFeB), permanent magnet electrical machines got rapid developed. Electrical machines have been used widely in industrial and daily life applications [9]-[10].

For traditional distributed winding permanent magnet synchronous machines (PMSMs), leakage magnetic flux is small, back-EMF is good sinusoidal waveform, utilization rate of permanent magnet and efficiency is high, which almost can satisfy all application requirements. However, it come to the liner moving applications or severe situations with huge vibration, PMSM lost its priority since the long track with PM mounted will cost huge and the rotor with PM on can not sustain heavy vibration.

To overcome these disadvantages, stator-PM machines have been widely investigated. There are mainly four types of stator-PM machines, which are double salient machines (DSMs), flux reversal machines (FRMs), flux switching machines (FSM) and stator-PM Vernier machines. The development history and trend of these four kinds of machines are presented by followings.

1) Double Salient Machine

Double salient machines are one kind of brushless machine, which firstly appeared in 1990s [11]. The structure of first double salient machine is shown in Fig. 1. 1. This machine has two pieces of PMs installed in the stator yoke and applies concentrated windings. The rotor is simple laminations without PM or windings, which is low-cost and robust, so this machine can endure severe vibrations.

The exciting flux created by stator PM links with three phase windings consecutively, so the variable flux could generate the alternative back-EMF in the windings. With injecting of rvarious current, this machine could produce constant torque. Since the exciting flux can be switched from one phase to another

consecutively, the leakage flux is small and the PM utilization factor is high [12]-[15]. Double salient machines are suitable for direct drive application since they can be designed with large number of poles.

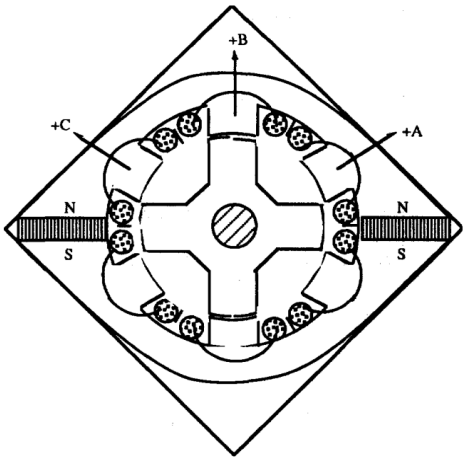

Fig. 1. 1. The first double salient permanent magnet machine in [11].

Currently, the researches about double salient machines mainly focus on the following aspects. First one is to explore new topologies to further improve the torque density. Generally, four strategies have been applied, as 1) selecting different combinations of stator and rotor teeth, 2) using double stators to improve the space utilization, 3) transferring PMs from stator into rotor.

In [16] and [17], two new double salient machines are proposed. Fig. 1. 2(a) shows the symmetric teeth 12/8 (stator teeth/rotor teeth) double salient machine and Fig. 1. 2(b) presents the asymmetric teeth 12/8 double salient machine. Comparing with the original 6/4 structure, the 12/8 structure has large equivalent permeance and the short magnetic path, so the torque density could be improved. Specially, it is pointed in [17] that some novel techniques such as asymmetric current can be used for drive the asymmetric teeth double salient machines to further increase the torque density.

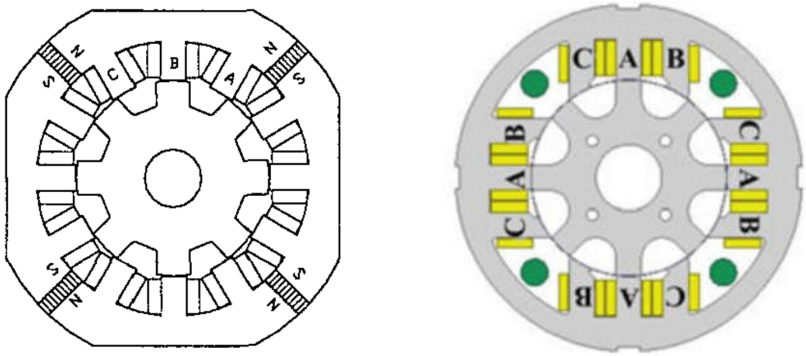

(a) Symmetric teeth in [16] (b) Asymmetric teeth in [17]

Fig. 1. 2. 12/8 double salient permanent magnet machine.

In [18], the other technique, saying using double stators is used to improve the performance of double salient machines. Fig. 1. 3 (a) shows the structure with surface-mounted-PM inner stator and Fig. 1. 3 (b) shows the one with inserted-PM inner stator. In these machines, the single stator is separated into two, so the space could be better used. Obviously, comparing with single stator machine shown in Fig. 1. 2, the space for the PM has been improved significantly, so the excitation field is thus strengthened, the torque is

improved. Meanwhile, with PMs moved away from the windings, the heat dissipation condition can also be improved, since the heat generated in PMs and in windings is separated mechanically by using two stators. It is reported that with double stator, the torque density for double salient permanent magnet machines could be significantly in [18].

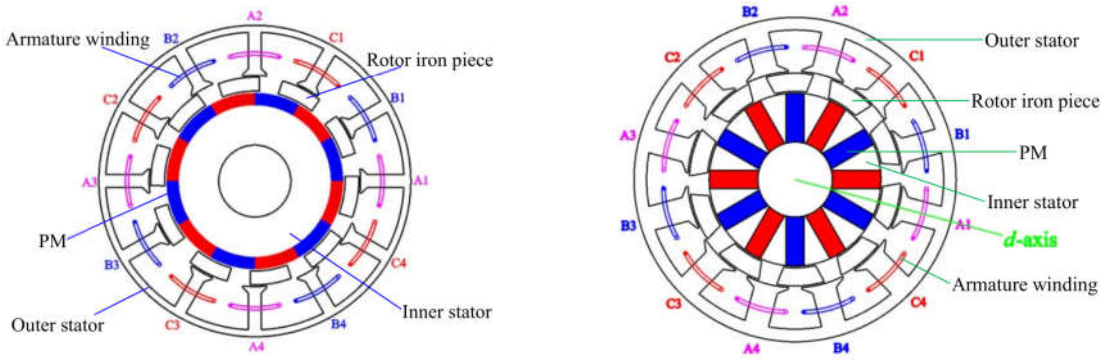

(a) Surface-mounted PM in inner stator in [18] (b) Inserted-PM in inner stator in [18]

Fig. 1. 3. Double stator double salient permanent magnet machine.

The third strategy to improve the torque density of double salient machines is to move the PMs from stator to rotor. Ref [19] and Ref [20] have given two examples. It is acknowledged that the torque density for stator-PM double salient is lower than rotor-PM synchronous machines. The key value for double salient machine lies on the stator-PM structure, which can make the rotor solid and robust to work in harsh conditions. If the PMs are moved from the stator to rotor, these machines actually are changed into salient-assistant permanent magnet synchronous machines. The advantages of stator-PM machines are removed, meanwhile, the torque density for these special rotor-PM machines seems have no advantages over traditional surface-mounted PM or inserted-PM synchronous machines. So strictly, these special rotor-PM machines do not agree with the traditional definition of double salient machines. And the merits of these machines are not significant comparing with stator-PM double salient machines or with the rotor-PM synchronous machines.

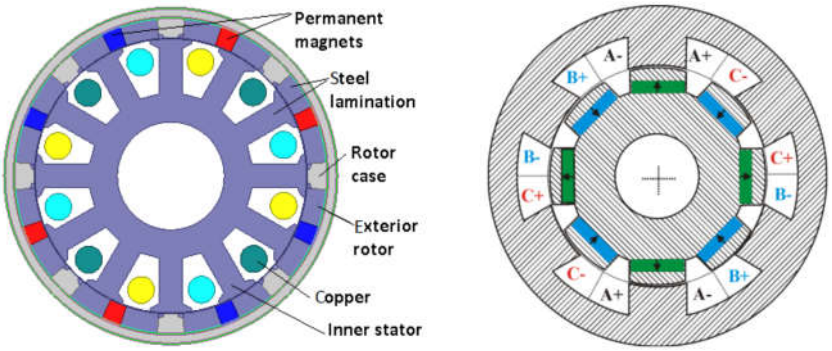

(a) Topology proposed in [19] (b) Topology proposed in [20]

Fig. 1. 4. Rotor-PM double salient permanent magnet machine.

Besides improving the torque density, on the other perspective, many literatures focus on improving the flux weakening capability. In [21]-[23], hybrid exciting double salient is proposed. Fig. 1. 5(a) shows the hybrid exciting solution for traditional 6/4 structure double salient machine, Fig. 1. 5(b) shows the hybrid exciting solution for one slot-PM double salient machine and Fig. 1. 5(c) shows the novel solution for one

asymmetric double salient machine.

Different from the rotor-PM machines, the relative position of the PMs and the windings are fixed, so the polarity of the flux induced in the windings has uni-polar feature. Under this condition, the DC winding could be added to modulate the exciting flux in the windings. In rotor-PM machines, since the flux in windings alters with the rotor position, it is difficult to develop the hybrid exciting techniques. As a result, the speed range for stator-PM machines is much larger than the rotor-PM machines due to the flexible flux weakening methods. Flexible flux weakening method including negative d-axis current or hybrid exciting is another advantage of stator-PM machines.

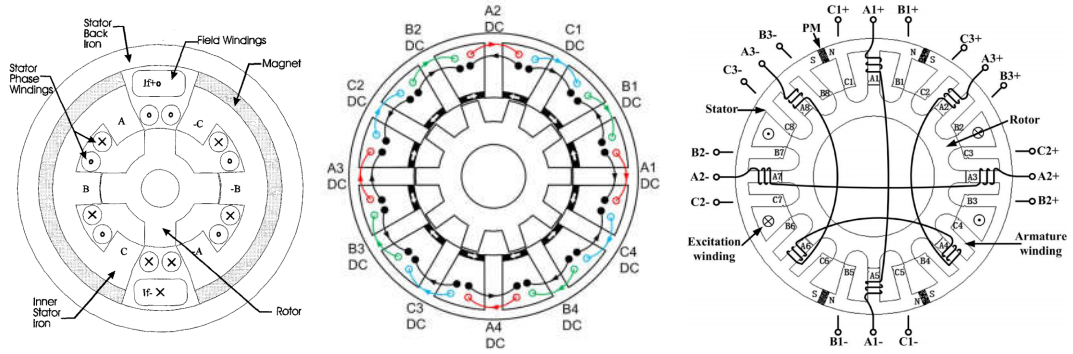

(a) For traditional 6/4 structure in [21] (b) For slot-PM structure in [22] (c) For asymmetric structure in [23]

Fig. 1. 5. Hybrid exciting double salient permanent magnet machine.

In hybrid exciting techniques, the additional DC coils will conflict the AC windings and cause additional copper loss. To solve this, in [24], the memory magnet is applied to modulate the exciting flux. It is introduced that the operating point of the memory magnet could be adjusted, so the flux weakening capability could be improved and the copper loss could be reduced. However, in real operation, the memory magnet is difficult to control. Usually, the exciting current needed to change the working point of the magnet is huge, which may exceed the capacity of the power converters. Meanwhile, it is difficult to adjust the working point of the magnetic when the machine is running. It is hard to maintain the constant torque or speed when huge current is injected to adjust the working point of the material. So this technique still has challenges in industrial applications.

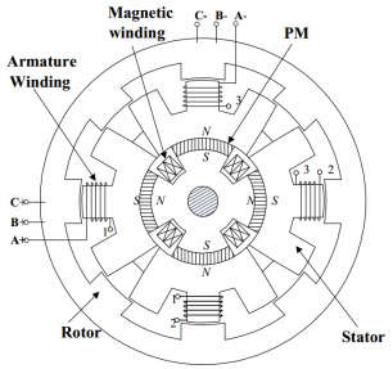

Fig. 1. 6. Double salient permanent magnet machine with memory magnet in [24].

Here is the summary for double salient machines. These machines can switch the exciting flux from one phase to the other smoothly, so the leakage flux is small and the PM utilization is high. Meanwhile, the rotor is solid and robust salient structure, which makes these machines suitable for harsh working

conditions.

On the other hand, the major disadvantage for traditional double salient machine is the asymmetric flux path, which is the inherent characteristic of double salient machines. Since there are three stator teeth between the adjacent PMs, the distance from PMs to each stator teeth could not be even. This causes the asymmetric back-EMF and inductance for three phases, making great harmonics for the output torque. It worth mentioning that in some novel double salient machines, the asymmetric magnetic path is avoid, however, the exciting flux switching way is different from the traditional double salient machines, which actually make them lose the torque density or PM utilization.

2) Flux Reversal Machine

Flux reversal machine is another stator-PM machine, which was proposed and named in 1996 [25]. The predecessor of flux reversal machine is one single-phase alternator proposed in [26]. Interesting, this alternator is named flux-switching alternator, not the flux-reversal alternator. Actually, this stator-PM alternator could be regarded as the predecessor of all the stator-PM machines, including the above introduced double salient machines, flux reversal machines and the flux switching machines. The basic principle of stator-PM machine is to construct the magnetic path to obtain the varied permeance along air-gap, so the windings could induce back-EMF to conduct the mechanical-electrical energy conversion. The PM location is the main characteristic for the later researchers to define the type of stator-PM machines. In Fig. 1. 7, the PM location is very abstract, it is hard to determine whether the PMs are inserted in the yoke or mounted on the teeth. So this alternator is the predecessor of all the stator-PM machines.

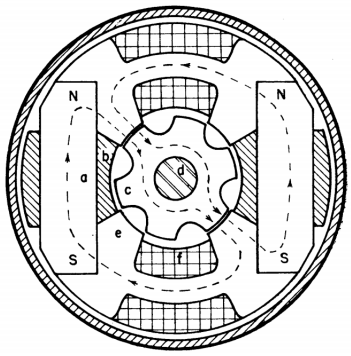

Fig. 1. 7. Predecessor of flux reversal machines in [25].

Fig. 1. 8 shows the primitive flux reversal machine, in which Fig. 1. 8(a) is the single phase structure in [27] and Fig. 1. 8(b) is the three phase structure in [28]. After that, the clear concept of flux reversal is set, as flux reversal machine means the machine with the PMs mounted on the surface of the stator teeth. Specifically, there are two pieces of PM with opposite polarity mounted on one stator teeth.

Different from the double salient machines, flux reversal machines have the symmetrical magnetic path and the sinusoidal back-EMF waveforms. In drive mode, this kind of machine has advantages than the traditional double salient machines. Meanwhile, since the PMs are mounted on the teeth, the space of PM for flux reversal machine is larger than double salient machine, so the torque density for flux reversal machine could get higher theoretically.

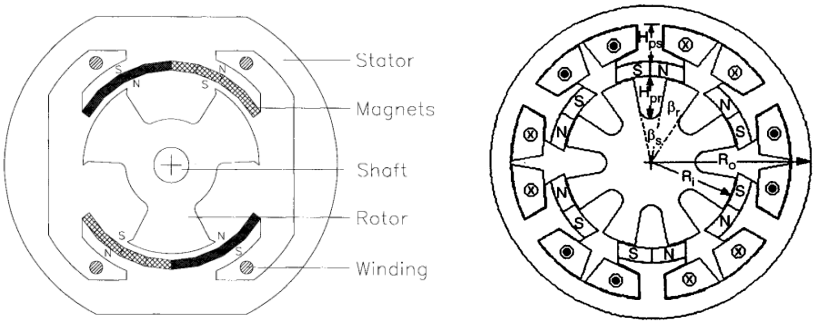

(a) Single phase flux reversal machine in [27]. (b) Three phase flux reversal machine in [28].

Fig. 1. 8. Primitive flux reversal machines.

Simply looked at the structure of flux reversal machines, it seems lack of diversity, as two pieces of PMs have to be mounted on one stator teeth. So comparing with other traditional stator-PM machines, such as the double salient machines or the flux switching machines, flux reversal machines did not draw much attention in last decades. The literatures about flux reversal machines are much rare than the other stator-PM machines. However, in recent year, the advantages of this kind of machines are rediscovered and many new theory and topologies of flux reversal machines are proposed. The performances of flux reversal machines have been improved significantly and it is believed these machines have advantages in linear motion applications.

Currently, the research of flux reversal machines mainly focus on the following aspects: 1) developing novel topologies for torque improvement, 2) studying on new winding pattern, 3) application on linear motions, 4) reducing cogging torque.

Speaking of the new topology for flux reversal machine, generally the following three techniques are applied. Firstly, change the way of locating PMs on the stator teeth, secondly, change the number of PM pieces on the stator and thirdly, use the partitioned stators. Additionally, some topologies may use more than one of the mentioned techniques.

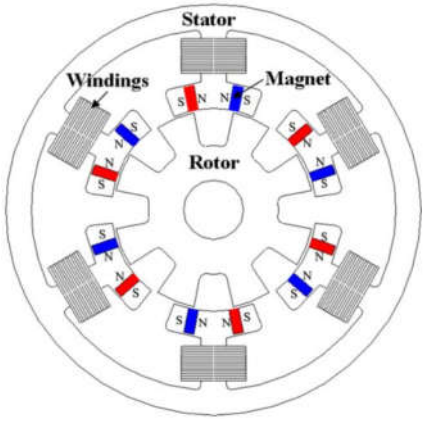

Fig. 1. 9. Using inserted PMs for flux reversal machine in [29].

Fig. 1. 9 shows the machine using inserted PMs proposed in [29], where the mounted PMs are changed into inserted in the stator teeth. Actually, this small technique is very practical in improving the torque density of flux reversal machines. In traditional flux reversal machines, the armature magnetic field produced by windings has to pass through the PMs to construct the loop. It is known that the permeance of

the PMs is very small, so the equivalent air-gap for the armature field is very large. Under this inserted way, the armature field has another path to form the loop without passing through the PMs. So the magnetic density in the air-gap could be strengthened and the torque could be increased accordingly. The details about this paralleled magnetic path will be introduced in chapter four, where the studied stator-PM Vernier machine applies the same principle. However, the paralleled magnetic path will cause the low power factor since the inductance value is increased. The trade-off of torque and power factor should be considered in this PM-inserted design.

Fig. 1. 10 demonstrates the strategy of changing PM pieces of stator teeth for flux reversal machines. Fig. 1. 10 (a) is one 6/14 flux reversal machine proposed in [30] and Fig. 1. 10 (b) is one 12/28 flux reversal machine introduced in [31]. It is seen that the PM pieces on stator teeth have been changed from 2 to 4, and the stator/rotor teeth combinations have been modulated. It is interesting to find that with this configuration, the flux reversal machines have the very similar structure with the magnetic field modulated machines. The ultimate version of the PM pieces changing strategy leads the evenly distributed PM flux reversal machine shown in Fig. 1. 10 (c) [32]. Actually, from the magnetic field modulated perspective, the machine shown in Fig. 1. 10 (c) is definitely one magnetic field modulated machine. The stator teeth and rotor teeth serves as the modulators. After modulation, the exciting magnetic field produced by the PMs could be modulated to have the same pole-pair with the winding poles. Actually, flux reversal machine is one special magnetic field modulation machine with uneven distributed PMs. This theory has been well developed in [33] to [35].

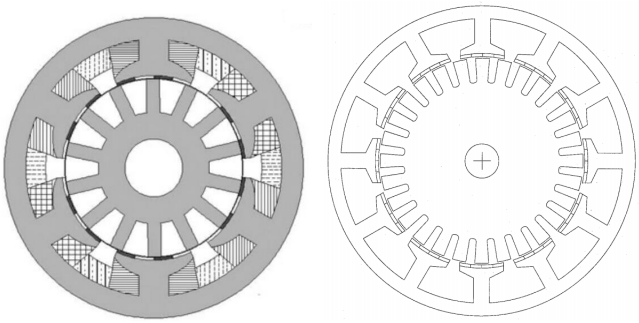

(a) 6/14 flux reversal machines in [30]. (b) 12/28 flux reversal machine in [31].

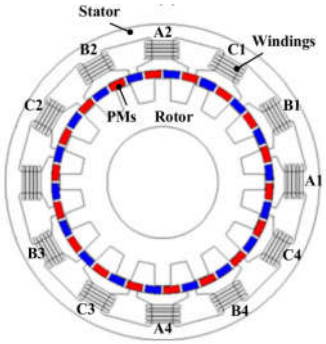

(c) Evenly distributed PM flux reversal machine in [32.]

Fig. 1. 10. Changing PM pieces on stator teeth for flux reversal machine.

Fig. 1. 11 shows the technique of using partitioned stator to further improve the torque density of flux reversal machine in [36]. The advantage of this method has been introduced above in double salient

machines as it can help to increase the space for PM and improve the heat dissipation condition. The PMs mounted on the surface of the inner stator could also be changed as inserted way. And the structures mentioned in Fig. 1. 10 also can be changed in this way.

The drawback of the partitioned stator is that it is difficult to build. The separated rotors are hard to be connected together. Even in some special way, the mechanical robust of these machines are very low. So up to now, these structures still have challenge in industrial applications.

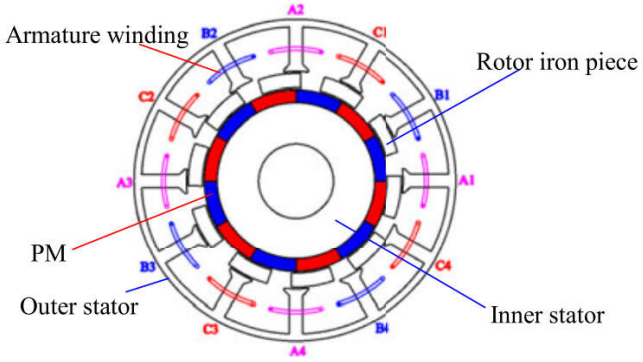

Fig. 1. 11. Using partitioned stators for flux reversal machine in [36].

Fig. 1. 12 shows the way of using the combined techniques to improve the performance of the flux reversal machines. Fig. 1. 12(a) is one partitioned stator flux reversal machine with consequent PM poles [37] and Fig. 1. 12(b) shows the one with inserted multiple PMs on stator teeth [31]. For the machine with consequent pole, the utilization of PMs could be improved and the equivalent permeance of the magnetic path becomes greater. So basically, the torque will not be damaged and the flux weakening capability could be strengthened. For the machine shown in Fig. 1. 12(b), it is one equivalent split-teeth stator-PM Vernier machine but with unevenly distributed PMs. It has the similar performance with split-teeth Vernier machine and suitable for large torque low speed applications.

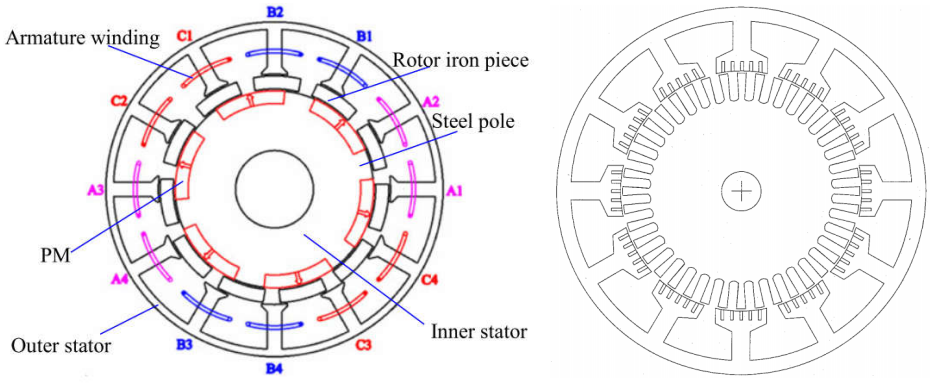

(a) Using partitioned stator and consequent pole PMs in [37]. (b) Using inserted multiple PMs on one stator teeth in [31].

Fig. 1. 12. Using combined techniques for flux reversal machine.

The other topic for flux reversal machine is to investigate the new winding configuration pattern to further improve their performance. Traditionally, flux reversal machines apply the concentrated windings. However, recently, it is found that distributed windings help to increase the torque density. Ref. [38] firstly proposed the idea of using distributed windings for flux reversal machine, Ref. [39] then follows and proposed one novel 6/14 flux reversal. It is reported that by simulation and experiment verifications, the

torque density for this distributed-winding flux reversal machine has 1.5 times of the traditional concentrated-winding flux reversal machine. Inspired by the distributed-winding idea, Ref. [40] proposed one special design method for flux reversal machine, which is based on the winding configuration. Fig. 1. 13 shows the different machine topologies could be developed by this design. Actually, the topologies shown in Fig. 1. 13(a) and in Fig. 1. 13(c) is not new, which is the traditional one and the exiting one shown in [30]. The contribution of Ref. [40] is that with the proposed method, the connection of these three topologies can be built and the fundamental principle could be found.

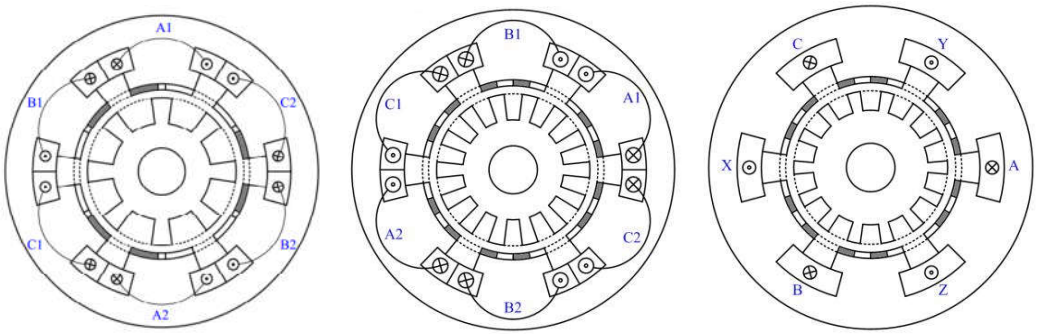

(a) Traditional structure in [30]. (b) 6/14 concentrated winding structure in [40]. (c) 6/14 distributed winding structure in [30].

Fig. 1. 13. Design flux reversal machines based on winding topology.

Ref. [41] compares the concentrated-winding flux reversal machines and the distributed-winding flux reversal machines. It is concluded under same rated power, the steel volume could be saved by 12% and the PM volume could be saved 34%. Ref. [42] studied the dq axis equivalent circuit for developing of better control strategy. Recently, Ref. [43] systematically investigated the winding paten and the combinations of the stator/rotor teeth for flux reversal machines. The common magnetization modes of flux reversal machines are proposed, the new machines with different winding patens and different combinations of stator/rotor teeth are proposed and analyzed, as shown in Fig. 1. 15.

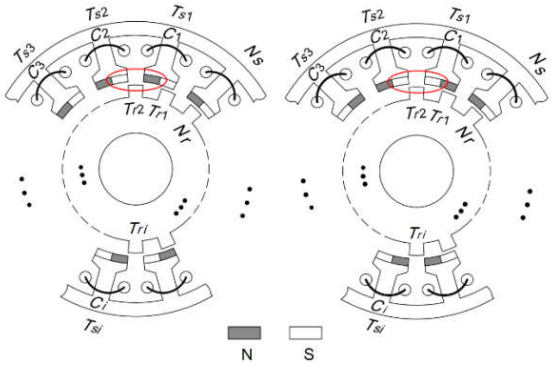

Fig. 1. 14. Common magnetization modes for flux reversal machines in [41].

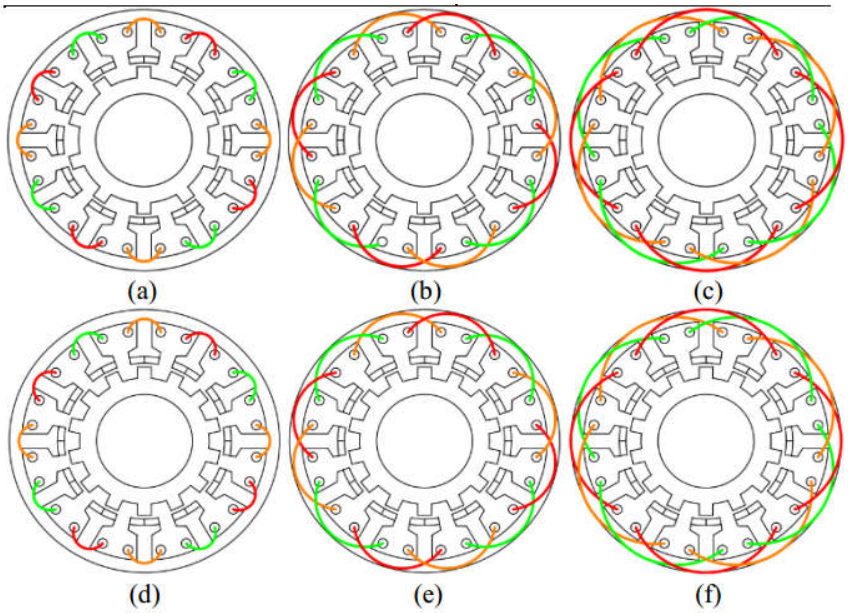

Fig. 1. 15. Different winding patens and combinations of stator/rotor teeth for flux reversal machines in [43].

Since flux reversal machines have PMs on stator, which are suitable to be used in linear motion applications. Many researchers have investigated the linear flux reversal machines. Typically, all the rotary machines mentioned above can be transferred into linear motor. Comparing with the rotor-PM machines, when the rotary machines are transferred into linear machine, the PMs will be placed on the mover, rather than on the stator. So in long travel linear applications, there is no need to cover the tracks with expensive PMs. This is the major advantage of stator-PM machines. Ref. [44] to Ref. [50] proposed many different kinds of linear flux reversal machines, and basically they are transferred from the introduced rotary flux reversal machines mentioned above. The following ones are selected as the examples to show this design.

Ref. [51] proposed the linear machine in Fig. 1. 16, which is transferred from Fig. 1. 8(b), Ref. [52] proposed the machine in Fig. 1. 17, which is transferred from Fig. 1. 10 (a) and Ref. [53] introduced the structure transferred from Fig. 1. 11. Generally, the linear machine works in the same principle with the rotary machines as the combinations of stator/rotor teeth and winding patens are the same. However, when rotary machine are transferred into linear machine, the end-effect should be well cared, as the end-effect will cause back-EMF distortion and cogging force. Some special techniques to deal with the end-effect usually are necessary when linear machines are designed.

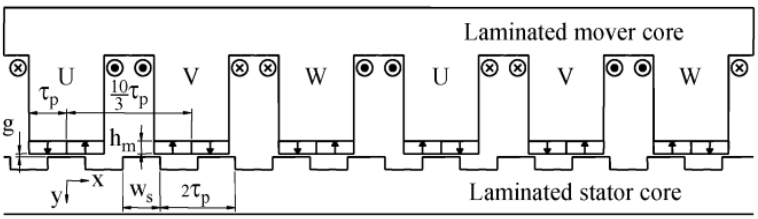

Fig. 1. 16. Linear machine transferred from Fig. 1. 8(b) in [51].

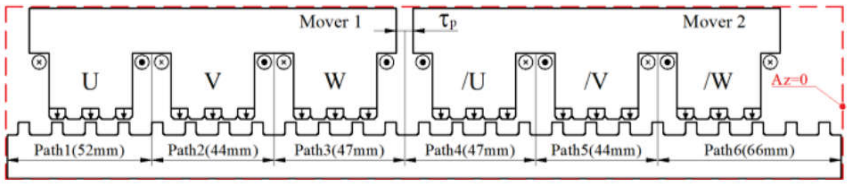

Fig. 1. 17. Linear machine transferred from Fig. 1. 10 (a) in [52].

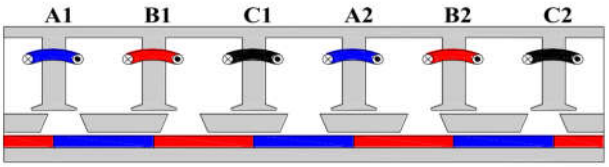

Fig. 1. 18. Linear machine transferred from Fig. 1. 11 in [53].

Cogging torque is another important issue for flux reversal machine. As the machines work with the variable permeance of the equivalent air-gap, in other words, working with salient effect, the cogging torque is much severe than rotor-PM machines. The techniques to reduce the cogging torque includes optimizing stator/rotor teeth shape, selecting better stator/rotor teeth combination, using skewed slots or poles [54]-[57]. These techniques are common ways to reduce cogging torque for all of machines, so they will be introduced here in detail.

3) Flux Switching Machine

Flux switching machine is another kind of stator-PM machines. Fig. 1. 19 shows the primitive flux switching machine, which is firstly proposed in [58].

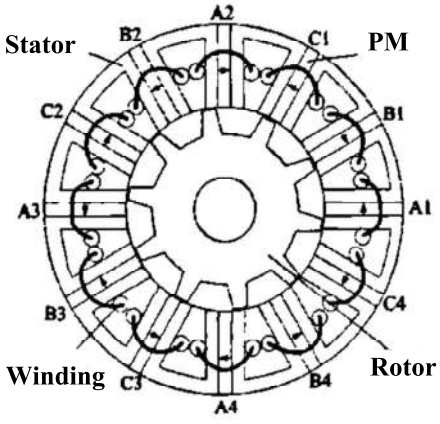

Fig. 1. 19. Primitive flux switching machine in [58].

Different from double salient machine or the flux reversal machines, flux switching machine has “C” core stator teeth and have PMs sandwiched between the cores. Obviously, the volume for PM in flux switching machine is much larger than the other stator-PM machines. So it may have stronger exciting field. On the other hand, it is noticed that the stator has been separated into many pieces, so the manufacturing difficulty for this machine is much larger than others. Flux switching machines have got much intensive attentions than the other stator-PM machines. The investigations of flux switching machine

fall into the following aspects, 1) exploring new topologies to improve the performance, 2) strengthening flux weakening capability, 3) reducing cogging torque, 4) study of linear flux switching machines, 5) comparative study of flux switching machine with magnetic field modulation machine.

Ref. [59] to Ref. [70] proposed the new topologies of flux switching machines and Fig. 1. 20 shows some of them. Fig. 1. 20 (a) shows one split-teeth flux switching presented in [59]. The split-teeth technique has also been used in other stator-PM machines such as flux reversal machines and double salient machines. The advantage of this technique is that it can increase the pole-pairs of the rotor, making the machine for low speed and high torque applications. Fig. 1. 20 (b) gives one novel flux switching machine with "V" shaped PM proposed in [60] . The flux concentrating effect produced by the "V" shape PMs helps to increase the torque density and efficiency of this machine. The other trend of developing new topologies is to apply double rotor or double stator structures. Ref. [61] gives the example of design flux switching machine with double rotor shown in Fig. 1. 20 (c), and Ref. [62] demonstrates the method to design double stator flux switching machine shown in Fig. 1. 20 (d). The advantage for these dual rotor or stator structure is that the space utilization can be increased thus the torque density or efficiency can be improved. The drawback is that the mechanical structure is too complicated, which is hard to build and has low reliability. The other aspect of the topology studying is the windings configuration. Ref. [63] proposed one with overlapping windings shown in Fig. 1. 20 (e) and Ref. [64] proposed one with four layer windings shown in Fig. 1. 20 (f).

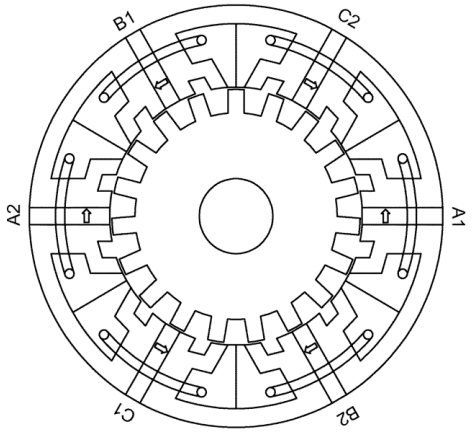

(a) With split teeth in [59].

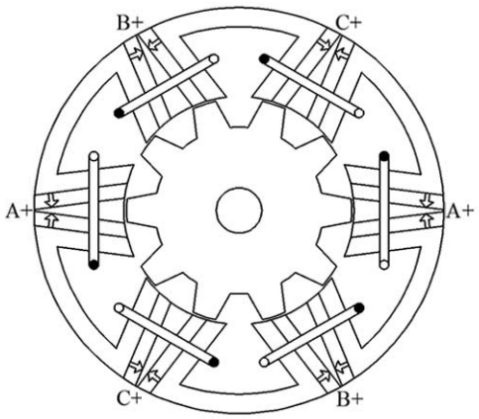

(b) With "V" shape PMs in [60].

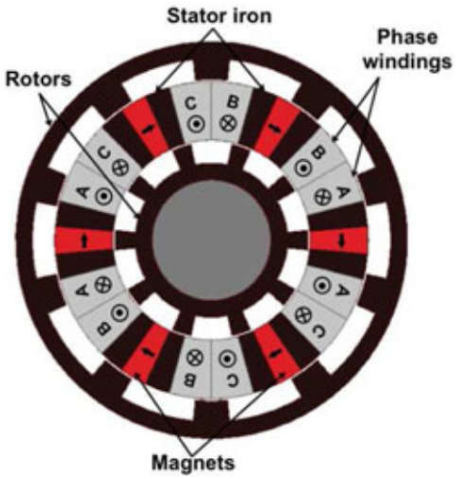

(a) With double rotor in [61].

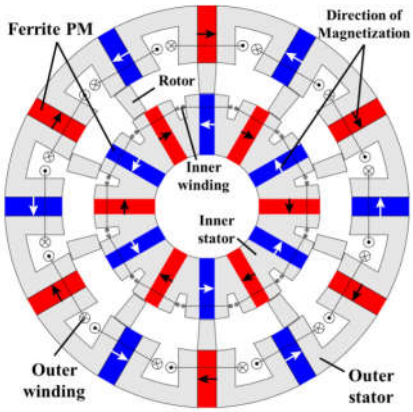

(b) With double stator in [62].

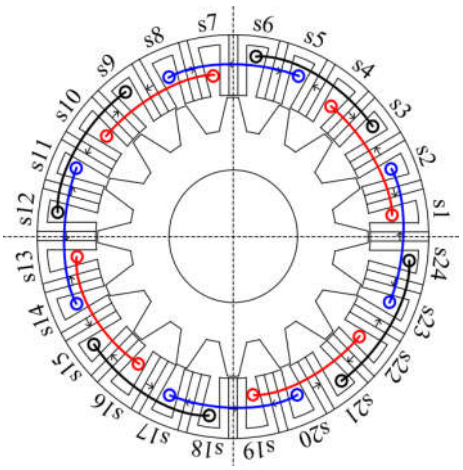

(e) With overlapping winding in [63].

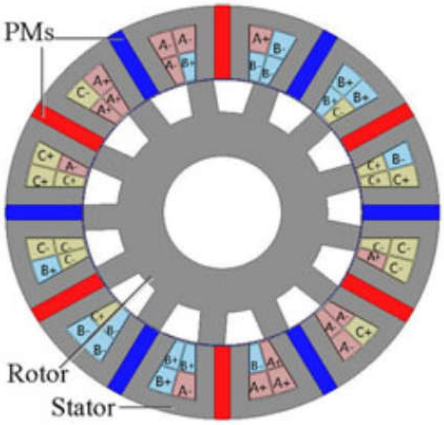

(f) With multi-layer winding in [64].

Fig. 1. 20. Novel topologies of flux switching machines.

To improve the flux weakening capability of flux switching machines, many hybrid excitation machines are studied [71]-[80]. These hybrid exciting machines have additional DC windings to adjust the exciting field, making the machines have wide speed range. The hybrid exciting machines are suitable for wide-speed range applications. However, comparing with the normal machines, the DC winding takes the valuable space for armature windings, and the DC windings may only be injected with current in short intervals, which make hybrid exciting machine has low torque density and efficiency. Meanwhile, the negative d-axis current can be used to adjust the exciting field. So in applications, the speed range and torque density should be balanced to determine whether hybrid exciting style should be used.

Similar to the double salient machine and the flux reversal machine, the cogging torque for flux switching machine is also one important research topic. Ref. [81] to Ref. [90] proposed many techniques to reduce cogging torque for flux switching machines, such as skewed teeth, better combination of rotor and stator teeth and optimized pole-shaping.

Linear flux switching machines have also been widely investigated in many literatures. Similar to the

flux reversal machines or the double salient machines, all the mentioned rotary flux switching machines can be adopted into linear machines. Ref. [91] to Ref. [100] gives some topologies of the linear flux switching machines. Basically, the performances of the linear flux switching machines have the similar characteristics of the rotary flux switching machines. The comparison of linear flux switching machines with other linear machines is equivalent to the comparison of rotary flux switching machines and the other rotary stator-PM machines.

Another interesting research topic of flux switching machine is the magnetic gear effect existing in this machine. It has been mentioned above that for the double salient machine, flux reversal machine and the flux switching machine, the primitive structure for them is same. So definitely, there should be one universal principle for them. Electric gear effect is the general theory to explain the operation principle of the stator-PM machines. Ref. [101] analyzed the magnetic gear effect in flux switching machine, Ref. [102] revealed the same principle in one partitioned stator flux switching machine, Ref. [103] compares the different flux switching machines with different winding configurations by using magnetic gear effect and Ref. [104] presented the general overview of the magnetically geared flux switching machines.

4) Stator-PM Vernier Machine

The newly developed stator-PM machine is another kind of stator-PM Vernier machines. Different from the other kinds of stator-PM machines, this machine is derived from the magnetic gear effect [105]-[106]. It works on the high order harmonics instead of the fundamental harmonic, which can be seen as a combination of magnetic gear and electrical machine. The earliest electromechanical device with Vernier concept is one resolver proposed in 1957, which could decouple the pole-pairs of winding and rotor. So it could be regarded as the predecessor of Vernier machine [107]. The first Vernier machine was proposed by C. H. Lee in 1963 [108], the basic principle is shown in Fig. 1. 21.

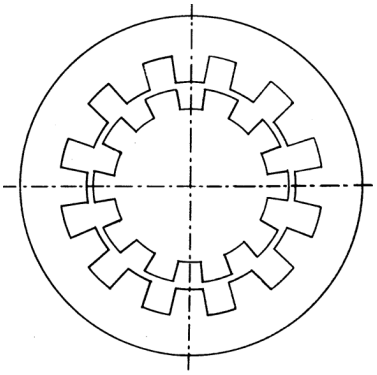

Fig. 1. 21. Structure of the first Vernier machines in [108].

It was the first time that “Vernier” was used to name a machine as it operates on the principle of a electrical gear that a small displacement of the rotor will produces a large displacement of the axes of the maximum and minimum permeance. It was stated that with the electrical gear effect, Vernier machines could scale down the speed and increase the torque. In the appended discussion, W. K. Koch pointed out the saturation of the yokes and teeth will limit the output of the torque, which made this machine with a confined gear effect. These two statements led the research of Vernier machine and pointed out its restriction. Afterwards, Prof. K. C. Mukherji compared power density of the Vernier machine with

induction motor in 1974, and it was concluded that Vernier machine has slightly higher power density than induction machine. But the improvement can not offset the increased cost of the control system [109]. This comparison was fair to show that the first Vernier machine operating with reluctance effect, namely without PMs or DC excitation winding, actually did not have much torque advantage than induction motor or DC motor. With the uncertain future, Vernier machines did not draw much attention at that age.

Twenty years later, it was rediscovered that the evolved Vernier machines with PM excitation or DC winding excitation could obtain much higher torque density than the initial Vernier reluctance machine. They even have higher torque density than popular PMSMs. Afterwards, Vernier machines have got great investigations. According to the excitation sources, Vernier machine can be divided into the following four categories, 1) electrical excitation type, 2) rotor-PM excitation type, 3) stator-PM excitation type and 4) dual-PM excitation type.

The electrically excitation Vernier machines actually have two categories, namely Vernier reluctance machine [107]-[109] and DC excitation Vernier machine [110]-[112]. Vernier reluctance machine works with the reluctance torque as the winding generates both excitation and armature fields, and the variation of the permeance is hence used to produce torque. But DC excitation Vernier machines mainly work with the electromagnetic torque, as the excitation field is actually modulated to couple with the armature field to generate torque. So it is found DC excitation Vernier machines have much higher torque density than the preliminary Vernier reluctance machines.

The first rotor-PM Vernier machine was proposed by A. Toba in 1999 [113]. It is interesting to see that Vernier machines could have the same structure with the conventional PMSMs, except the combination of the winding and PM poles. Afterwards, rotor-PM Vernier machines got rapid development due to its torque advantage. Ref. [114] to [115] presented novel topologies to further improve the torque density. Ref. [116] to [117] studied the dual-stator or dual-rotor Vernier machines. Ref. [118] to [119] investigated the consequent-pole Vernier machines to improve PM utilization factor and expand the flux weakening range.

The stator-PM Vernier machine is another kind of stator-PM machines. Different from the double salient machine, flux reversal machine and the flux switching machine, this kind of machine has not drawn much attention. Although Vernier machine is not the new concept, the literatures about stator-PM Vernier machine are still rare. Up to now, there are no more than twnety papers reported this and most of the papers are published in last two years.

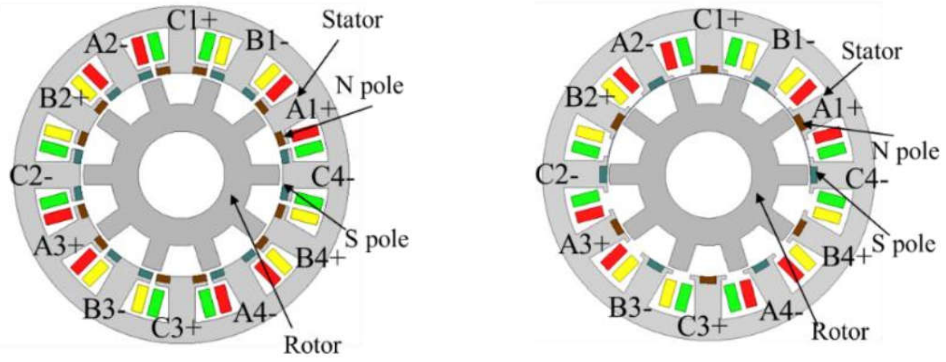

(a) PM inserted in side of the teeth in [120]. (b) PM inserted in the central of the teeth in [121].

Fig. 1. 22. Two kind of stator-PM Vernier machines.

Ref. [120] and Ref. [121] studied stator-PM Vernier machines shown in Fig. 1. 22. It is seen that these kinds of machines have the similar structure with flux reversal machine. The difference is the combinatiton of stator and rotor teeth. Flux reversal machines are developed from the salient machine based on the magnetic circuit analysis, but the Vernier machine is developed from the magnetic gear, the combinations of stator and rotor teeth agree with the magnetic gear principle.

The other aspect of stator-PM Vernier machine is the linear machines. It has been mentioned above that the stator-PM machines have advantages in long track linear motion. Ref. [122] introduced one high force density linear Vernier machine with concentrated windings, as shown in Fig. 1. 23. To eliminate the detent force, Ref. [123] proposed one double stator structure, as shown in Fig. 1. 24.

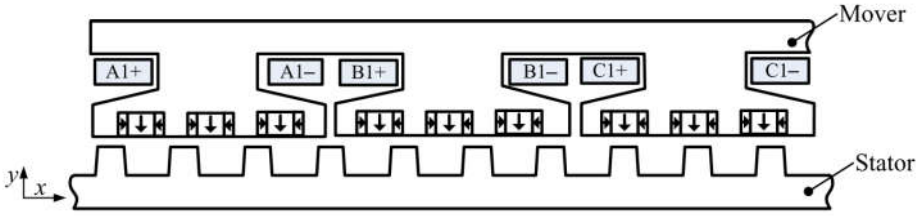

Fig. 1. 23. High force density linear Vernier machine in [122].

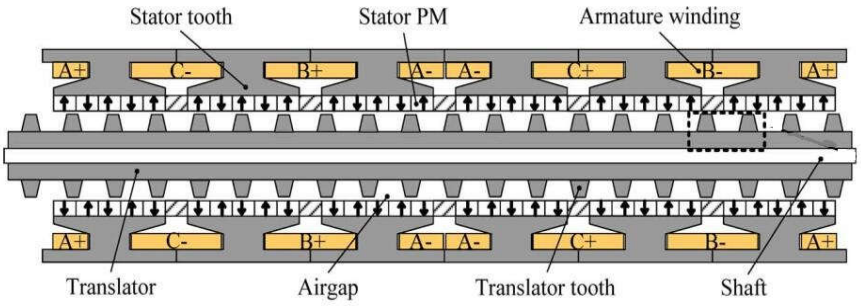

Fig. 1. 24. Linear stator-PM Vernier machines with double stator in [123].

To further improve the force density, Ref. [124] proposed the distributed winding stator-PM Vernier machine, as shown in Fig. 1. 25. With distributed winding, the pole-pairs of the winding became smaller, so the gear-ratio can be improved. The greater gear-ratio can improve the force density according to the magnetic gear effect theory.

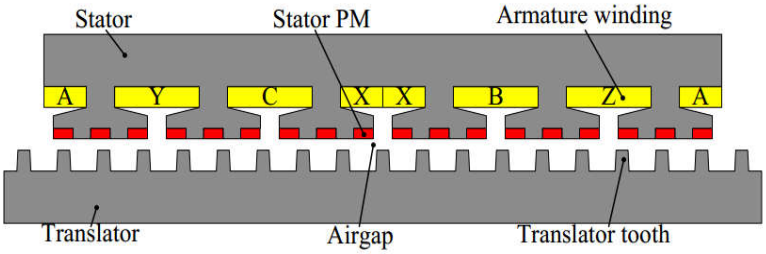

Fig. 1. 25. Linear stator-PM Vernier machines with single stator in [124].

Ref. [125] proposed one modular stator-PM Vernier machine. With the modular structure, the end-effect can be eliminated. So the back-EMF for three phase winding is symmetrical, the torque ripple can be reduced. The disadvantage for this structure is the complicated craft to connect the modular stator.

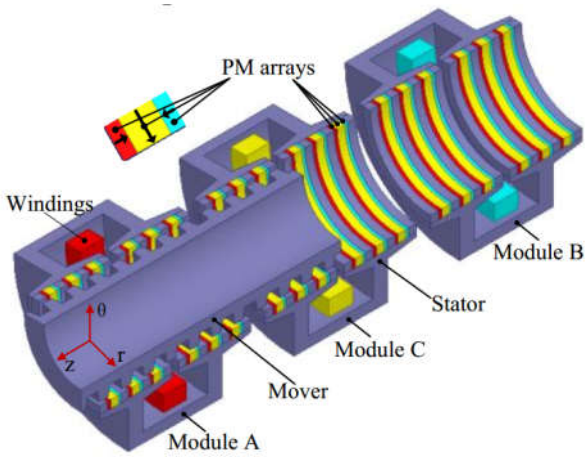

Fig. 1. 26. Linear stator-PM Vernier machines with tubular stator in [125].

1.1.2 Challenges of Stator-PM Machines

Stator-PM machines have been investigated for decades. Some new theories have been developed and various novel topologies have been proposed. By synthetically reviewing the developing history and characteristics of the main four types of stator-PM machines, the following three viewpoints were proposed here. 1) For most of the stator-PM machines, the biased flux characteristic in the windings have not been well recognized and taken advantage of to improve the flux weakening capability. 2) In some of the stator-PM machines, the exciting magnetic field path is open-circuit or short-circuit. So the utilization of PMs is low and cogging torque is large. 3) Comparing with rotor-PM machines, the torque density for stator-PM is still lower. In rotary motions, stator-PM machines still have no advantages.

To meet the mentioned three challenges, this thesis addressed the following topics, 1) developing biased flux machines to expand the flux weakening capability, 2) developing doubly complementary machines to improve PM utilization and reduce torque ripple, 3) exploring new topologies with torque density higher than rotor-PM machines for low speed applications.

1.2 Contents of this Thesis

This thesis includes seven chapters, in chapter one, the overview of stator-PM machines are presented. The development history and tend of four kinds of stator-PM machines are introduced and the challenges of stator-PM machines are concluded.

In chapter two, the electric machines developed from double salient machines are proposed. These machines are investigated from the traditional double salient and the magnetic gear effect perspectives. From the traditional salient machine perspective, the operation principle and the structure of these machines are introduced firstly then followed by the analysis of their coil flux and winding flux. Thirdly, general electromagnetic performance of these machines are analyzed to evaluate the back-EMF, inductance and cogging torque and one 12-11 machine is well designed to evaluate its performance. The simulation results show this machine has relatively high torque density, little torque ripple and acceptable efficiency. This kind of machines has great potential in high torque low speed direct drive applications. The general design guideline from the double salient perspective for this kind of machines is concluded. On the other

hand, this machine is studied from the flux modulated perspective since it has the very similar structure with double rotor flux modulated machines. It is revealed that various harmonic components of flux are generated and contribute to the effective torque rather than merely single dominant one. By applying this approach, a new class of biased flux machines with flux bidirectional bias is derived and the essential operation principle is explained clearly. The design guidelines including the winding connection pattern, the flux modulation principle as well as the detailed interaction process of the flux harmonics created by PMs and winding current are investigated in this chapter. The machine prototype is built and tested to verify the proposed design theory and simulation analysis.

In chapter three, aiming to improve permanent magnet (PM) utilization factor, suppress cogging torque and reduce back-EMF harmonics in stator-PM machines, a new type of stator-PM doubly complementary machines (DCMs) are proposed. These machines have two complementarities as one exists in complementary rotors and the other exists in the basic units belonging to same phases. The first one applies the complementary rotors to construct a consecutive switching path for permanent magnet exciting flux, so that shorted or open magnetic path is avoided to reduce cogging torque and improve PM utilization. The second one is designed to reduce back-EMF harmonics and improve the torque density. The topology, working principle, characteristics and design methodology for DCMs are presented. Simulation and experiments are conducted for a 12/11(stator teeth/rotor teeth) DCMs to evaluate its performance and verify this design methodology. It is revealed that this machine could obtain good sinusoidal back-EMF waveform, small torque ripple and high PM utilization factor due to the doubly complementary characteristic. Adopting the doubly complementary idea into axial flux machines, a novel axial flux machine is also proposed to be used in direct drive application. It is shown that the torque density of machine is high and the efficiency is more than 90% at rated speed.

Chapter four investigates the new Vernier machines with consequent-pole PMs in slots and compares the influence of different combinations of rotor and winding poles. These machines have the paralleled magnetic path, which means the armature field will not pass through PMs. So the risk of demagnetization is eliminated and the armature reaction is intensified to improve the torque. Meanwhile, the simple structure makes these machines mechanically reliable and endurable. The principle of the proposed machines is introduced and the combinations of different winding and rotor poles are discussed. One prototype with 24 slots, 2 winding pole-pairs and 22 rotor pole-pairs has been built and tested. The results show that the torque density for prototype could reach 3 Nm/kg under natural cooling condition and the efficiency could get higher than 90%. Meanwhile, the total harmonic distortion (THD) for back electromotive force (back-EMF) is only about 5%, cogging torque is only about 0.8% and electromagnetic torque ripple is merely 5%. It is indicated that this kind of machines have great potential in direct drive applications.

In chapter five, to further improve the torque density of stator-PM machines, one novel dual-PM excitation Vernier machine with short-pitch distributed-windings was proposed. The special parallel magnetic path constructed by the dual-PM structure could increase the equivalent permeance of the air-gap to better utilize the magnetomotive force (MMF) for torque improvement. The distributed-winding could increase the electrical gear ratio of the machine for speed scaling-down and torque turning up. Meanwhile, the short- pitch coils are applied to eliminate back-EMF harmonics to reduce torque ripple. The principle

and characteristics of the proposed machine are introduced in detail. Some essential issues such as the torque percentages contributed by the excitation field harmonics, the effect of the shot-pitch coils and the torque comparison of dual-PM Vernier machine with conventional rotor-PM Vernier machines are introduced. The tested prototype has shown that this machine has good potential for direct-drive application as the torque density could reach 6 Nm/kg under natural ventilation, the total harmonic distortion (THD) for back-EMF is less than 4%, the torque ripple is less than 4% and the efficiency is about 90% under rated speed.

In chapter six, the summary of the works finished or to be finished in future are presented.

Chapter 2 Design, Analysis and Control of Novel Biased Flux Stator-PM Machines

Biased flux stator-PM machines are novel stator-PM machines with biased flux in coils, which can be controlled by biased current to realize flexible excitation field modulation. This biased current includes both DC and AC component, in which the DC component works to generate or modulate the exciting flux and the AC component serves to produce the torque. Meanwhile, the rotors for biased flux machines are simple and robust, which makes them suitable for severe environments. Although biased flux phenomenon has been recognized for half a century in double salient permanent magnet machines and switching reluctance machines, the systematically studies of biased flux machines have not been presented. In this chapter, the novel biased flux stator-PM machines are introduced. Firstly, the definition and characteristics of biased flux machines are introduced. Secondly, the design and analysis of biased flux stator-PM machine are given, where two different design methods based on magnetic circuit analysis and magnetic field modulated analysis respectively are presented. Thirdly, the novel control based on zero-sequence current is proposed to control the biased flux machines. Fourthly, the concept of biased flux is expanded into other machines to achieve additional benefits. Lastly, the conclusions for this chapter are given.

2.1 Definition and Characteristics of Biased Flux Machines

2.1.1 Definition of Biased Flux Machines

The diagram of the bipolar flux machines is shown in Fig. 2.1, where Fig. 2.1(a) demonstrates the general construction of the machines, and Fig. 2. 1(b) illustrates flux linkage waveforms in the coils. In these machines, the relative position of the PMs, and the stationary coils are not fixed but changing with time. With the rotating of the PMs, the polarity of the exciting flux linking with the coils is alternatively changing. Traditional rotor-PM machines belong to bipolar flux machines.

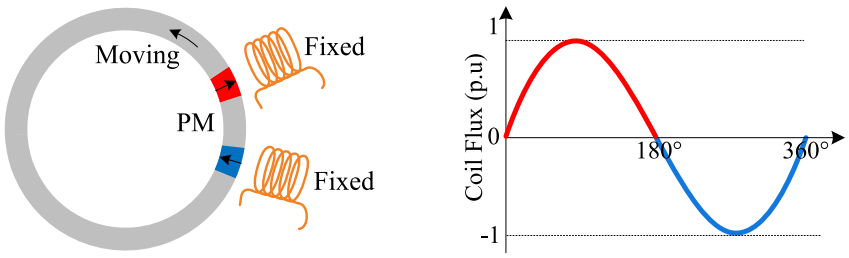

(a) Structure. (b) Coil flux.

Fig. 2.1. Diagram of bipolar flux machines.

The diagram of the biased machines is shown in Fig. 2.2. In these machines, the relative position of the PMs and the coils are fixed, which means the PMs are stationary, while the salient segments rotate during operation. Therefore the BFMs belong to the stator-PM machines. Consequently, BFMs refer to the

machines in which PM flux links the coils with merely positive or merely negative bias or the positive and negative bias combined flux.

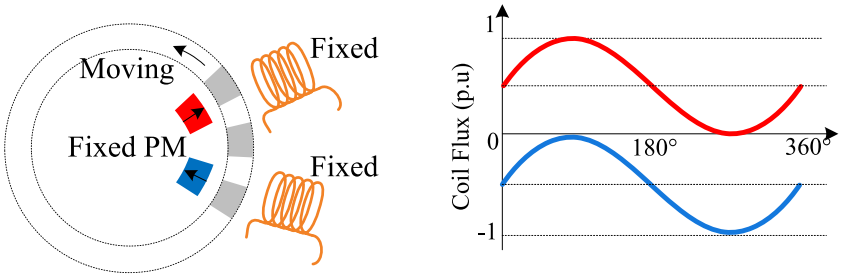

(a) Structure. (b) Coil flux.

Fig. 2.2. Diagram of biased flux machines.

2.1.2 Characteristics of Biased Flux Machines

The major characteristic of biased flux machines is the biased flux, which can be applied to increase the freedoms to modulate the excitation field. In general field oriented control (FOC), there are two degrees of freedoms to control the AC armature current, which are the amplitude and the phase position. The amplitude of the AC current is controlled to modulate the torque while the phase position is controlled to weaken or strengthen the flux as shown in Fig. 2.3.

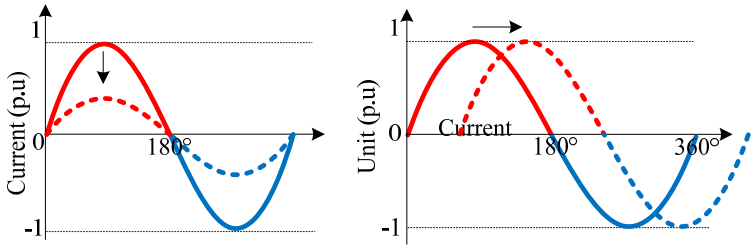

Fig. 2.3. General FOC for bipolar flux machines.

However, with the biased flux characteristic, the degree of freedoms in the current control of the BFMs can be increased to three. Because the polarity of the flux is fixed in the windings, the PM exciting flux could be modulated with DC current in the windings. Meanwhile, the AC armature current components in the same coil can be used to create torque.

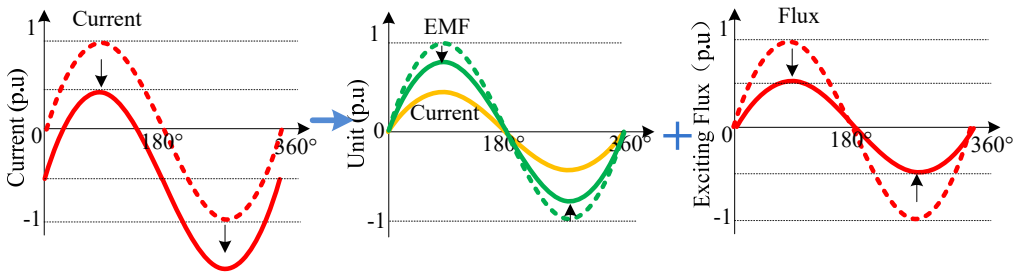

(a) Shifting down control.

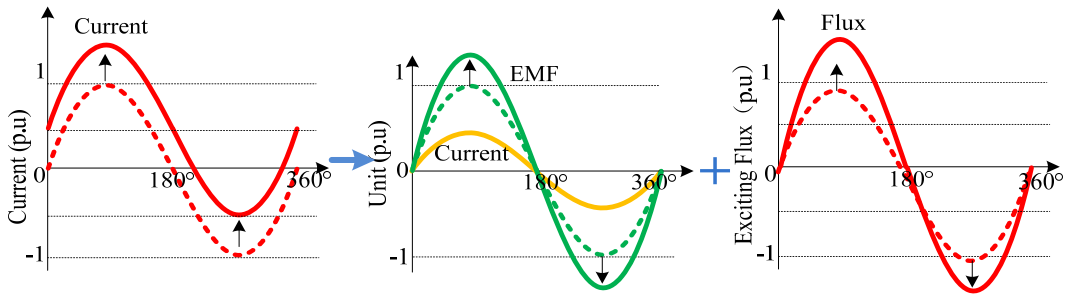

(b) Shifting up control.

Fig. 2.4. Integrated flux control for BFMs.

Fig. 2.4 shows the diagram of the integrated flux control. Fig. 4(a) shows the flux weakening control of BFMs, in which the AC component works the same as that in the FOC, while the negative DC component serves to weaken the exciting flux. Similarly, Fig. 2.4 (b) shows the flux strengthening control with the positive DC bias current component. The integrated flux control has three degree to control the BFMs, which makes the control more flexible and may further improve the flux weakening capability of the BFMs.

2.1.3 What Kind of Machines Belonging to Biased Flux Machines

According to the definition, BFMs covers the stator-PM machines and non-PM machines, specially, mainly including the switch reluctance machines, double salient machines and variable flux reluctance machines. Fig. 2.5 shows the two different SRMs, one is 3-phase 12/8 SRM and the other one is 6-phase 12/10 SRM. In SRM, the drive current in the concentrated winding is biased, so the produced flux in stator teeth is biased, which agrees with the definition of BFM.

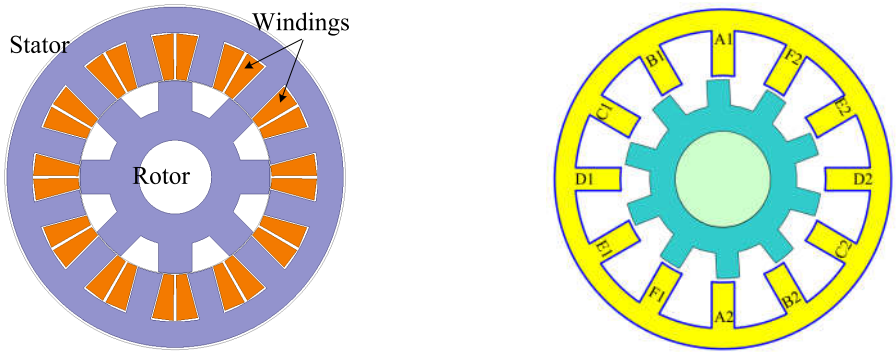

(a) 3-phase 12/8 SRM. (b) 6-phase 12/10 SRM.

Fig. 2.5. One kind of Biased flux machines-SRMs.

The other kind of BFM is double salient permanent magnet (DSPM) machines. Different from SRMs, there are PMs embedded in the stator. Since these machines work with the various permeances when the rotor is moving and the relative positions of the winding and PMs are fixed, the polarity of the flux in the windings stays unchanged. So DSPM machines belong to BFM. Fig. 2.6 shows different DSPM machines. Fig. 2.6 (a) gives the traditional DPSM. In this machine, the teeth number between different PMs is three and six teeth could be regarded as one unit. The magnetic field polarity of teeth in one unit could be

expressed as NNNSSS (N means the north polarity and S means the south polarity). By this way, the DSPMs can be better named and understood. With this naming method, the machines shown in Fig. 2.6 (a) and Fig. 2.6 (b) is 12/8 NNNSSS DSPM and NSNS 12/11 DSPM. The other kind DSPM applied the double stator, which moves the PMs from the primary stator into the secondary stator. The space could be better used to improve the torque density and heat dispassion condition could be improved. These kinds of double stator DSPMs have drawn much more attention in recent year. These kinds of machines also belong to the BFMs when the PMs in inner stator are aligned to the slots. Fig. 2.6 (c) shows the double stator 12/8 NNNSSS DSPM and Fig. 2.6 (d) presented the double stator 12/10 NSNS DSPM.

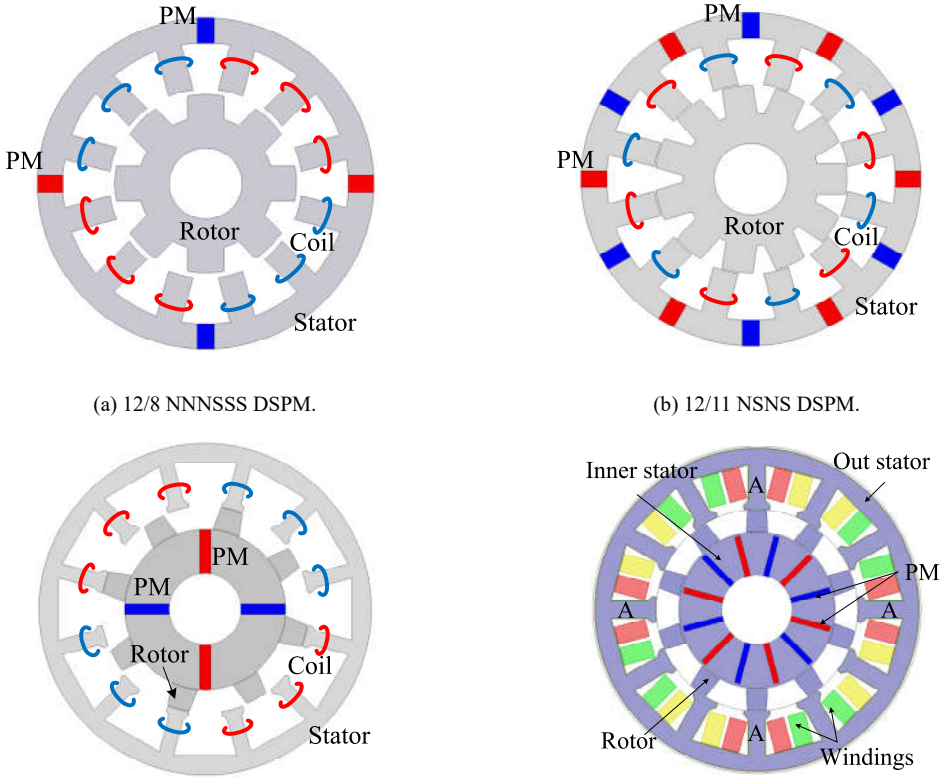

(a) 12/8 NNNSSS DSPM.

(b) 12/11 NSNS DSPM.

(c) Double stator 12/8 NNNSSS DSPM.

(d) Double stator 12/10 NSNS DSPM.

Fig. 2.6. One kind of biased flux machines-DSPMs.

The other kind of BFM is the electrical exciting machines, namely variable reluctance machines, which applies the DC excitation windings to replace the stator-PMs to generate the excitation field. So basically, this kind of machines has the similar principle of DSPM. The difference is that the excitation field of these machines is easy for modulation. Fig. 2.7 (a) shows the double-salient doubly-excited variable reluctance motor, and Fig. 2.7 (b) shows the non-overlapping variable reluctance motor with salient pole rotor.

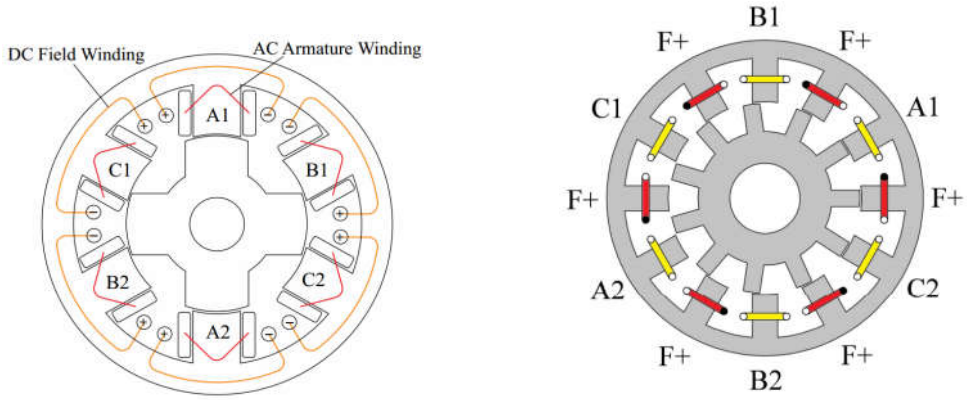

(a) 6/4 double-salient doubly-excited VRM. (b) 12/11 Non-overlapping VRM.

Fig. 2.7. One kind of Biased flux machines-VRMs.

With clear definition, it is found that BFMs includes many kinds of machines, including SRM, DSPM and VRM. Actually, the biased flux phenomenon has been noticed for decades, however, this characteristic seems has no positive influence to the machines, so this phenomenon has not drawn much attentions and the clear concept of biased flux machines have not been build. In this chapter, it is found that biased flux characteristic can be applied to realize more flexible excitation field modulation by using biased current. Consequently, the definition of BFM is given and which kinds of machines belong to BFM is summarized. Theoretically, the biased current drive is suitable for all of the mentioned machines above.

2.2 Design of Double Stator BFMs

It has been introduced that BFMs include many kinds of machines and it is also known that double stator structure could improve the torque density by further improving the space utilization. Meanwhile, the heat dissipation could also be improved since PMs are moved into the secondary stator. In this section, one novel kind of double stator BFMs is introduced. Two design methods based on magnetic circuit construction and magnetic field modulation theory are introduced.

2.2.1 Magnetic Circuit Construction Method

The basic principle for the magnetic circuit is to construct windings with biased exciting flux, so that the biased current could be used for drive. To realize this, how to construct biased flux in single coil, construct machine structures, connect coils into windings and design corresponding drive circuits are necessary and important.

1) Constructing Biased Flux in Single Coils

The preliminary of magnetic circuit design is to construct biased flux in the single coils. And hence, the final windings connected by coils could keep the biased component. To obtain biased flux in the coils, PMs should not be installed in rotor but be fixed at certain stationary positions to make sure the flux polarity in the coils keeps unchanged. This design applies the double stator structure with PMs installed in inner stator, which contribute to improved torque density and good heat dissipation condition. With coils in outer stator slots and PMs in inner stator, how to construct exciting flux path to ensure the coils have biased flux is

therefore the key. The main idea used in this design is to construct varied permeance along the air-gap, so the coils could get varied flux with rotor moving. The basic structure is shown in Fig. 2.8, where the rotor is formed by separated iron pieces and the polarity of the adjacent PMs is opposite.

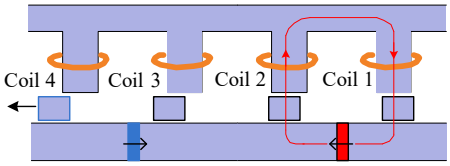

(a) Aligned position.

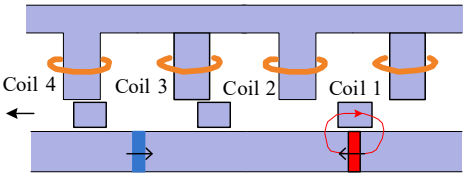

(b) Unaligned position.

Fig. 2.8. Diagram of constructing biased flux in Coil 1 and Coil 2.

It is shown that when rotor moves into the aligned position, the PM flux goes through Coil 1 and Coil 2 to form the loop. The coil flux gets maximum value at this position. After that, the coil flux decreases with rotor moving. When rotor moves to unaligned position shown in Fig. 2.8 (b), the coil flux for Coil 1 and Coil 2 gets zero since the PM flux is shorted. Afterwards, the coil flux will increase as the permeance gets greater with rotor moving. It is seen that the coil flux in Coil 1 and Coil 2 is biased, and this situation also exists in other coils. Following with this design principle, the biased flux in coils is constructed. Noticeably, the polarity of the coils could be used to distinguish different structure, because each structure has unique coil flux pattern. Using N and S to represent the coil flux with positive and negative polarity respectively, the coil flux pattern for this machine would be NNSS. If the PM pieces are doubled and installed under each of the slots in inner stator, the coil flux pattern for this structure could be NSNS.

2) Constructing Machine Structures

With the basic principle shown in Fig. 2.8, two NNSS double stator BFMs with 12/10 (stator teeth/rotor teeth) and 12/11 are constructed, which are shown in Fig. 2.9(a) and Fig. 2.9(b) respectively. To analyze the coil flux vector, the conductor polarity in each coil keeps the same with Coil 1. No-load flux distributions for these two machines are presented in Fig. 2.10 to Fig. 2.12 to demonstrate their operation principle, where rotor position θ_e changes from 0 electric degrees to 270 electric degrees.

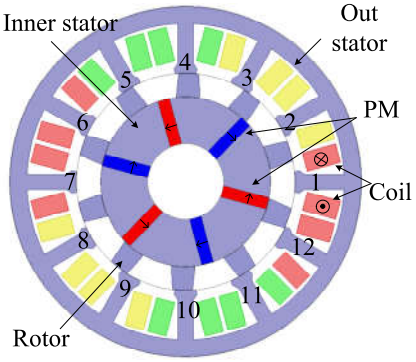

(a) NNSS double stator 12/10.

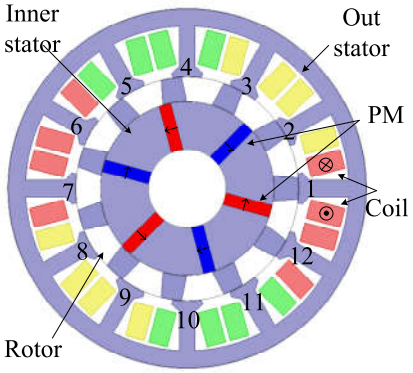

(b) NNSS double stator 12/11.

Fig. 2.9. Proposed BFMs.

The diagram of flux waveforms in Coil 1 and Coil 12 is demonstrated in Fig. 2.10. When $\theta_e = 0°$, the coil flux gets peak value because the overlap area of rotor and stator teeth gets maximum, as shown in Fig. 2.11(a) and Fig. 2.12(a). From $\theta_e = 0°$ to $\theta_e = 90°$, the flux value drops with the decrease of the overlap area, as shown in Fig. 2.11(b) and Fig. 2.12(b). Till $\theta_e = 180°$, flux value gets minimum value, as shown in Fig. 2.11(c) and Fig. 2.12(c). Afterwards, from $\theta_e = 180°$ to θ_e=270°, the flux value increases, as shown in Fig. 2.11(d) and Fig. 2.12(d).

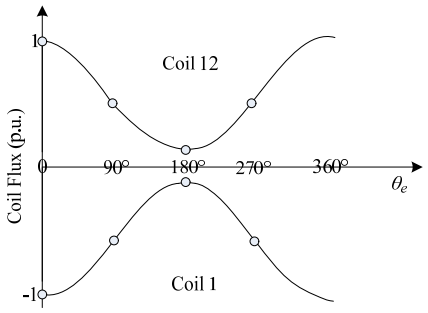

Fig. 2.10. Diagram of coil flux in double stator NNSS BFMs.

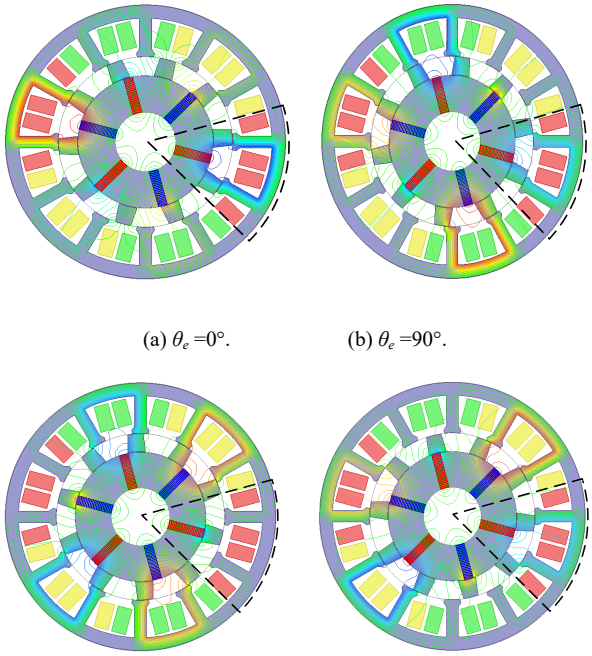

(a) θ_e =0°. (b) θ_e =90°.

(c) θ_e =180°. (d) θ_e =270°.

Fig. 2.11. Open-circuit flux distribution of double stator NNSS 12/10 BFM.

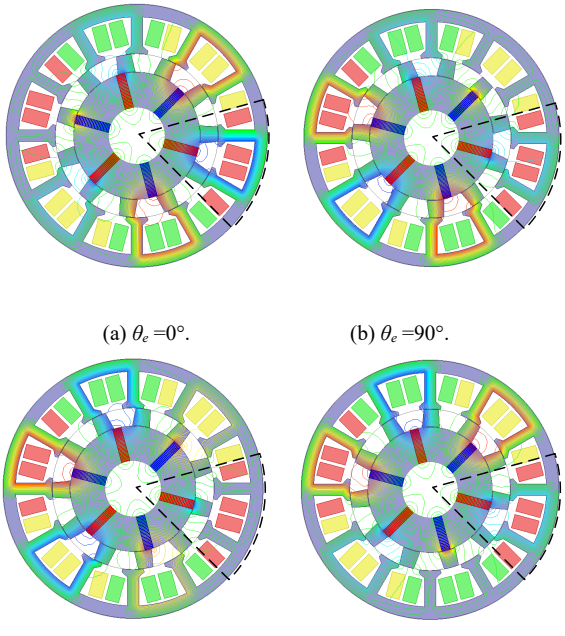

(a) θ_e =0°. (b) θ_e =90°.

(c) θ_e =180°. (d) θ_e =270°.

Fig. 2.12. Open-circuit flux distribution of double stator NNSS 12/11 BFM.

3) Connecting Coils into Windings with Biased Flux

Connecting coils into windings is another important issue for BFMs due to its special drive current. The coil flux vector is used in this chapter to obtain the connection of windings, as this method could keep the

biased flux component in final windings and obtain highest winding factor. The coil flux vector method depends on two parameters of the coils. First one is the polarity of the coil flux and second is the phase difference between different coils. The polarity of coil flux is easy to be determined according to the structure, while the phase difference between coils needs derivation.

The phase difference between different coil groups is used for analysis, and each group includes two coils. These two coils have the same flux magnitude but opposite polarity. The number of coil groups can be expressed as N_s/q, where N_s is the stator teeth number, q is the coil number under same PM pole (q=2 in NNSS BFMs). The phase difference between the adjacent groups α_G can be expressed:

$$\alpha_G = \pi + (\frac{2\pi}{N_s} - \frac{2\pi}{N_r})N_r q \tag{2-1}$$

where N_r is the rotor teeth number. There is 180° shift between different groups because of the opposite PM polarity in adjacent groups. By defining flux phase of Coil 1 as zero, the flux phase α_i for Coil i can be expressed as:

$$\alpha_i = \begin{cases} \alpha_{i-1} + \alpha_G, i = 2k, k = 1,2...6 \\ \alpha_{i-1} + \pi, i = 2k+1, k = 1,2...5 \end{cases} \tag{2-2}$$

For coils with even number, they lead the following coil to form the new group, so when i is even number, the phase should be added α_G based on Coil_{i-1}. While when i is odd number, it just following the previous Coil_{i-1} to from the same group, so the phase is added π because of the opposite flux polarity for the coils belonging to same group.

Based on the coil flux polarity and phase position, the flux vector can be derived to direct the winding connection. Fig. 2.13 shows the coil flux vector for NNSS 12/10 and 12/11 BFMs. To distinguish the flux polarity, the flux with negative polarity is set in the inner circle, while the one with positive polarity is set in the out circle.

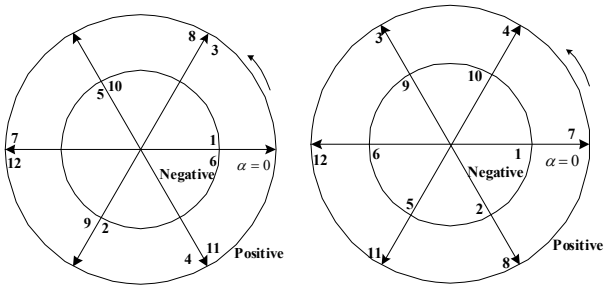

(a) NNSS 12/10. (b) NNSS 12/11.

Fig. 2.13. Coil flux vector for double stator BFMs.

As shown in Fig. 2.13, the coil flux vector not only reflects the coil flux phase position, but also indicates the coil flux polarity. In connecting the final windings, both AC and DC component of the coil flux should be considered. For example, the coils with same flux polarity should not be connected in subtractive series. Otherwise, the DC component will be cancelled. The coils with different phase position should not be connected in series. Otherwise, the AC component will be reduced.

Based on that principle, the final winding connection pattern for 12/10 and 12/11 BFM is shown in Fig. 2.14. The coils for 12/10 machine are connected into three windings A, B and C. These windings have

positive biased exciting flux, and the phase difference among the winding flux is 2π/3. Since the final windings keep the DC component of exciting flux, the biased current could be used to adjust the exciting field.

The coils for 12/11 machine are connected into six windings A1, B1, C1, A2, B2 and C2. These six windings are divided into two groups, the positive group and negative group. Positive group includes A1, B1 and C1 and negative group includes A2, B2, and C2. The winding flux phase difference among each group is 2π/3, and there is no phase difference for A1 and A2. This characteristic makes this machine have two groups of three phase windings. The AC drive current for each group should be the same, while the DC biased drive current for them should be opposite. Under this way, the DC biased current could work to adjust the exciting field and AC current could create the same rotating magnetic field.

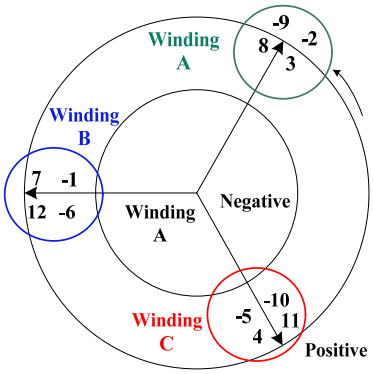

(a) NNSS 12/10.

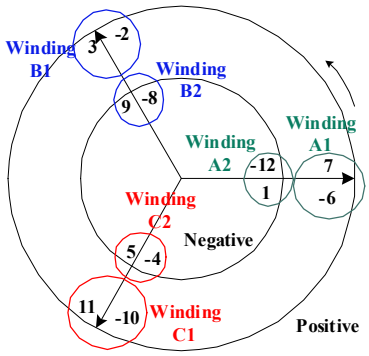

(b) NNSS 12/11.

Fig. 2.14. Winding connection pattern for double stator BFMs.

4) The Drive Circuit for BFMs

The special drive circuit is presented for BFMs for the unconventional winding connecting pattern and drive method. Fig. 2.15(a) presents the drive circuit for 12/10 BFM. The neutral point is connected into the midpoint of the DC bus capacitors. The zero sequence current in three phase windings is therefore controllable to adjust the exciting field. Fig. 2.15 (b) gives the drive circuit for 12/11 BFM. The windings are divided into two groups, and the neutral points of each group are connected. With special switching pattern, the DC zero sequence current for the groups are opposite and the AC current component could keep same.

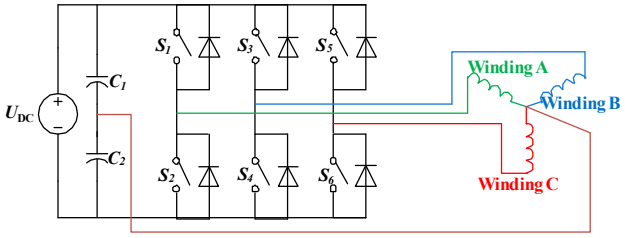

(a) NNSS 12/10.

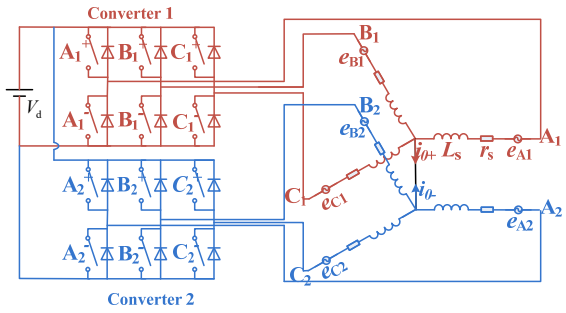

(a) NNSS 12/11.

Fig. 2.15. Drive circuit for double stator BFMs.

2.2.2 Magnetic Field Modulated Method

The magnetic circuit constructing method is based on the magnetic path observation. The used methodology is to select structure firstly and then observe the coil flux for windings interconnection. After that the detailed dimensions are optimized for further evaluation of the performance. If this structure turns out infeasible, one should get back to the first step to search other potential structures. Actually, the initial searching process is stochastic, which is a trial-and-error methodology. It is time consuming and ineffective. Besides that, the torque generating principle of BFMs has not been fully revealed, as which harmonics of space magnetic fields have contributed to the torque is rarely reported. To solve the above two issues, in this section, one topology exploration method for BFM based on magnetic field modulation mechanism is proposed, and its torque generating principle is analyzed. This method could provide a new perspective to design BFMs and better understand their operation principle.

1) Structure Exploration

Magnetic field modulation mechanism was first recognized in magnetic gear then it was adopted into the machine design to investigate the magneitic field modulated machines. In this part, the field modulation mechanism is applied to explore the potential structures for double stator biased flux machines. Fig. 2.16 is presented here to briefly introduce this mechanism.

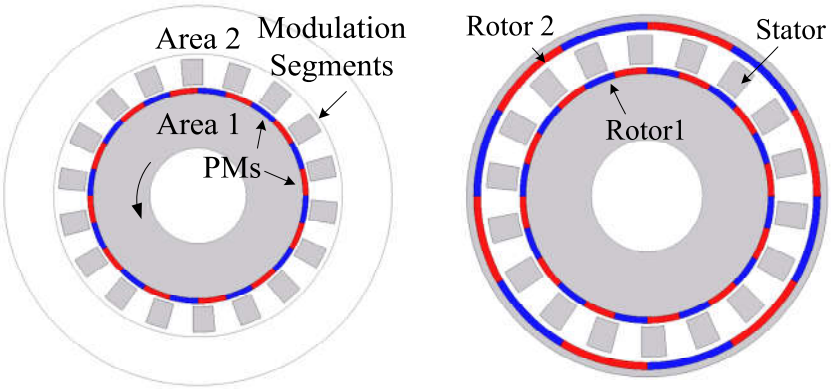

(a) Diagram of the flux modulation effect (b) Magnetic gear.

Fig. 2.16. Magnetic field modulation principle and its application.

In area 1, the pole-pair number of magnetic field produced by PMs is P_{PM}. After modulation, the pole-pair number of the magnetic field in area 2 will be changed. By inserting PMs into rotor 2 to interact with the modulated magnetic field, it is possible for the rotor to obtain constant torque.

Assuming the rotation velocity of PMs in area 1 is ω_{PM}, the number of the salient pieces is N_{r} and the rotation velocity of salient pieces is ω_{Nr}, the flux space harmonics in the air-gap $P_{u,v}$ and its corresponding velocity $\omega_{u,v}$ could be expressed by the following equations according to the magnetic field modulation principle,

$$P_{u,v} = \left| uP_{\mathrm{PM}} + vN_r \right|, u = 1,3,5 \ldots v = 0, \pm 1, \pm 2 \ldots \tag{2-3}$$

$$\omega_{u,v} = \frac{uP_{PM}}{uP_{PM} + vN_r}\omega_{PM} + \frac{vN_r}{uP_{PM} + vN_r}\omega_{Nr}, u = 1,3,5 \ldots v = 0, \pm 1, \pm 2 \ldots \tag{2-4}$$

By replacing any side of PMs with windings, dual-rotor electric machines could be developed. Noticeably, the dual-rotor electric machines have almost the same structure with double stator BFMs. The only difference is that the double rotors of dual-rotor machines could both rotate, while for BFMs, one of them should be fixed to generate biased flux in the coils.

Therefore the magnetic field mechanism used in design the dual-rotor machines could be adopted into design BFMs. The pole pairs of the windings and PMs, the number of segment pieces could be determined by this mechanism. To keep the DC component of the biased flux in the final windings, some special rules are also needed to direct this design. Generally, the new method proposed in this chapter is to apply magnetic field modulation mechanism to explore potential structures and then select the feasible ones which could keep biased flux in the final windings.

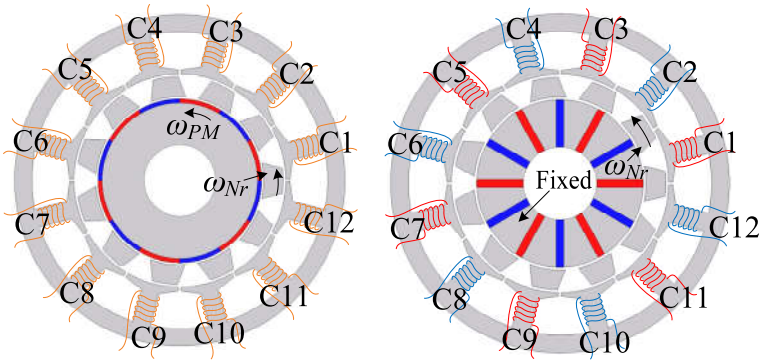

(a) 12-slot 6-pole-pair dual-rotor machines. (b) NSNS DSBFM.

Fig. 2.17. Derivation of NSNS DSBFM.

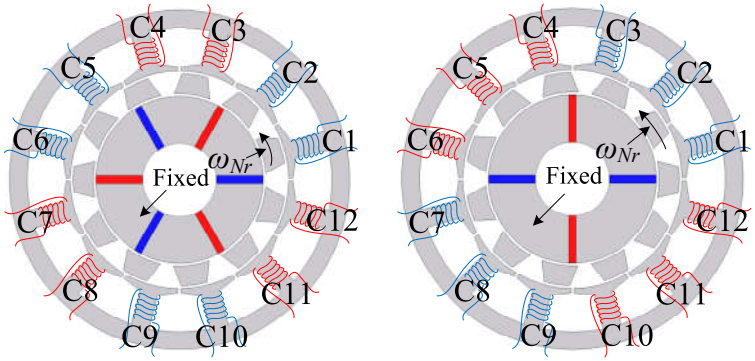

(a) 12-slot 3-pole-pair NNSS DSBFM. (b) 12-slot 2-pole-pair NNNSSS DSBFM.

Fig. 2.18. Different configurations of DSBFMs.

The 12-slot concentrated winding machines are used for examples to demonstrate the derivation of double stator BFMs. Fig. 2.17(a) is a 12-slot 6-pole-pair dual-rotor machine. To obtain the biased flux in coils, the inner rotor should be fixed at certain positions. The rule of fix the inner rotor position is to ensure the coil will be underneath one single PM pole. Under this way, the coil flux could merely vary with the changing of permeance but will not change its polarity. With inner rotor fixed in the position shown in Fig. 2.17(b), the coil flux polarity in 12 coils could be fixed. The flux polarity in the coils with odd number is marked with *N*, while the flux polarity in the coils with even number is marked with *S*. Therefore, this is a *NSNS* 12/11 double stator BFM. Similarly, the NNSS 12/11 and NNNSSS 12/11 double stator BFM could also be developed, as shown in Fig. 2.18.

However, not all the dual-rotor magnetic field modulation machines could be transferred into BFMs. Only the ones with all coils underneath one single PM pole could obtain that. This means the slot number N_S could be divided by the PM poles 2*N_P (N_P means the pole-pair number). Besides, since the coils are divided into two groups with negative and positive biased flux symmetrically, the slot number N_S must be an even number. Meanwhile considering the phase number of machines, the slot number N_S should also be dividable by phase number, so the general formula to determine N_S and N_P is given by

$$\begin{cases} N_s = 6l, l = 1,2,3... \\ N_p = \{x \mid \mathrm{mod}(N_s, 2x) = 0, x = 1,2,3...\} \end{cases} \tag{2-5}$$

With this formula, the potential structure of the three phase BFMs could be derived as listed in Table 2. 1.

Table 2. 1 Potential Structures of BFMs

N_S	2 N_P	N_S / 2N_P	Classified as
6	2	3	$\underbrace{\text{N...}}_{3}\underbrace{\text{S...}}_{3}$
	4	6/4	NA
	6	1	$\underbrace{\text{N}}_{1}\underbrace{\text{S}}_{1}$
	>6	<1	NA
12	2	6	$\underbrace{\text{N...}}_{6}\underbrace{\text{S...}}_{6}$
	4	3	$\underbrace{\text{N...}}_{3}\underbrace{\text{S...}}_{3}$
	6	2	$\underbrace{\text{N...}}_{2}\underbrace{\text{S...}}_{2}$
	8	12/8	NA
	12	1	$\underbrace{\text{N}}_{1}\underbrace{\text{S}}_{1}$
	>12	<1	NA
6i (i=1,2...)	2k_1 (k_1=1,2...)	3i/3k_1	$\underbrace{\text{N...}}_{N_S/N_P}\ \underbrace{\text{S...}}_{N_S/N_P}$

2) Winding Connection pattern

It is noted that BFM should be driven by biased current to achieve advantages, so the final windings must keep the DC component of the biased flux and do not undermine the AC component in the coils. As a result, the winding connection pattern for BFM is different from the traditional way, which is necessary to introduce that.

BFMs have coils wounded on each teeth and each coil could obtain various biased flux when rotor is moving. With the method of using vectors to indicate the polarity and phase position of the coil flux, the coil flux vector could be plotted to direct winding interconnection. The location of the coils could be used to determine the polarity of the coil flux, and (2-6) could be derived to calculate the phase position difference of each coil vector according to the magnetic modulation effect.

$$\alpha=\frac{2\pi\cdot(N_r-N_p)}{N_s} \tag{2-6}$$

Based on the polarity and phase position difference, the coil vector could be plotted.

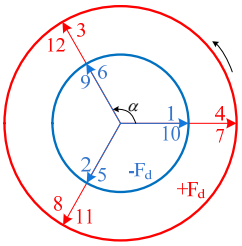

Fig. 2.19. Flux vectors for NNSS 12/11 double stator BFM.

NNSS 12/11 double stator BFM is taken for demonstration. Taking the parameters of this machine into (2-6), α could be figured out as $4\pi/3$. To distinguish the polarities, two circles are sued. The vectors ending at outer circle are the ones with positive DC flux $+F_d$, while the vectors ending at inner circle are the ones with negative DC component $-F_d$. So the final coil vectors are drawn in Fig. 2.19. Based on the flux vectors, the coil connecting pattern is given in Fig. 2.20. Fig. 2.20(a) shows how to connect six windings labeled with A1, A2, B1, B2, C1 and C2 with the coils.Fig. 2.20(b) shows how to connect the six windings into double layers.

Noticeably, the upper layer winding only includes the coils with $+F_d$ while the lower layer winding only includes the coils with $-F_d$. Under this way, the DC component of the coils could be reserved. In terms of the AC component of the coil flux, phase A is taken for example for analysis. Phase winding A is formed by A1 and A2, A1 includes C_4 and C_7 while A2 includes C_1 and C_{10}. The phase positions of these four coils are the same, so their back-EMFs and AC components of the coils are identical. With this winding configuration, the biased current could be used to drive this machine, as A1 is driven by biased current with positive DC component while A2 is driven by biased current with negative DC component.

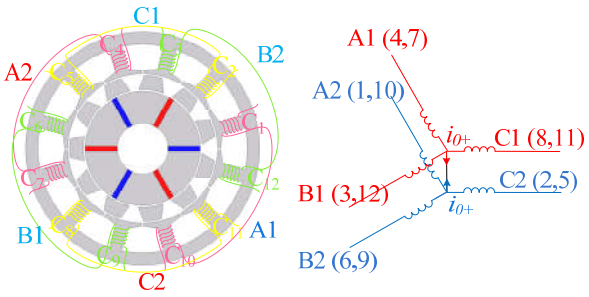

(a) Configuring six windings. (b) Connecting windings as double layers.

Fig. 2.20. Coil connecting pattern.

3) Torque Component Analysis

The torque generating principle of the double stator BFM will be discussed in this section. Firstly, the space fields produced by the PMs and windings are analyzed with the magnetic field modulation mechanism. Secondly the effective space harmonics are developed to reveal which harmonics of exciting field and armature field have contributed to the torque.

a) Magnetic Field produced by PMs

Firstly, the magnetic field modulation effect for the PM created field is analyzed. The finite element

software Maxwell is used to conduct simulations. Fig. 2.21(a) shows the original field produced by the PMs and Fig. 2.21(b) shows the space field modulated by the iron salient pieces.

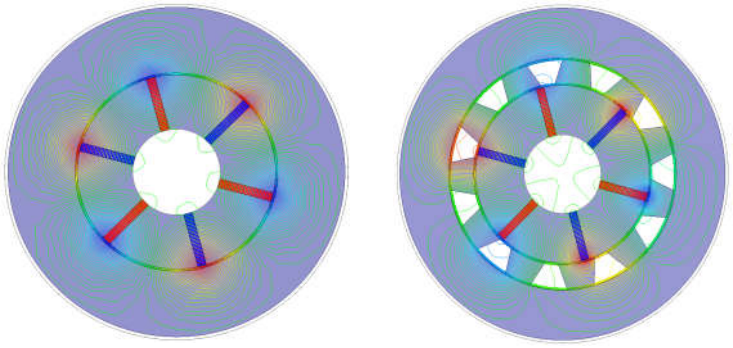

(a) Original PM field. (b) Field modulated by the salient rotors.

Fig. 2.21. Field modulation effect for the PM created field.

The radial air-gap flux density and its FFT analysis before and after the modulation are shown in Fig. 2.22 and Fig. 2.23. It is seen that the major component of the original PM field is 3rd harmonics. This is comprehensible since the PMs are six pieces with 3 pole pairs.

After modulation, the harmonics become richer, as the magnitudes of 2nd, 8th, 9th, 14th and 19th harmonics rise. In traditional machines working with fundamental magnetic field, these harmonics are harmful because they cannot generate the constant torque. But in this double stator BFM, the situation is different.

Many of these exciting field harmonics will interact with armature field harmonics to generate torque, as long as they have the same order and rotating velocity. Therefore the rotating velocity of these harmonics should also be analyzed to figure out which of them are effective harmonics.

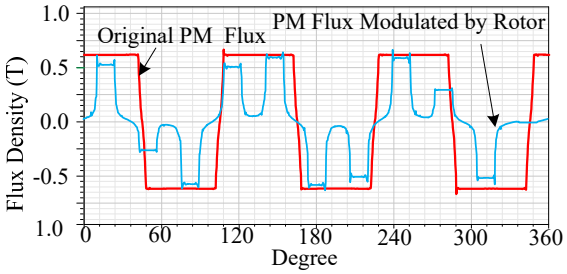

Fig. 2.22. Space magnetic field density created by PMs.

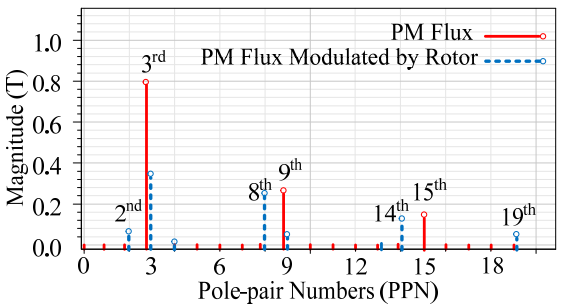

Fig. 2.23. FFT analysis of space magnetic field density created by PMs.

Using P_{PM}, N_r, ω_{PM}, ω_{Nr} to represent the pole-pair number of the original PM field, the number of salient pieces, the velocity of P_{PM} and the velocity of N_r. According to the magnetic field modulation principle

introduced above, the pole-pair number and the corresponding rotary velocity of the magnetic fields in air-gap are modulated by the rotor pieces. So the modulated pole-pair number $P_{P_{PM},m,k}$ and its velocity $\omega_{P_{PM},m,k}$ could be expressed as:

$$P_{P_{PM},m,k} = \left| mP_{\mathrm{PM}} + kN_r \right|, m = 1,3,5 \ldots k = 0, \pm 1, \pm 2 \ldots \tag{2-7}$$

$$\omega_{P_{PM},m,k} = \frac{mP_{PM}}{mP_{PM} + kN_r}\omega_{PM} + \frac{kN_r}{mP_{PM} + kN_r}\omega_{Nr}, m = 1,3,5 \ldots k = 0, \pm 1, \pm 2 \ldots \tag{2-8}$$

Ignoring the high order harmonics with small amplitude, the field pole pairs and the corresponding velocity of original and the secondary magnetic fields after modulation could be figured out based on Fig. 2.23 and Eq. (7-8). The final results are summarized in Table 2. 2.

Table 2. 2 Magnetic Field Space Harmonics Produced by PMs

Original		After modulation	
P_{PM}	ω_{PM}	$P_{P_{PM},m,k}$	$\omega_{P_{PM},m,k}$
3	0	$P_{3,m,k} = \lvert 3m + 11k \rvert$	$\frac{11k}{3m+11k}\omega_{Nr}$
9	0	$P_{9,m,k} = \lvert 9m + 11k \rvert$	$\frac{11k}{9m+11k}\omega_{Nr}$
15	0	$P_{15,m,k} = \lvert 15m + 11k \rvert$	$\frac{11k}{15m+11k}\omega_{Nr}$

b) Magnetic Field Produced by Windings

Similarly, the space harmonics of the magnetic field created by the windings are also analyzed when *q*-axis current is injected. Fig. 2.24(a) and Fig. 2.24(b) show the original and modulated winging fields respectively. The magnetic field density along the air-gap and its FFT analysis before and after modulation are shown in Fig. 2.25 and Fig. 2.26, respectively.

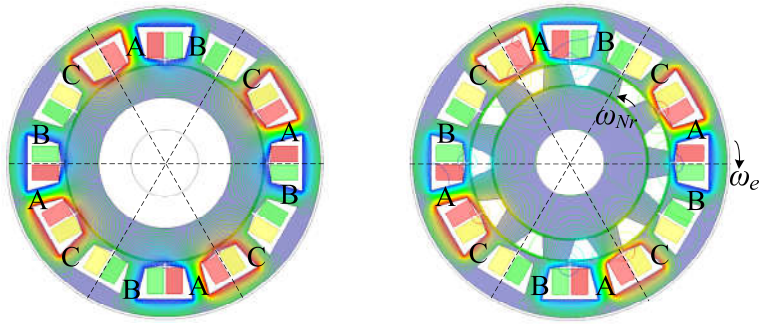

(a) Original winding field. (b) Field modulated by the salient rotor.

Fig. 2.24. Field modulation effect for the winding flux.

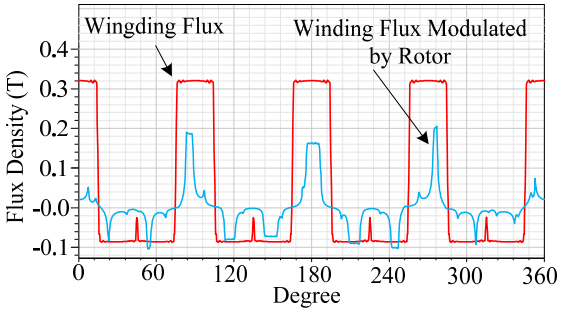

Fig. 2.25. Magnetic field density created by windings.

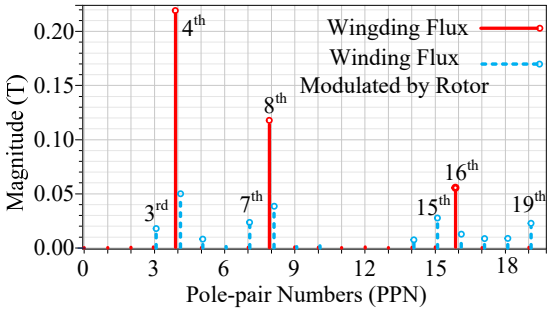

Fig. 2.26. FFT analysis of magnetic field density created by windings.

From the FFT analysis, it is observed that the pole-pair numbers of the winding field is not certainly a single value, but with a series of components such as 4th, 8th and 16th. This is because the pole-pair numbers of 8 has the same winding connection pattern with 4 and 16 in the machines with 12 slots.

Using PPW, ω_W to represent the pole-pair number of the original winding field and its velocity, the modulated pole-pair number $P_{P_W,i,j}$ and its velocity $\omega_{P_{P_W},i,j}$ can be expressed as:

$$P_{P_W,i,j} = \left| iP_{P_W} + jN_r \right|, i = 1,3,5 \ldots j = 0, \pm 1, \pm 2 \ldots \tag{2-9}$$

$$\omega_{P_{P_W},i,j} = \frac{iP_{P_W}}{iP_{P_W} + jN_r}\omega_W + \frac{jN_r}{iP_{P_W} + jN_r}\omega_{Nr}, i = 1,3,5 \ldots j = 0, \pm 1, \pm 2 \ldots \tag{2-10}$$

The high order harmonics with small amplitude could be ignored to simplify the analysis. Assuming the frequency of AC current is *f*, the angular velocity of current ω_e equals $2\pi f$. With this connection, the angular velocities for 8th, 4th and 16th harmonics are $\omega_e / 8$, $-\omega_e / 4$ and $-\omega_e / 16$, respectively. The minus signal means these harmonics rotate with the opposite direction. After modulation, the magnetic field characteristics including the pole-pair number $P_{P_W,i,j}$ and corresponding velocity $\omega_{P_W,i,j}$ produced by windings could be calculated by Eq. (2-9) and Eq. (2-10). The results are listed in Table 2. 3.

Table 2. 3 Magnetic Field Harmonics Produced by Windings

Original		After Modulation	
P_W	ω_W	$P_{P_W,i,j}$	$\omega_{P_W,i,j}$
4	$-\frac{\omega_e}{4}$	$P_{4,i,j}=\lvert 4i+11j\rvert$	$\frac{4i}{4i+11j}\omega_W+\frac{11j}{4i+11j}\omega_{Nr}$
8	$\frac{\omega_e}{8}$	$P_{8,i,j}=\lvert 8i+11j\rvert$	$\frac{8i}{8i+11j}\omega_W+\frac{11j}{8i+11j}\omega_{Nr}$
16	$-\frac{\omega_e}{16}$	$P_{16,i,j}=\lvert 16i+11j\rvert$	$\frac{16i}{16i+11j}\omega_W+\frac{11j}{16i+11j}\omega_{Nr}$

c) Effective Magnetic Field Harmonics

As mentioned above, in traditional machine working with fundamental magnetic field, the other harmonics are harmful. But for this double FBM, many harmonics may contribute to torque. Revealing which harmonics could contribute to torque generation helps to understand the operation principle of this machine.

Actually, the harmonic order represents the pole-pair number of the field since the FFT analysis of the field harmonics is conducted along the air-gap.

To figure out the effective magnetic field harmonics, the electromagnetic torque is expressed by air-gap flux density. With $B_{\mathrm{PM}i}$ and $B_{\mathrm{W}i}$ to express the magnitude of i^{th} magnetic field harmonic produced by PM and windings respectively, the electromagnetic torque T_{e} can be expressed by (2-11) according to Maxwell stress tensor.

$$T_e=\frac{l_m {r_{gap}}^2}{\mu_0}\sin\psi\int_0^{2\pi}\sum_{P_{PM}=1}^{\infty}B_{PMP_{PM}}\sin(P_{PM}\theta)\sum_{P_{PW}=1}^{\infty}B_{WP_{PW}}\sin(P_{PW}\theta)d\theta \tag{2-11}$$

where, l_m is the machine axial length, r_{gap} is the radius of average air-gap, μ_0 is the permeability of vacuum, ψ is the angle between the vector of exciting magnetic field and armature magnetic field, P_{PM} is the harmonic order of PM produced field, P_{PW} is the harmonic order of winding produced field and θ is the mechanical angle.

Noticeably, ψ reflects the drive condition of the machine, when $\psi<90°$, the machine operates in flux strengthening condition, while when $\psi>90°$, the machine operates in flux weakening condition.

Here, ψ=90° is applied to generate maximum torque. So in simulations, the d-axis current is set as zero.

$$\sin\psi\int_0^{2\pi}B_{PMP_{PM}}\sin(P_{PM}\theta)B_{WP_{PW}}\sin(P_{PW}\theta)d\varphi=0 \tag{2-12}$$

It is easy to prove Eq. (2-12) when $P_{PM}\neq P_{PW}$, so Eq. (2-11) can be simplified as,

$$T_e=\frac{l_m {r_{gap}}^2}{\mu_0}\sin\psi\sum_{P_{effective}=1}^{\infty}B_{PMP_{effective}}B_{WP_{effective}} \tag{2-13}$$

where, $P_{effective}$ is the effective magnetic harmonics.

Using $H_{PM}(P_{P_{PM},m,k},\omega_{P_{PM},m,k})$ and $H_W(P_{P_W,i,j},\omega_{P_W,i,j})$ to represent the PM produced fields and winding produced fields respectively. The effective harmonics could be figured by enumerating *m, k, i, j* to make

$$H_{PM}(P_{P_{PM},m,k},\omega_{P_{PM},m,k}) = H_W(P_{P_W,i,j},\omega_{P_W,i,j}) \tag{2-14}$$

With Eq. (2-13) and Eq. (2-14), the effective harmonics for this double stator BFM and the torque components contributed by these harmonics could be figured out.

Table 2. 4 Effective Magnetic Field Harmonics

$H_{PM}(P_{P_{PM},m,k},\omega_{P_{PM},m,k})=H_W(P_{P_W,i,j},\omega_{P_W,i,j})$		Order	Velocity
$H_{PM}(P_{3,1,0},\omega_{3,1,0})$	$H_W(P_{8,1,-1},\omega_{8,1,-1})$	3	0
$H_{PM}(P_{15,1,-1},\omega_{15,1,-1})$	$H_W(P_{4,1,0},\omega_{4,1,0})$	4	$(-11/4)*\omega_{Nr}$
$H_{PM}(P_{3,1,-1},\omega_{3,1,-1})$	$H_W(P_{8,1,0},\omega_{8,1,0})$	8	$(11/8)*\omega_{Nr}$
$H_{PM}(P_{15,1,0},\omega_{15,1,0})$	$H_W(P_{4,1,1},\omega_{4,1,1})$	15	0
…	…	…	…

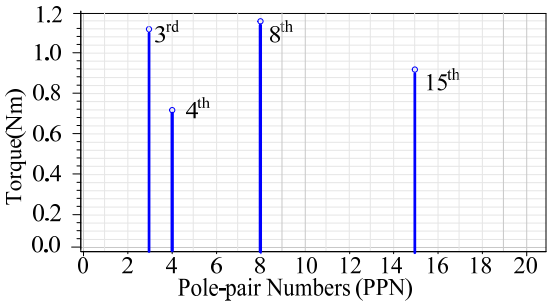

Fig. 2. 27. Torque components contributed by harmonics.

Table 2. 4 shows the effective harmonics and the Fig. 2. 27 shows the torque components contributed by harmonics. It is revealed that various harmonics have contributed to torque generation and the major harmonics are 3rd, 4th, 8th and 15th. This phenomenon is different from the traditional PMSMs and helps to understand the essential torque generating principle of these machines.

2.2.3 Performance of the 12/11 NNSS DSBFM

1) Design Parameters of the Prototype

The 12/11 NNSS DSBFM is selected as case study for verification of the theory of the biased flux machines. The definition of the design dimensions of the machine is shown in Fig. 2. 27, and the values of the key dimensions are listed in Table 2. 5.

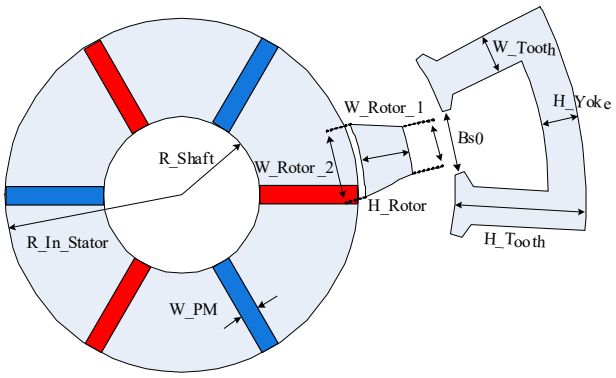

Fig. 2. 28. Diagram of the key design dimensions of NNSS-12-11 DSBFM

Table 2. 5 Key Design Dimensions of NNSS-12-11 DSBFM

Parameters	Dimension (mm)	Parameters	Dimension (mm)
R_Shaft	13.0	H_Yoke	7.0
R_In_Stator	29.5	W_Tooth	7.0
W_PM	3.0	H_Tooth	21.5
H_Rotor	8.0	Airgap_Inner	0.5
W_Rotor_1	9.3	Airgap_outer	0.5
W_Rotor_2	12.4	Outer Diameter	120
Bs0	10.5	Model Depth	55

Table 2. 6 gives the key design parameters of the machine. The rated speed is designed as 1000 rpm and the DC bus voltage is 24 V. The rated phase current (RMS) is 4.8 A and rated torque is 5.25 Nm. The slot space-factor, the conductor endings and the lamination stacking factor are all listed.

Table 2. 6 Key Design Parameters of NNSS-12-11DSBFM

Parameters	Value	Parameters	Value
DC bus Voltage	24 V	Winding Turns	35
Rated Speed	1000 rpm	Conductor Diameter	1.06mm
Rated Current (RMS)	7 A	Conductor End Length	16mm
Rated Torque	5.25Nm	Slot Area	260(mm)2
Rated Power	550W	Slot Space-Factor	0.8
Efficiency	>=86%	Lamination Stacking Factor	0.95
Surface Current Density	4.8A/(mm)2	Unload Magnetic Flux Density	1.5T

Fig. 2. 29 shows the prototype photographs. Fig. 2. 29 (a) to Fig. 2. 29 (d) is the rotor, inner stator, outer stator and top appearance. The salient rotor is fixed on the rings by bars and the inner stator is installed on the stator end plate. In order to test the coil back-EMF to verify the flux vector shown in Fig. 2.19, all endings of the coils are drawn out.

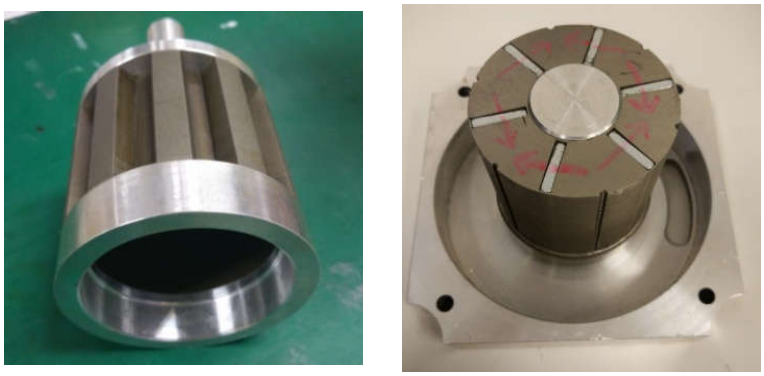

(a) Rotor. (b) Inner stator.

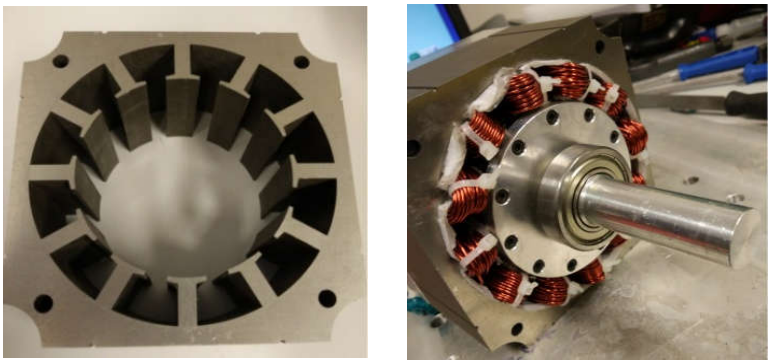

(c) Outer stator. (d) Top appearance.

Fig. 2. 29. Machine prototype.

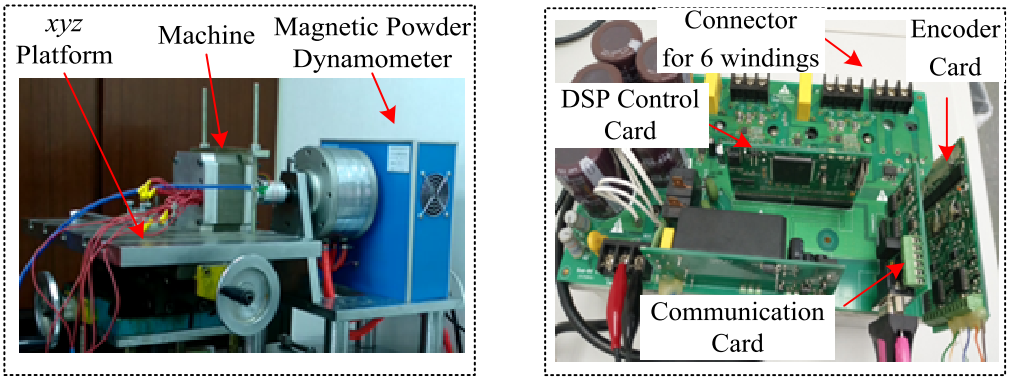

(a) Test apparatus. (b) Control board.

Fig. 2. 30. Experiment setup.

Fig. 2. 30 shows the experiment setup, where Fig. 2. 30(a) is the test apparatus and Fig. 2. 30(b) is the control board. The magnetic powder dynamometer serves as both the load and the torque measuring meter. For the control board shown in Fig. 2. 30(b), double three-phase inverters are applied to drive the six windings.

2) Biased Flux Waveforms

Under no-load condition, the flux is analyzed to demonstrate the principle of this machine. Fig. 2.

31shows the simulation results of exciting flux in winding A1, A2, B1, B2, C1 and C2. As analyzed above, the flux in the upper layer winding A1, B1 and C1 is with positive DC bias, while the flux in the lower winding is with negative DC bias. The simulation results indicate the biased flux characteristic of the BFMs.

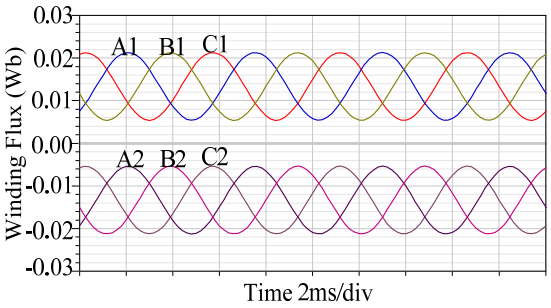

Fig. 2. 31. Simulated results of bidirectional flux bias in the proposed machine.

3) Back-EMF Waveforms

Fig. 2. 32(a) and Fig. 2. 32 (b) show the simulation and experimental waveforms of back-EMF in coils C_1, C_2 and C_3, and Fig. 2. 32(c) presents the corresponding FFT analysis. Ideally, the back-EMF in each coil should be sinusoidal waveform, and the phase difference for these three adjacent coils should be 120°. However, the back-EMF in single coil has many harmonics, as shown in Fig. 2. 32(c), which makes the waveforms distorted, and the phase difference shifted.

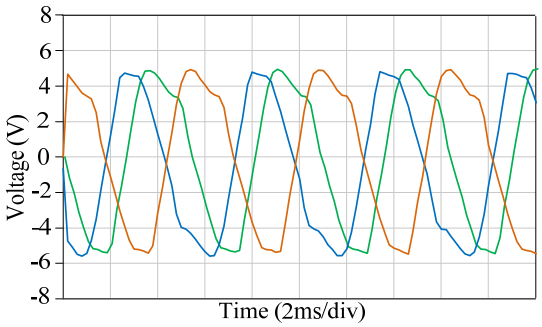

(a) Simulation results.

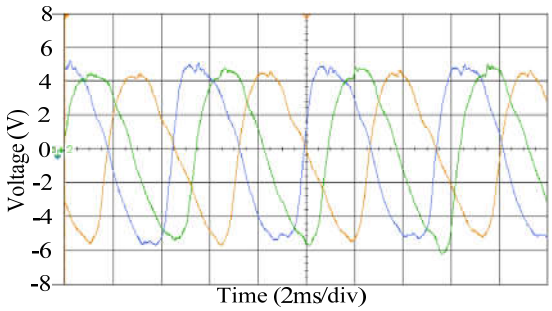

(b) Measured results.

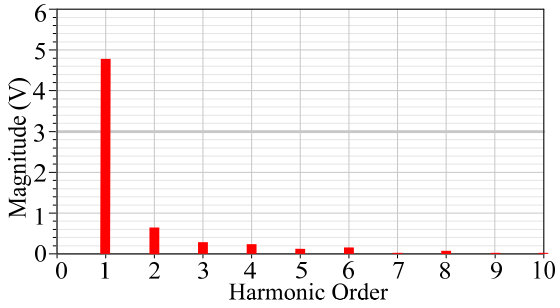

(c) FFT analysis for Back-EMF in C1.

Fig. 2. 32. Back-EMF waveforms of coils C1, C2 and C3.

Fig. 2. 33 and Fig. 2. 34 give the simulation and experimental results of the back-EMF waveforms in upper and lower layer windings. It is worth mentioning that the back-EMFs for windings in upper and lower layer have the complementary characteristic, which means the even order harmonics have the opposite phase positions. Therefore these even order harmonics could be cancelled when the windings in both upper group and lower group work together. For example, the back-EMFs for coil A1 and A2 are not well sinusoidal, but the combined back-EMF for Phase A is better.

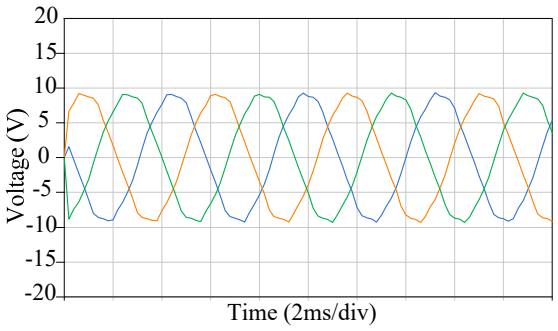

(a) Simulated results.

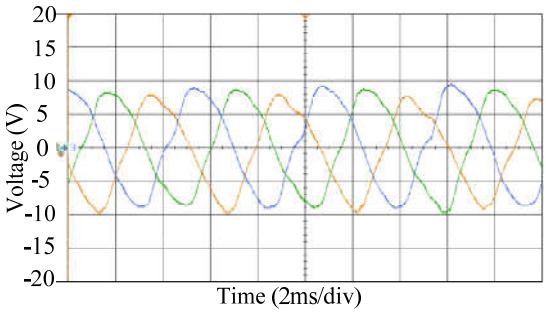

(b) Measured results.

Fig. 2. 33. Back-EMF waveforms of coil A1, B1 and C1.

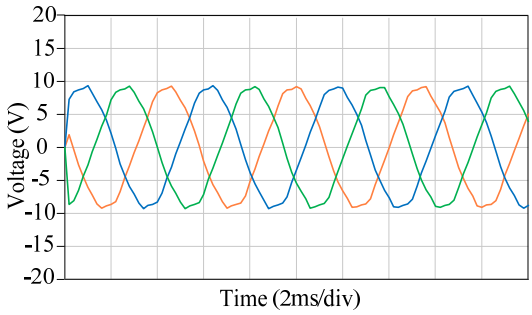

(a) Simulated results.

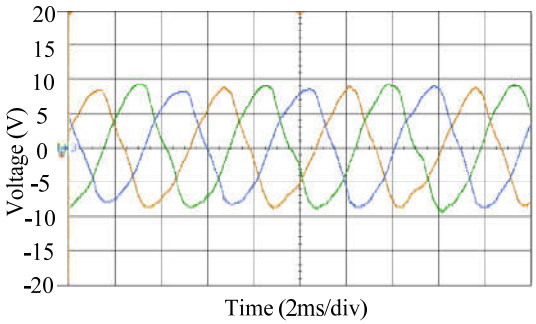

(b) Measured results.

Fig. 2. 34. Back-EMF waveforms of coil A2, B2 and C2.

Fig. 2. 35 shows the series-wound three-phase back-EMF waveforms. This back-EMF has a better sinusoidal waveforms, which comes from the complementary characteristics existed between the upper and lower windings.

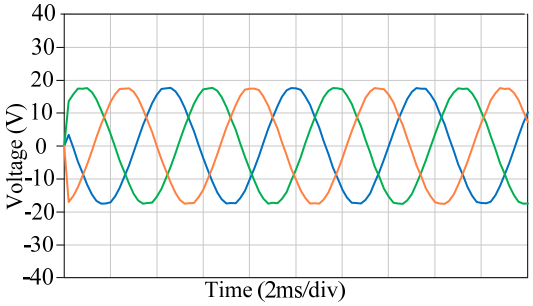

(a) Simulated results.

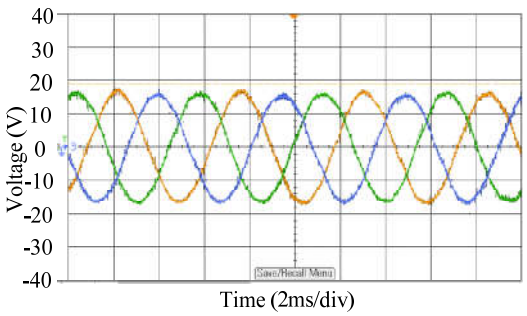

(b) Measured results.

Fig. 2. 35. Back-EMF waveforms of Phase A, B and C.

4) Inductance Characteritic

Based on the flux path for NNSS double stator BFMs, it could be derived that these machines have no mutual inductance, which means these machines are formed by independent single-phase machines. To introduce this characteristic, the simulation results of inductance waveforms for the proposed 12/11 NNSS DSBFM are presented in Fig. 2. 36. It is shown that compared with the self-inductance, the mutual-inductance is relative low and almost can be neglected, which matches the principle analysis well. With insignificant mutual inductance means the machine is formed by independent single phase machines. Actually, each basic single phase machine covers one PM piece, two stator teeth and two coils. With this structure, the flux path for these machines is very short, as it only goes through two adjacent coils.

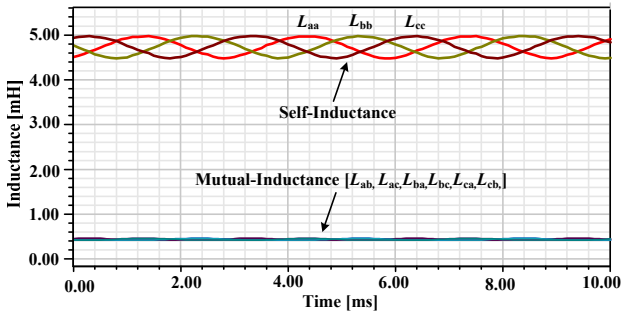

Fig. 2. 36. Simulation results of inductance in NNSS-12-11 DSBFM

Two merits could be obtained by this design. Firstly, short flux path means the small leakage flux, so the PM utilization factor can be high. Secondly, these machines are easily to be designed as modularized machines or multi-phase for some special applications because there is no mutual effect among the phases.

5) Torque Performance

The torque performances including unloaded cogging torque, rated torque, flux-weakened torque and flux-strengthened torque are presented.

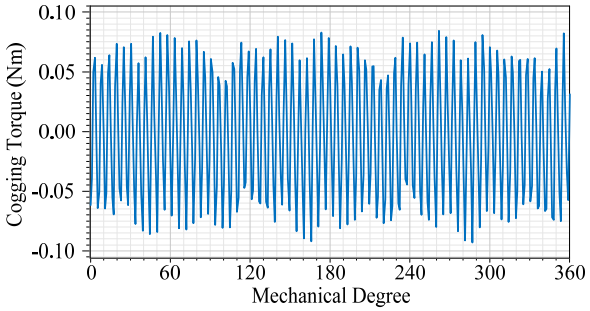

Fig. 2. 37. Simulation result of cogging torque.

Fig. 2. 37 gives the simulation result about the cogging torque. Due to the complementary relative locations of the rotor teeth and stator, the cogging torque for this salient machine is small, with less than 0.2 Nm peak-peak value.

Fig. 2. 38 gives the waveforms of adjusting exciting magnetic field with biased current. In normal operation when DC current component is zero, the torque for this exampled machine is 5.25 Nm. When DC current is -5 A, the exciting magnetic field is weakened, as the torque descends to 3 Nm. When DC

current is 5 A, the exciting magnetic field is strengthened, as the torque increases to 6 Nm. This example has proved that adjusting the exciting magnetic field with biased current is practical. Noticeably, the torque ripple is slightly high under rated condition, which is caused by the by PWM control, unbalanced magnetic force and the bearing tolerance.

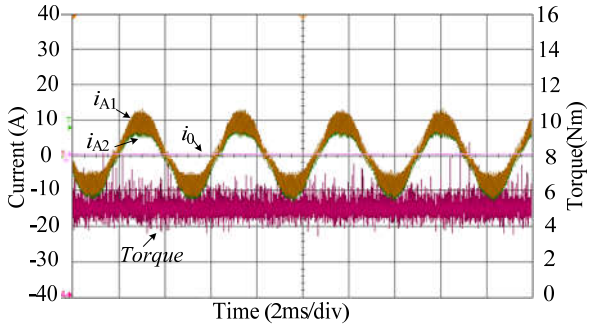

(a) Normal control with AC current.

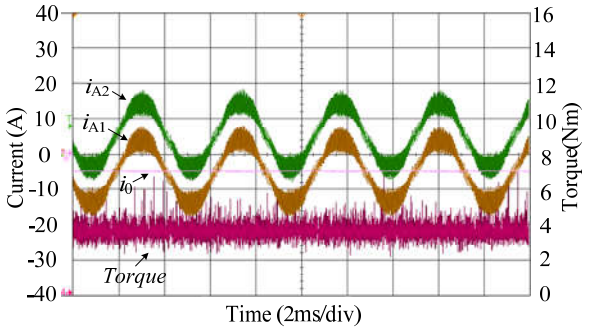

(b) Flux weakening control with negative DC current.

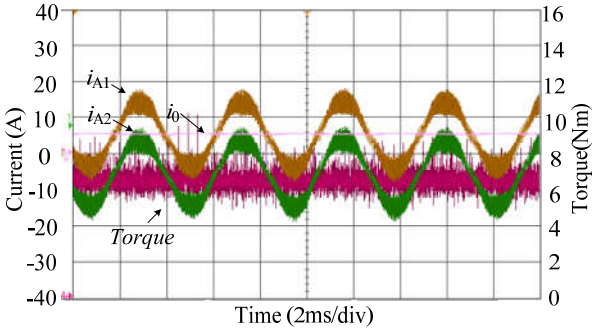

(c) Flux strengthening control with positive DC current.

Fig. 2. 38. Diagram of modulating exciting field with biased current.

6) Efficiency

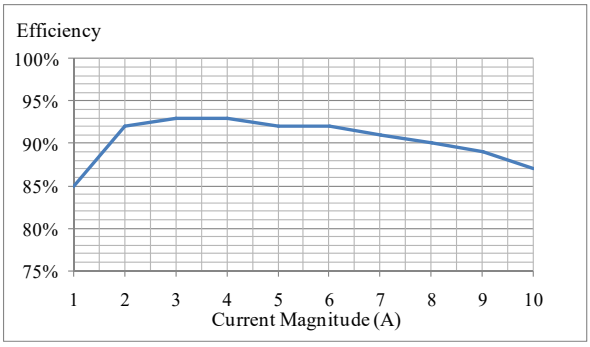

Fig. 2. 39. Measured efficiency under rated speed.

The efficiency under rated constant speed and variable loads is tested and shown in Fig. 2. 39. The efficiency is higher than 85% in whole range and can reach higher than 90% in middle loaded range.

2.3 Control of BFMs Based on Zero-Sequence Current

The major characteristic of BFM is that they can be controlled by the biased current to realize the special flux regulation control. Fig. 2. 40 gives the control diagram for the corresponding circuit in Fig. 2.15 (b) for NNSS 12/11 DSBFM. Different from the traditional SVPWM control, there is one additional variable is controlled, which is the zero-sequence-current. In the six-phase converter, zero-sequence-current passes through the double layers of the windings.

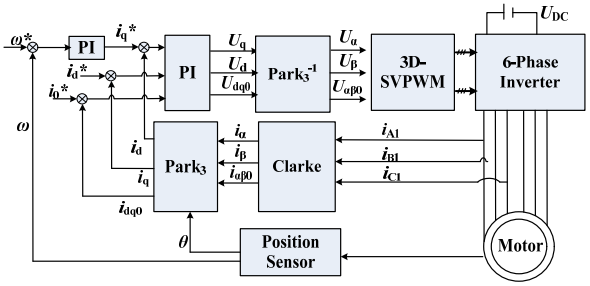

Fig. 2. 40. Control diagram of the biased flux machine based on zero-sequence current.

Two more basic voltage vectors should be used to realize the zero-sequence current control, which are the U_0+ and U_0- to generate the positive and negative zero-sequence-current. In Fig. 2. 40 U_0+ means the state of S_1, S_3, S_5 on and S_2, S_4, S_6 off while U_0- means the state of S_1, S_3, S_5 off and S_2, S_4, S_6 on.

Similar with the d-axis and q-axis current, the zero-sequence-current is also controlled by the PI regulators. With the zero-sequence-current, the total sum of the three-phase current does not equal to zero anymore, so three current sensors instead of traditional two should be used to detect the current, which may increase the drive cost slightly.

Firstly, implement the coordinate system transforming for the sampling phase current to get i_d, i_q and i_{dq0}, which includes two steps, using the Clarke and $Park_3$ transformer respectively. Because the zero sequence current is not zero, the Clarke transformer can be expressed as:

$$\begin{bmatrix} i_\alpha \\ i_\beta \\ i_{\alpha\beta 0} \end{bmatrix} = \sqrt{\frac{2}{3}} \begin{bmatrix} 1 & -\frac{1}{2} & -\frac{1}{2} \\ 0 & \frac{\sqrt{3}}{2} & -\frac{\sqrt{3}}{2} \\ \frac{1}{\sqrt{2}} & \frac{1}{\sqrt{2}} & \frac{1}{\sqrt{2}} \end{bmatrix} \begin{bmatrix} i_A \\ i_B \\ i_C \end{bmatrix} \tag{2-15}$$

Park transformer is expanded to 3×3 matrix, as shown in (2-15). Therefore the third variable zero sequence current can be processed.

$$\begin{bmatrix} i_d \\ i_q \\ i_{dq0} \end{bmatrix} = \begin{bmatrix} \cos\theta & -\sin\theta & 0 \\ \sin\theta & \cos\theta & 0 \\ 0 & 0 & 1 \end{bmatrix} \begin{bmatrix} i_\alpha \\ i_\beta \\ i_{\alpha\beta 0} \end{bmatrix} \tag{2-16}$$

Secondly, the PI regulator is used to do the closed-loop for speed and current control. Different from the traditional vector control, there is an additional variable i_0 to be controlled to regulate the excited flux linkage. Operating with the i_0 control, the capability of this machine for adjusting flux linkage gets strengthened. As a result, it can operate in wide speed range. i_0* has the higher priority to modulate the flux linkage, because it controlled the flux directly, equal to additional excitation DC machine when i_d=0. However, injecting DC component will raise the current peak value, while the current reaches the limitation of the converter, the i_0* can not be raised further. At this stage, i_d* is continue used to modulate the flux linkage.

Thirdly, using $Park_3^{-1}$ to get U_α, U_β and $U_{\alpha\beta 0}$, then sending them to the proposed 3-D SVPWM module to produce the two groups trigger signals. The 6-Phase inverter is used to drive the double layers windings. The details of the 3-D SVPWM will be introduced next.

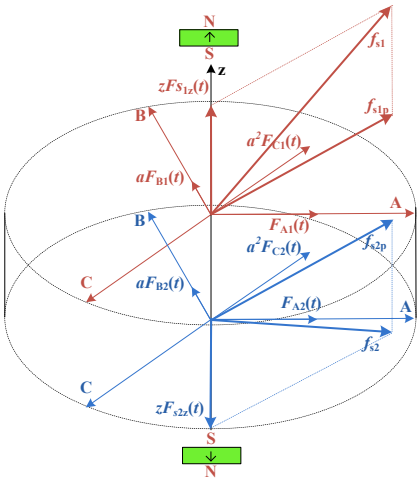

Fig. 2. 41. Space flux linkage model of the proposed control system.

Under this control, the space flux linkage model of this machine is shown in Fig. 2. 41. Because there are double layers of windings, the space vectors are expanded into three dimension, two planes are needed to express flux vectors. In the upper layer, the stator flux $\boldsymbol{f}_{s1}$ can be expressed as:

$$\boldsymbol{f}_{s1} = a^0 F_{A1}(t) + aF_{B1}(t) + a^2 F_{C1}(t) + \mathbf{z}F_{s1z}(t) = \boldsymbol{f}_{s1p} + \mathbf{z}F_{s1z}(t) \tag{2-17}$$

Where a^0, a, a^2 is space operator, $F_{A1}(t)$, $F_{B1}(t)$ and $F_{C1}(t)$ is the flux amplitude of stator winding A_1, B_1

and C_1, $\mathbf{z}$ is the vertical unite vector, $F_{s1z}(t)$ is the flux amplitude produced by the zero sequence current, $\boldsymbol{f}_{s1p}$ is the projection of $\boldsymbol{f}_{s1}$ in plane one. Similarly, in the lower layer, the stator flux $\boldsymbol{f}_{s2}$ can be expressed as:

$$\boldsymbol{f}_{s2} = a^0 F_{A2}(t) + aF_{B2}(t) + a^2 F_{C2}(t) + \mathbf{z}F_{s2z}(t) = \boldsymbol{f}_{s2p} + \mathbf{z}F_{s2z}(t) \tag{2-18}$$

where $F_{A2}(t)$, $F_{B2}(t)$ and $F_{C2}(t)$ is the flux amplitude of stator winding A_2, B_2 and C_2, $\boldsymbol{f}_{s2p}$ is the projection of $\boldsymbol{f}_{s2}$ in plane one. $F_{s2z}(t)$ is the flux amplitude produced by the zero sequence current. $\boldsymbol{f}_{s2p}$ is the projection of $\boldsymbol{f}_{s2}$ in plane two.

As mentioned before, the phase currents in two layers include DC and AC component, AC is used to produce the rotational flux $\boldsymbol{f}_{s1p}$ and $\boldsymbol{f}_{s2p}$. Because both the rotational fluxes are synchronous to the rotor, $\boldsymbol{f}_{s1p}$ must be equal to $\boldsymbol{f}_{s1p}$ strictly. The vertical flux $\mathbf{z}F_{s1z}(t)$ and $\mathbf{z}F_{s2z}(t)$ are caused by DC current, which is used to modulate the excited flux. The DC current is flowing from layer one into layer two, so the amplitudes of $\mathbf{z}F_{s1z}(t)$ and $\mathbf{z}F_{s2z}(t)$ are the same while the directions are opposite, as shown inFig. 2. 41.

Considering the connecting pattern of windings in layer one and layer two, the influence of the vertical fluxes keeps the same. Which means $\mathbf{z}F_{s1z}(t)$ and $\mathbf{z}F_{s2z}(t)$ weakens or strengthens the excited flux consistently.

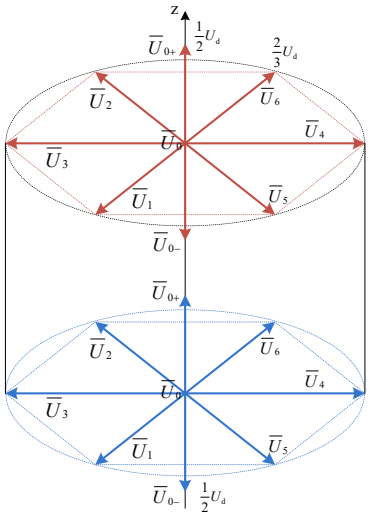

Fig. 2. 42. Basic space voltage vectors.

3-D SVPWM is the core of the control diagram, which is used to produce the two group drive signals according to U_α, U_β and $U_{\alpha\beta0}$. Different from the traditional SVPWM, another variable $U_{\alpha\beta0}$ is needed to be considered, since the reference U_{ref} has been expanded into three dimension from $\alpha\beta$ plane. Accordingly, additional basic vectors U_{0+} and U_{0-} are needed. The basic vectors are shown in Fig. 2. 42, there are U_1 to U_6 vectors in both upper and lower layer and U_0, U_{0+} and U_{0-} between the layers in z axis.

There is no difference between U_1 to U_6 and the traditional ones, thus their magnitude is $2U_{DC}/3$. What is noteworthy is the U_0, U_{0+} and U_{0-} vectors. Defining U_0 as the status of all the switches been turned off, U_{0+} of all upper switches been turned on and all lower switches been turned off, U_{0-} of all upper switches been turned off and all lower switches been turned on. Under this definition, the magnitude of U_0 is zero, U_{0+} and U_{0-} is $U_{DC}/2$. Because the DC current in two layers has the same magnitude, U_{0+} and U_{0-} should be used in combination. When upper layer uses U_{0+}, lower layer uses U_{0-}, so does in the reversed situation.

How to calculate the implemented time of the basic vectors according to the references will be introduced below. Take the upper layer for example, assuming the rotor is located in section three, U_4, U_6 and U_{0+} should be used to compound the reference U_{ref}, as shown in Fig. 2. 43. Where, U_{ref} can be compounded by vector U_{P} in $\alpha\beta$ plane and $U_{\alpha\beta0}$ in z axis, and U_{P} can be further decomposed by U_α and U_β.

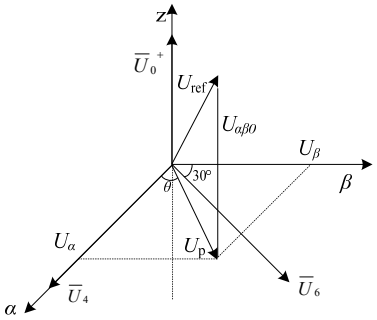

Fig. 2. 43. Composing reference vector using basic vectors

In the control diagram, U_α, U_β and $U_{\alpha\beta0}$ has been given as the reference, so next is to calculate the basic voltage vectors implemented time by them. According to the vector synthesis principle, implemented time of U_4, U_6 and U_{0+} and U_0 can be calculated by (2-19).

$$\begin{cases} T_6 = \sqrt{3}\dfrac{T_{\text{s}}}{U_{\text{DC}}} U_{\beta\text{ref}} \\ T_4 = \dfrac{T_{\text{s}}}{2U_{\text{DC}}}(3U_{\alpha\text{ref}} - \sqrt{3}U_{\beta\text{ref}}) \\ T_{0+} = T_{0-} = \dfrac{2U_{\alpha\beta0}}{U_{\text{DC}}} \\ T_0 = T_{\text{s}} - T_4 - T_6 - T_{0+} \end{cases} \tag{2-19}$$

To reduce the switching losses, seven-segment PWM is used in this chapter. Transfer the vector implemented time into PWM starting moment t_{A1on}, t_{B1on}, t_{C1on}, t_{A2on}, t_{B2on} and ending moment for t_{A2off}, t_{B2off}. In one switching period, the vectors operating order and interval is presented in Fig. 2. 44. The starting and ending moment for the switches are given in (2-20).

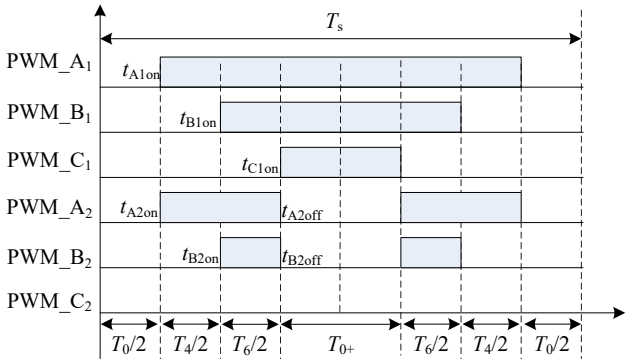

Fig. 2. 44. Seven-segment PWM signals in section three.

$$\begin{cases} t_{\text{A1on}} = t_{\text{A2on}} = 0.5T_0 \\ t_{\text{B1on}} = t_{\text{B2on}} = 0.5(T_0 + T_4) \\ t_{\text{C1on}} = t_{\text{C2on}} = 0.5(T_0 + T_4 + T_6) \\ t_{\text{A2off}} = t_{\text{B2off}} = 0.5(T_0 + T_4 + T_6) \end{cases} \tag{2-20}$$

It is shown that, the intervals for U_4 and U_6 are the same, so the AC currents in two layers are controlled to keep the same. The intervals for U_{0+} and U_{0-} are complementary, so the DC current in two layers are opposite. Since the drive signals in two layers are consistent and complementary, only one layer currents needs to be sampled present the feedbacks.

By using the proposed 3D-SVPWM control, the simulation results are presented to verify the feasibility and effectiveness of the integrated excitation control.

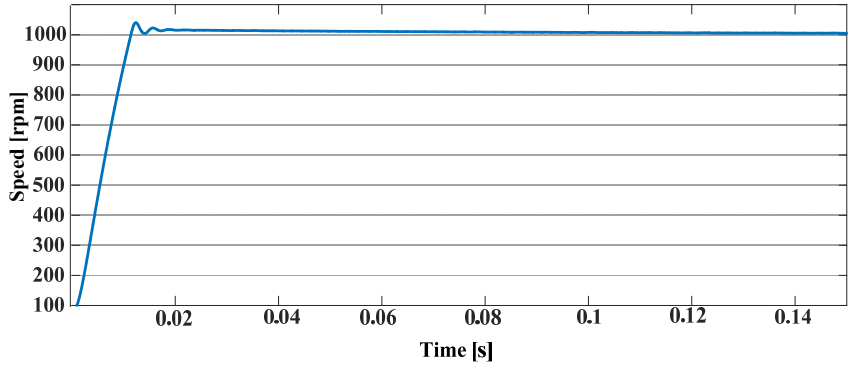

Fig. 2. 45. Speed waveform of the proposed system.

Fig. 2. 45 shows the speed waveform when the machines starts from 0 to rated 1000rpm. It is shown that the speed can reach the steady state of 1000 rpm, and the dynamic response process is good.

Fig. 2. 46 and Fig. 2. 47 shows the waveforms of six phase current and electromagnetic torque when the machines operating in the rated situation. The rated speed is 1000 rpm, the rated current is 10A and the rated torque is 5.25 Nm. In rated situation, there is no flux weakening control, so the current of two layers is the same, there is no zero sequence current, as shown in Fig. 2. 46. The current is sinusoidal waveform with few harmonic components, which means the 3D-SVPWM is feasible. Under rated situation, the electromagnetic torque is 5.25Nm, as shown in Fig. 2. 47. The Matlab simulation results agree well with the finite element analysis, which means the mathematical model of the control system is accurate.

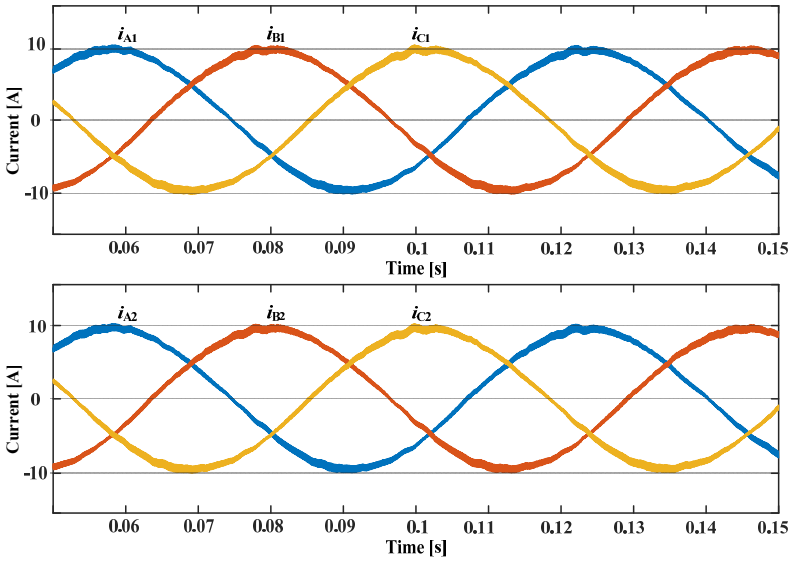

Fig. 2. 46. Six phase current at rated situation.

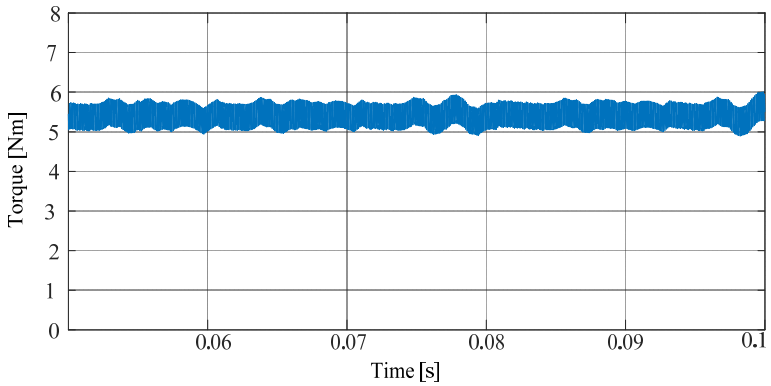

Fig. 2. 47. Rated torque waveform.

To verify the algorithm of the zero sequence injection, one example waveform of the six phase current under the flux weakening control is presented in Fig. 2. 48. The I_{dc} is -5A while the I_{ac} is rated 10A. It is shown that upper layer windings current of phase A1, B1 and C1 is moved down, with the maximum value of 5A and minimum value of -15A. The biased DC current is -5A, which realizes the desired control.

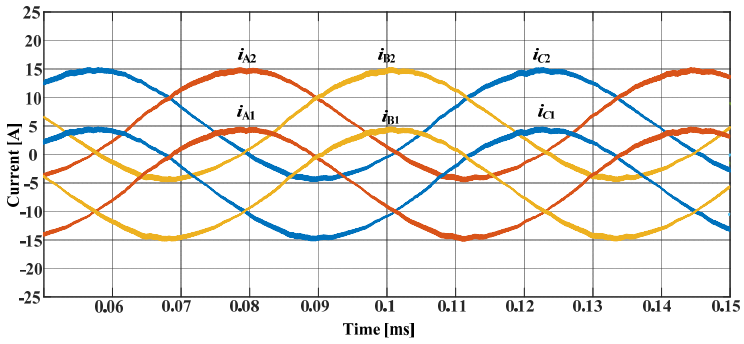

Fig. 2. 48. Six phase current under flux weakening control.

Lastly, the effectiveness of the integrated excitation control is demonstrated. Two simulations are conducted for comparison, as shown in Fig. 2. 49, the first read line is the natural output mechanical character of NNSS 12/11 DSBFM, while the blue line represents the one under the proposed integrated excitation control.

It is seen, for the natural output mechanical character, the cut-off speed is 1100 rpm and the cut-off torque is 3.8 Nm, the speed can not increase anymore without flux weakening control. For the integrated excitation control with zero sequence current I_0, the speed range can be extended into 1800rpm, and the cut-off torque is 3.5 Nm.

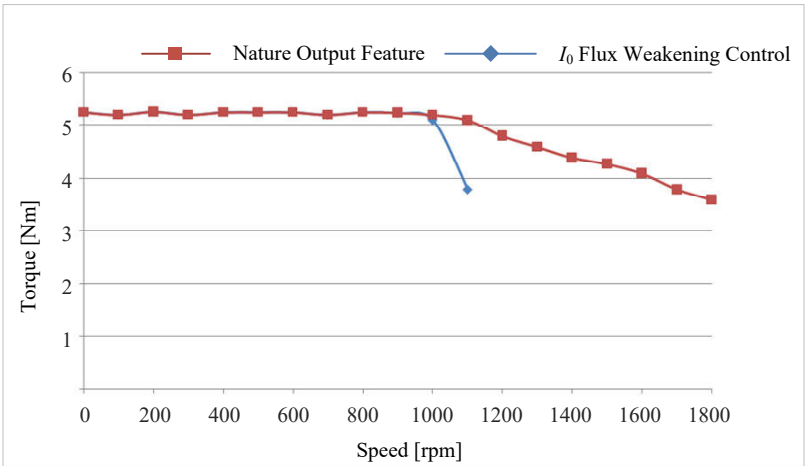

Fig. 2. 49. Effectiveness of the integrated excitation control.

It is demonstrated that, there are three features of this control. (1) The proposed flux weakening control is universal to all the BFMs, which covers massive of machines of different structure. (2) The proposed method is feasible and effective in the selected subject DSDSM, the machine speed is extended 1.63 times. (3) There is no field winding anymore. Therefore, no additional control circuit is needed. The system cost is reduced.

2.4 Extend the Biased Flux Concept into Other Machines

The basic concept of biased flux machines is to construct biased flux in the windings so biased current could be used for driven. Actually, this concept can be extended into many other machines besides the studied NNSS double stator BFMs. In this part, this BFM concept is extended into other machines to design the more general biased flux machines. One novel BFM with double salient structure is taken for example to demonstrate the principle.

Fig. 2. 50 shows the topology of the proposed double salient BFM (DSBFM). The stator has 12 teeth and the rotor has 11 teeth. The coils apply the concentrated distribution and the adjacent coils have the opposite wound direction. Different from the traditional three phase machines, the six windings labeled with A_1, A_2, B_1, B_2, C_1 and C_2 are separated into two layers and connected in the way shown in Fig. 2.15(b). The conductor distribution is shown in Fig. 2. 50. Noticeably, this novel pattern is different from the traditional winding connecting ones in the permanent magnet synchronous machines.

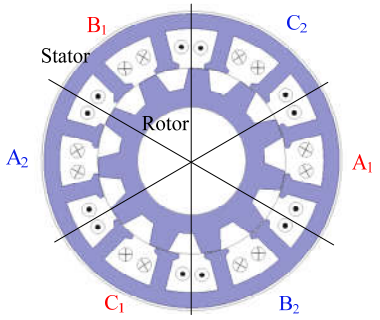

Fig. 2. 50. Topology of the proposed DSBFM.

The key for this machine is to use biased current to produce both the exciting flux and the armature flux. Actually, the biased current includes two component, namely AC and DC component. The DC component is used to produce the exciting flux while the AC component is used to generate armature flux to interact with the exciting flux to create torque.

To generate biased current, six windings belonging to three phases are connected as shown in Fig. 2.15(b) and double three-phase inverters are used. For the upper layer windings A_1, B_1 and C_1, positive DC current is used to create exciting flux and for lower layer windings A_2, B_2 and C_2, negative DC current is used. To reveal the operation principle of this DSBFM, Fig. 2. 51 presents the exciting flux distribution when only the DC current is used.

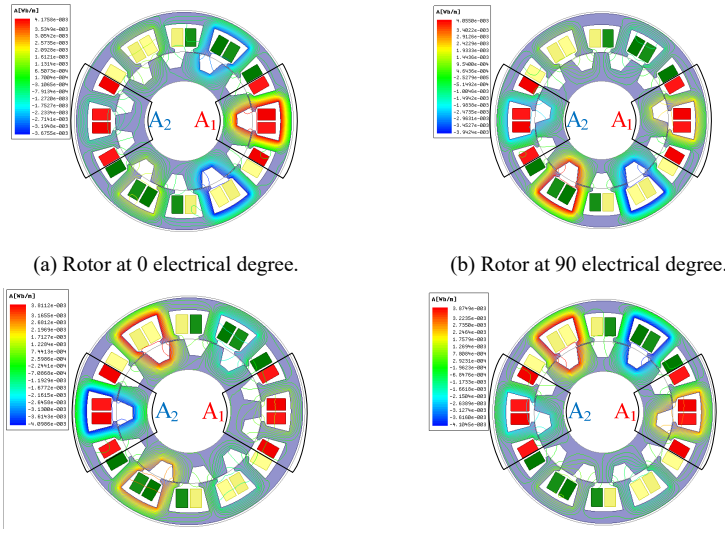

(a) Rotor at 0 electrical degree.

(b) Rotor at 90 electrical degree.

(c) Rotor at 180 electrical degree.

(d) Rotor at 270 electrical degree.

Fig. 2. 51. Exciting flux distribution of DSBFM.

When the rotor moves to 0 electric degree, two rotor teeth are aligned with the stator teeth wound with winding A_1 so the flux in A_1 gets maximum. On the other hand, the stator teeth wound with winding A_2 are unlighted with rotor teeth so flux in A_2 gets minimum value. Meanwhile, because the polarities of the DC current in A_1 and A_2 are opposite with each other, so their flux is also with different polarity. When the rotor moves to 90 electrical degrees, the rotor teeth has half aligned with both A_1 and A_2, so the flux in A_1 and A_2 get its half value. When rotor moves to 180 electrical degrees, the situation is opposite to that in Fig. 2. 51 (a), as A_1 gets its minimum value and A_2 get its maximum value. Fig. 2. 51(d) shows opposite position of Fig. 2. 51 (b). Fig. 2. 52 shows the winding flux waveforms for six windings. It is verified that the coil flux is biased and the phase difference for fundamental harmonic is 120°.

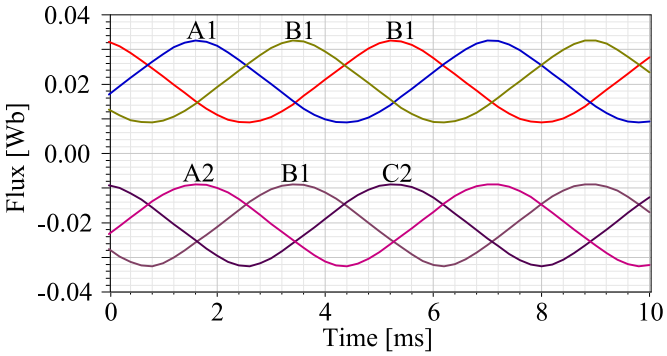

Fig. 2. 52. Winding flux for DSBFM when only DC current is used.

Fig. 2. 53 shows the back-EMF waveforms for six windings. It is shown that fundamental harmonics for upper and lower windings are the same and this machine is three-phase machine should be driven by three phase currents.

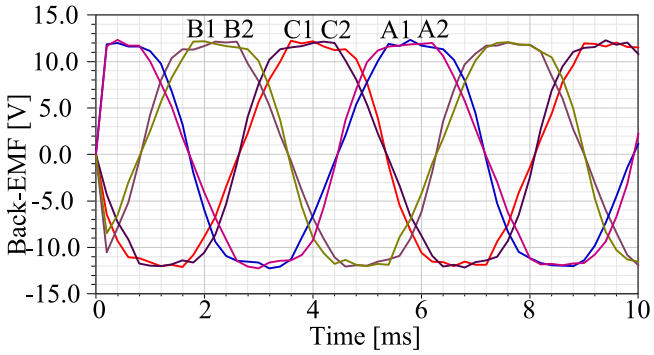

Fig. 2. 53.Winding back-EMF for DSBFM.

To evaluate the torque generating capability, the biased current shown in Fig. 2. 54 is injected into six windings. The DC component is used to produce exciting flux as mentioned and AC component is used to create torque. The key design parameters of this DSBFM are ted in Table 2. 7.

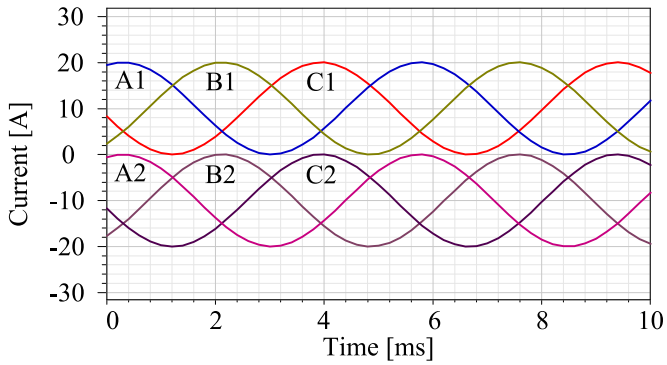

Fig. 2. 54. Biased drive current for DSBFM.

Table 2. 7 Key Design Parameters of This DSBFM

Parameters	Quantity
Rated Speed	500 rpm
Rated Torque	3 Nm
Out Diameter	120 mm
Axial Length	55 mm
Rated Phase Current	17 A (RMS)
Conductor Number	35
Slot Area	300$(mm)^2$
Coil Space Factor	0.7
Current Density in Copper	5.5 $A/(mm)^2$
Conductor Section Area	3 $(mm)^2$

Fig. 2. 55 shows the output torque waveform of this DSBFM, the rated torque is 3 Nm and the torque ripple takes about 20%.

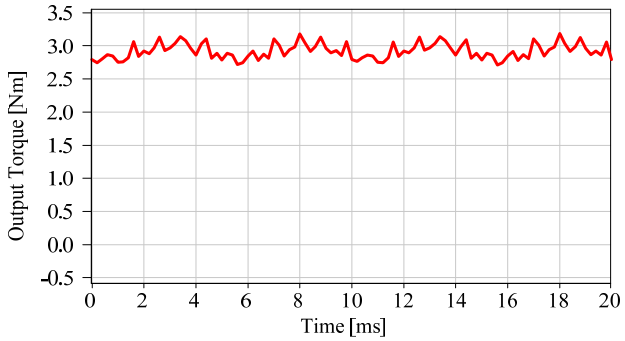

Fig. 2. 55. Output torque for DSBFM.

It is revealed that the principle of design BFM is feasible. The DC component of the drive current can work as the exciting source. Actually this exciting source can be used to generate exciting flux or modulate exciting flux to realize flux weakening or strengthening control. In this section, this method is expanded to other biased flux to demonstrate its advantages.

1) For PM Exciting Machines

Fig. 2. 56 shows the example of using this design method in PM exciting machine. It has been introduced in section II, DSM belongs to BFM, so definitely this design method can be used. Separate the windings into double layers, so the DC current can be injected into the windings with AC current. The DC component here can modulate the exciting flux to realize flux weakening or strengthening control.

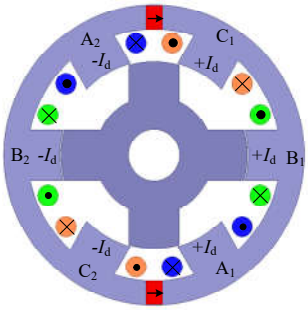

Fig. 2. 56. Example of using this design method in PM exciting machine.

2) For Hybrid Exciting Machines

Fig. 2. 57 shows the example of using this method in hybrid exciting machine. The hybrid exciting DSM also belongs to based flux machine, so the biased current can be used for drive to remove the DC exciting coils because it can modulate the exciting flux. In this way, the cost and efficiency of hybrid exciting machine can be improved.

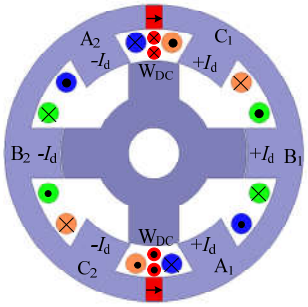

Fig. 2. 57. Example of using this design method in hybrid exciting machine.

3) For Electrical Exciting Machines

Fig. 2. 58 shows the example of using this design method in a electrical exciting machine (8/12 double salient machine) to remove the DC exciting coils. The principle is similar to that in hybrid machines. The additional exciting coils can be removed to give space for armature coils and the exciting flux can be modulated flexibly to improve the efficiency in wide speed range.

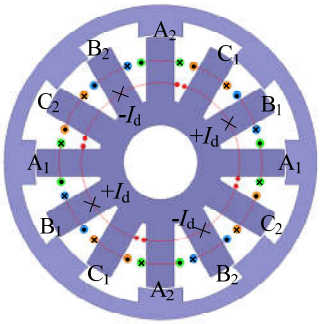

Fig. 2. 58. Example of using this design method in electrical exciting machine.

2.5 Conclusion

The definition of biased flux machine (BFM) is proposed in this chapter. Under that definition, two methodologies of design BFMs are proposed. One is based on the magnetic circuit, and the other is based on the magnetic field modulation theory.

A set of double stator biased flux machines (DSBFM) are proposed and their operation principle and performances of the BFMs are introduced in detail. Firstly, the fundamental principle of these machines is explained by using magnetic field modulation mechanism. It is revealed that various space harmonics of magnetic field have contributed to produce constant torque rather than fundamental one. The simulation and experimental results have verified the validity of this proposed method.

The control method for BFMs using zero-sequence current is introduced. It is demonstrated that this control has the following three features: 1) The proposed flux weakening control is universal to all the BFMs, which covers massive of machines of different structure. 2) The proposed method is feasible and effective in the selected subject BFMs, the machine speed is extended 1.6 times. 3) There is no field winding needed anymore. Therefore, no additional control circuit is needed. The system cost is reduced.

Additionally, the biased flux concept have been applied into design the other machines, to verify the feasibility of this method, a new non-PM 12/11 (stator teeth/rotor teeth) double salient biased flux is proposed for demonstration. It is shown that the performance of the double salient BFM driven by biased current is good. Moreover, the expanded applications of this method in other BFMs are presented. The advantages of this method can be summarized as: 1) For PM exciting BFMs, the biased current can be used to modulate the exciting flux, combing with negative d–axis current, it is more flexible to realize flux weakening or strengthening control. 2) For hybrid exciting or electrical exciting machines, the biased current can function as the DC windings, so the DC windings can be removed to give space for armature windings. This helps to reduce the cost and improve the efficiency of the machines. 3) This method is universal, which can be used in various machines as long as they agree with the definition of the BFMs.

Chapter 3 Design and Analysis of Doubly Complementary Machines

Stator-PM machines work on the principle that winding flux varies with the uneven permeance along air-gap caused by the salient rotor and stator teeth. In most literatures, obtaining maximum back-EMF by constructing the doubly salient structure is the only objective, which means the coil flux is usually well considered. This methodology merely focuses on the effective exciting flux going through coils but ignores the leakage flux which bypasses the coils. This is not adequate to determine the performance of electrical machines as the linkage flux usually will lower PM utilization and cause cogging torque. In this chapter, to improve PM utilization factor as well as reduce cogging torque, a new type of stator-PM machines namely stator-PM DCMs are proposed. The PM flux model for these machines is either short-circuit or open-circuit but a new switching circuit model. These machines apply the double complementary rotors so the PM flux could be switched between double rotors consecutively to avoid been shorted or opened. Meanwhile, the units belonging to same phases are also designed as complementary structures to reduce the back-EMF harmonics and improve torque density.

This chapter is organized as following. Section 3.1 introduces short-circuit and open-circuit model of stator-PM machines. Section 3.2 introduces the topology and principle of the proposed DCM. Secton 3.3 analyzes the specific characteristic of this machine. Section 3.4 presents the experimental verification, Section 3.5 introduces how to apply this concept to design axial flux machine and the conlclusions are drawn in Section 3.6.

3.1 Concept of Complementary Magnetic Path

In this part, a new perspective is provided to view the stator-PM machines. Instead of the effective exciting flux going through the coils, the leakage flux is focused. The effective flux passes through the coils undoubtedly while the leakage flux path varies for different machines. Based on the leakage flux path, most the stator-PM machines fall into the following categories, the ones with short-circuit model and the ones with open-circuit model.

3.1.1 Short-circuit Model

The diagram of stator-PM machines with short-circuit model is shown in Fig. 3. 1. Fig. 3. 1 (a) shows the position where PM flux passes the winding coils. At this position, the PM flux is desired to go through the coils as much as possible. Fig. 3. 1(b) shows the position where PM flux is shorted by the salient to minimize the coil flux.

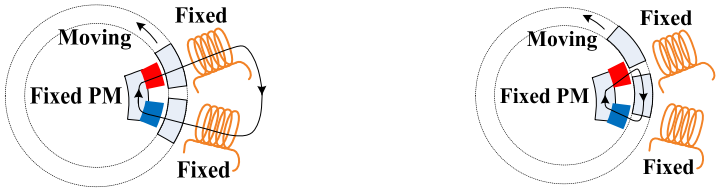

(a) Position of maximum flux in coils (b) Position of minimum flux in coils.

Fig. 3. 1 Diagram of short-circuit model for stator-PM machines.

Fig. 3. 2 shows some machines with this short-circuit model. The shorted PM flux is circled with dotted line for demonstration. Fig. 3. 2 (a) is the conventional flux switching permanent magnet (FSPM) machine, Fig. 3. 2 (b) the developed E-core FSPM, Fig. 3. 2 (c) the partitioned stator FSPM (PS-FSPM), and Fig. 3. 2(d) the double stator biased flux machine (DSBFM).

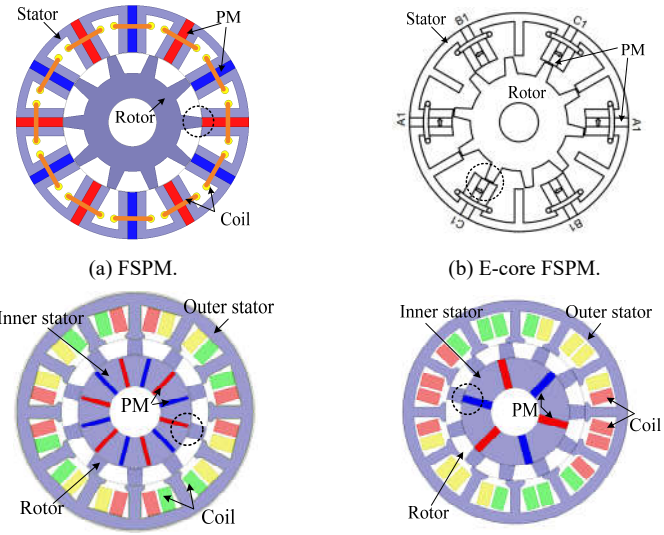

(a) FSPM. (b) E-core FSPM.

(c). PS-FSPM. (d) DS-BFM.

Fig. 3. 2. Stator-PM machines with short-circuit model.

The advantage of machines with short-circuit model is that the coil flux varies at large range to generate back-EMF since the PM flux is shorted at certain position. On the other hand, these machines have two major disadvantages, as the first one is low PM utilization factor and second one is the large cogging torque. For the first one, the shorted PM flux actually is wasted as it does not contribute to generate back-EMF. For the second one, since PM flux is shorted at certain position, the rotor would prefer these positions and cogging torque is caused.

3.1.2 Open-circuit Model

Some of the stator-PM machines have the open-circuit model, as shown in Fig. 3. 3. Fig. 3. 3(a) shows the way of coil flux getting maximum value, which is similar to that in short-circuit model. But the way for coils to get minimum flux is different, and as Fig. 3. 3(b) shows, the large reluctance is designed to evade the PM flux going through the coils but other paths instead.

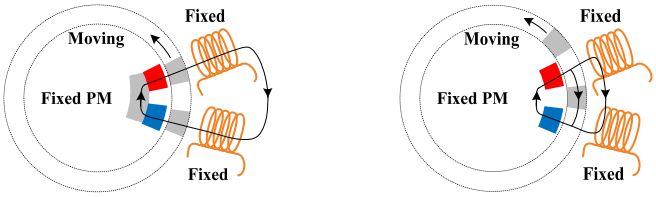

(a) Position of maximum flux in coils. (b) Position of minimum flux in coils.

Fig. 3. 3. Diagram of open-circuit model for stator-PM machines.

It is worth mentioning that some stationary DC winding exciting machines have the similar operation principle with the stator-PM machines, because PMs are simply replaced by the DC windings to work as the exciting source. So here some DC winding exciting machines are also discussed. Fig. 3. 4 shows some of the stator-PM and DC winding exciting machines with the open-circuit model. The open circuit for the exciting source is circled with the dotted line. Fig. 3. 4 (a) is the biased flux PM machine (BFPMM), Fig. 3. 4(b) the variable flux reluctance machine (VFRM), Fig. 3. 4(c) the non-overlapping stator wound field synchronous (NSWFS) machine , Fig. 3. 4 (d) the segment rotor NSWFS (SNSWFS).

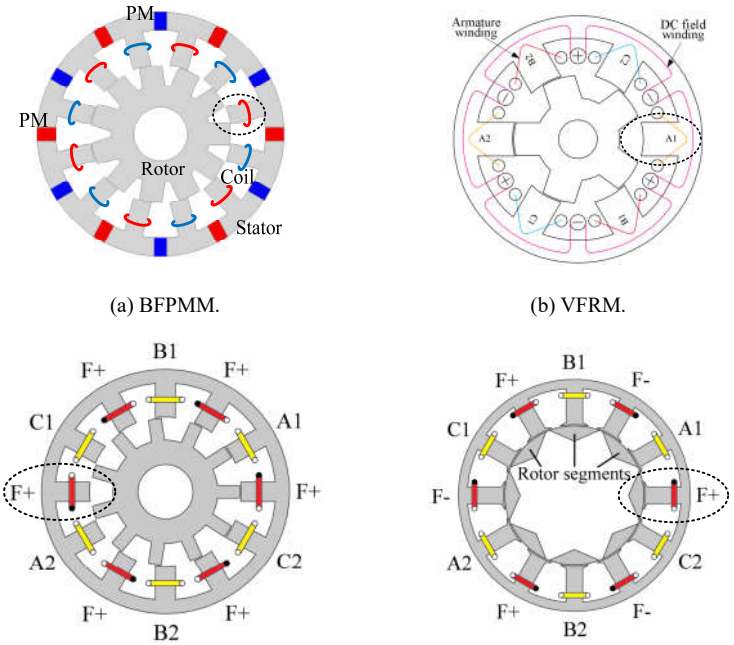

(a) BFPMM. (b) VFRM.

(c) NSWFS. (d) SNSWFS.

Fig. 3. 4. Stator-PM or DC winding exciting machines with open-circuit model.

The main advantage of these machines with open-circuit model is the low cogging torque because there is no special position where the reluctance is small and the rotor prefers. This characteristic is different with the machines with short-circuit model. However, the open-circuit feature also causes some disadvantages. The basic principle for these machines is to use the infinite reluctance to simulate the open-circuit, so the PM flux could be driven out from the coils. But actually, the reluctance is hard to be designed as infinite, and as Fig. 3. 3(b) shows, parts of the PM flux still go through the coils as leakage flux. This leakage flux will reduce peak-to-peak value of the back-EMF, lower PM utilization factor and thus undermine electromagnetic torque and efficiency. In short, machines with short-circuit model have the

disadvantages of low PM utilization factor and large cogging torque, while machines with open-circuit model have low PM utilization factor, relatively low electromagnetic torque and efficiency.

3.2 Design of a Novel Doubly Complementary Machine

3.2.1 Topology and Principle of the Proposed DCM

In this section, the topology, winding connection pattern and PM flux path is introduced to explain the principle of the proposed DCM. The topology of the proposed DCM is shown in Fig. 3. 5, as one stator and two rotors are involved. The stator has slots and teeth both inside and outside, correspondingly, the double synchronous rotors are located inside and outside of the stator. These double rotors are unified as ones with the cup shape and the stator is fixed in the end plate with bars. Noticeably, the double rotors are staggered with 180^{o} mechanical degree, which plays an significant role in constructing the doubly complementary characteristic. Six pieces of PMs are inset in the stator yoke and the adjacent ones are with opposite magnetizing directions, which are indicated by different color and arrow. This special combination of PMs and the stator teeth also contributes to the doubly complementary characteristic. The windings apply the concentrated distribution and the coils belonging to same phases are labeled with same color. The detailed winding connecting pattern is shown in Fig. 3. 6.

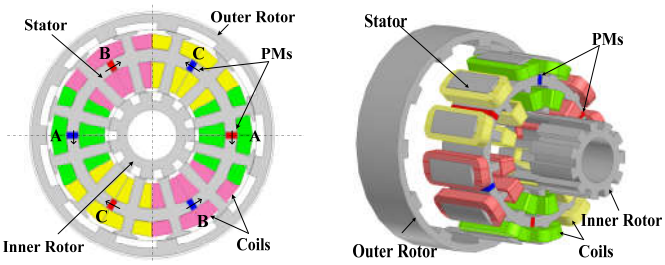

(a) Side view. (b) Exploded view.

Fig. 3. 5. Topology of the proposed DCM.

Fig. 3. 6 shows the winding connecting pattern for the DCM. Based on the PM locations, the windings are divided into six groups, namely group A_1, A_2, B_1, B_2, C_1 and C_2. For each group, the wingding is formed by four coils with two wound on outer teeth and two on inner teeth. The polarities of the conductors are distinguished with different symbols and the coils connecting pattern is identical for six windings. Finally, winding A_1, A_2, B_1, B_2 and C_1, C_2 are connected in series as phase winding A, B and C.

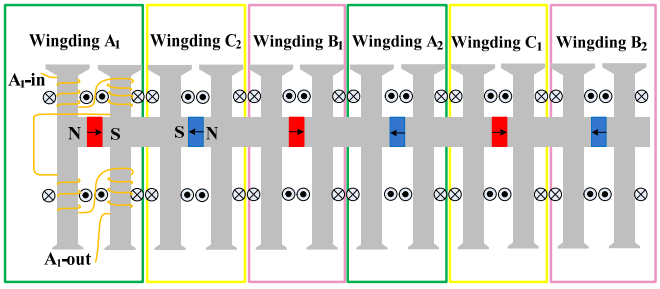

Fig. 3. 6. Winding connection pattern.

3.2.2 PM Flux Path of DCM

PM flux path is essential for electrical machines as it indicates their operation principle. Fig. 3. 7 shows the PM flux distribution for DCM with rotor at four different positions, and Fig. 3. 8 gives the diagram of the winding flux corresponding to Fig. 3. 7. Phase A is taken for example to for demonstration, where the coil flux in A_1, A_2 and A are represented by ψ_{mA1}, ψ_{mA2} and ψ_{mA}.

When θ_e equals zero in Fig. 3. 7 (a), two of the outer rotor teeth are aligned with the stator teeth wound with winding A_1. The PM flux goes through the outer rotor to form the closed loop, making ψ_{mA1} get maximum value. Meanwhile, due to complementary characteristic, two of the inner rotor teeth are aligned with the stator teeth wound with winding A_2. The PM flux goes through the inner rotor to form the closed loop. Due to the opposite magnetizing direction for the PMs under winding A_1 and A_2, ψ_{mA2} also gets its maximum, as shown in Fig. 3. 8. Then in Fig. 3. 7(b), when θ_e equals $\pi/2$, the PM flux goes half through the out rotor and half through inner rotor, making ψ_{mA1} and ψ_{mA2} equals zero. Fig. 3. 7(c) shows θ_e equals π, which is the opposite position of that in Fig. 3. 7(a), so ψ_{mA1} and ψ_{mA2} get their minimum value. Similarly, ψ_{mA1} and ψ_{mA2} get zero again in Fig. 3. 7 (d).

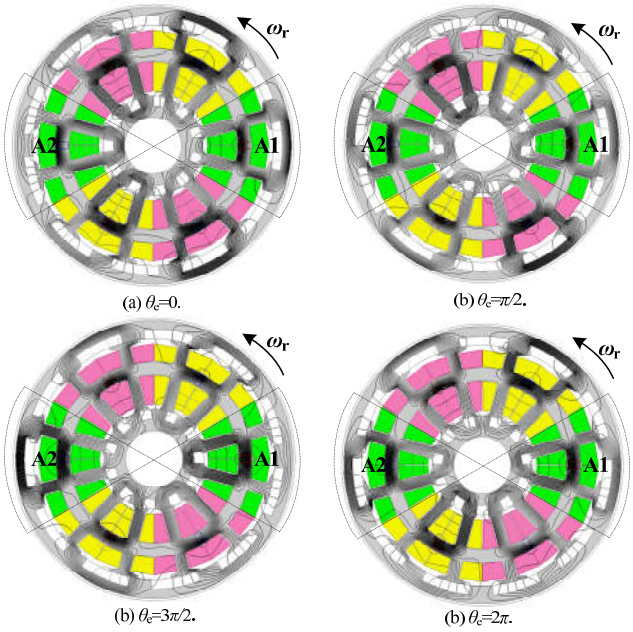

Fig. 3. 7. Open-circuit flux distribution.

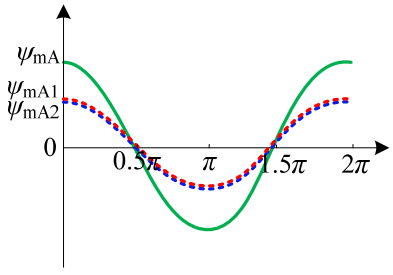

Fig. 3. 8. Flux in winding A_1, A_2 and A.

Noticeably, the PM-flux switches between the double rotors smoothly, without been shorted or open, contributing to the high PM utilization factor. Meanwhile, different from most of the stator-PM machines, the PM flux just passes through the coil belonging to the same phase. So essentially, there is no mutual inductance among different phases, this machine can be esteemed as three independent single phase machines. This helps to improve its fault-tolerant capability, and in extreme situation, it can work use just one single-phase winding.

3.3 Characteristics of the Proposed Doubly Complementary Machine

In this section, the detailed analysis for this machine is presented, including the doubly complementary characteristic, principle to construct the multiphase with different pole-pairs, torque characteristic and the advantage of this complementary characteristic.

3.3.1 Doubly Complementary Characteristic

1) Complementarity in Single Unit

The most outstanding characteristic of this machine is the doubly complementary characteristic. It is mentioned that this machine is formed by three independent phases, and each phase includes two units. The doubly complementary characteristic has twofold meaning, namely 1), there is complementarity in each unit; 2), these two units belonging to same phase are complementary.

Taking the unit wound with winding A_1 for example, Fig. 3. 9 shows the diagram of the complementarity in one single unit. When θ_e equals $\pi/2$, the outer rotor teeth are aligned with the stator teeth, so the PM flux goes through the outer rotor. When the rotor moves $\theta_e = \pi$, the PM flux goes through the inner rotor instead. Therefore, PM flux is switched between the double rotors smoothly without been shorted or opened. This is contributed by the double rotor structure and can be regarded as one complementary characteristic.

To further reveal this characteristic, the PM flux in the coils is analyzed. Dividing winding A_1 into two components-winding A_{11} and winding A_{12} as Fig. 3. 9 shows. Each winding includes the coils wound on two adjacent stator teeth. For the two coils in each winding, the PM flux going through them is totally the same, thus the flux in winding A_{11} and A_{12} are the minimum units.

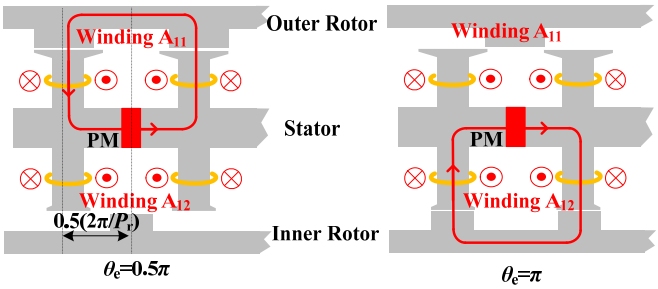

Fig. 3. 9. Diagram of complementarity in single unit.

To reveal the flux complementary characteristic in this unit, the open-circuit flux in winding A_{11}, A_{12} and A_1 is analyzed. Writing the flux in winding A_{11} as ψ_{mA11}, which can be expressed as (3-1):

$$\psi_{\mathrm{mA11}} = \psi_{\mathrm{DCA11}} + \sum_{n=1}^{+\infty} \psi_{\mathrm{ACA11}n} \cos(nP_{\mathrm{r}}\theta_{\mathrm{r}}) \tag{3- 1}$$

where, ψ_{DCA11} is the DC component, $\psi_{\mathrm{ACA11}n}$ is the magnitude of n^{th} harmonics, P_{r} is the rotor poles, and θ_{r} is the mechanical angle of the rotor.

The mechanical angle for the central line of outer rotor and inner rotor tooth is $(2\pi/P_{\mathrm{r}})/2$, and the flux direction in winding A_{12} is opposite to that in winding A_{11}. So the flux in winding A_{12} can be derived as:

$$\psi_{\mathrm{mA12}} = -\left\{ \psi_{\mathrm{DCA12}} + \sum_{n=1}^{+\infty} \psi_{\mathrm{ACA12}n} \cos\left(nP_{\mathrm{r}}(\theta_{\mathrm{r}} + \frac{1}{2}\frac{2\pi}{P_{\mathrm{r}}}) \right) \right\} \tag{3- 2}$$

where ψ_{DCA12} is the DC component, $\psi_{\mathrm{ACA12}n}$ is the magnitude of n^{th} harmonics, thus the flux in winding A_1 is:

$$\psi_{\mathrm{mA1}} = \psi_{\mathrm{mA11}} + \psi_{\mathrm{mA12}} = \psi_{\mathrm{DCA11}} - \psi_{\mathrm{DCA12}} + \sum_{n=2,4,6\ldots}^{+\infty} (\psi_{\mathrm{ACA11}n} - \psi_{\mathrm{ACA12}n}) \cos(nP_{\mathrm{r}}\theta_{\mathrm{r}}) + \sum_{n=1,3,5\ldots}^{+\infty} (\psi_{\mathrm{ACA11}n} + \psi_{\mathrm{ACA12}n}) \cos(nP_{\mathrm{r}}\theta_{\mathrm{r}}) \tag{3- 3}$$

According to (3-3), the DC component and the even order harmonics are mitigated due to the complementary rotors. Actually if the inner rotor and out rotor are identical without the arc, there are only the odd order harmonics. Anyway, the DC component and the even order harmonics of the flux in the final phase are still can be eliminated completely due to the complementarity in two units belonging to same phase.

2) Complementarity in Two Units Belonging to Same Phase

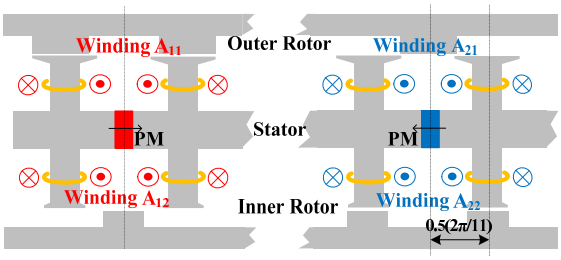

Fig. 3. 10. Diagram of complementarity in two units belong to same phase.

To explain the complementarity in two units belonging to same phase, the flux in winding A_1 is expressed as:

$$\psi_{\mathrm{mA1}} = \psi(\theta_{\mathrm{r}}) \tag{3- 4}$$

According to Fig. 3. 10, the angle difference for the rotor teeth of these two units is $(2\pi/P_{\mathrm{r}})/2$, and the PM magnetizing direction for them is opposite. So the flux in winding A_2 can be expressed as:

$$\psi_{\mathrm{mA2}} = -\psi\left(\theta_{\mathrm{r}} + \frac{1}{2}\frac{2\pi}{P_{\mathrm{r}}} \right) = -\psi_{\mathrm{DCA11}} + \psi_{\mathrm{DCA12}} - \sum_{n=2,4,6\ldots}^{+\infty} (\psi_{\mathrm{ACA11}n} - \psi_{\mathrm{ACA12}n}) \cos(nP_{\mathrm{r}}\theta_{\mathrm{r}}) + \sum_{n=1,3,5\ldots}^{+\infty} (\psi_{\mathrm{ACA11}n} + \psi_{\mathrm{ACA12}n}) \cos(nP_{\mathrm{r}}\theta_{\mathrm{r}}) \tag{3- 5}$$

Therefore, the phase flux for winding A can be derived as:

$$\psi_{\mathrm{mA}}=\psi_{\mathrm{mA1}}+\psi_{\mathrm{mA2}}=2\sum_{n=1,3,5\ldots}^{+\infty}(\psi_{\mathrm{ACA11}n}+\psi_{\mathrm{ACA12}n})\cos(nP_{\mathrm{r}}\theta_{\mathrm{r}}) \tag{3- 6}$$

It is shown in (3-6), the DC component and even order harmonics in phase flux are totally eliminated by the doubly complementary characteristics. With Y style connection, the 3rd harmonics are automatically eliminated, so the flux is almost the perfect sinusoidal waveform.

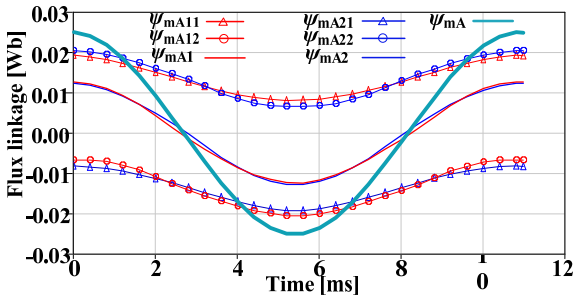

Fig. 3. 11. FEM simulation results of the open circuit winding flux.

To verify the analysis above, finite element method is used to simulate the open circuit flux in the windings of the built prototype. The winding flux waveforms are presented in Fig. 3. 11 and the corresponding FFT analysis is given in Fig. 3. 12. It is shown in Fig. 3. 11 that the phase flux ψ_{mA} has no DC component and even order harmonics at all, which is almost the perfect sinusoidal waveform. Actually, the coil flux ψ_{mA11} and ψ_{mA12} also have few harmonics, and their DC component magnitude is almost the same. This is contributed by the optimizing algorithm, as the optimizing objective is to reduce the flux harmonics to improve torque density.

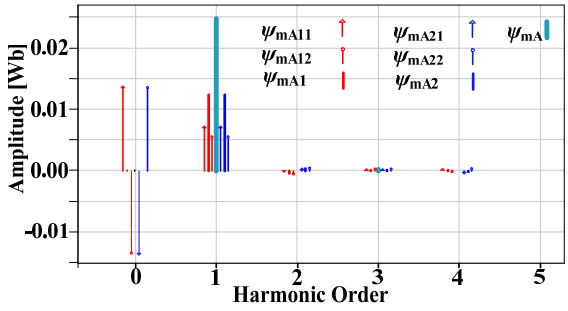

Fig. 3. 12. FFT analysis of the open circuit winding flux.

The doubly complementary characteristics not only influence the exciting flux, but also influence the armature reaction. To reveal this, the inductances are analyzed to indicate the armature reaction. Similarly, the inductances for the windings belonging to phase A are analyzed. Writing inductance in winding A_{11} as L_{11} which can be expressed as:

$$L_{\mathrm{A11}}=L_{\mathrm{DCA11}}+\sum_{n=1}^{+\infty}L_{\mathrm{ACA11}n}\cos(nP_{\mathrm{r}}\theta_{\mathrm{r}}) \tag{3- 7}$$

where, L_{DCA11} is the DC component, $L_{\mathrm{DCA11}n}$ the n^{th} harmonics. Similarity to (2), the inductance for winding A_{12} can be expressed as:

$$L_{\mathrm{A12}}=L_{\mathrm{DCA12}}+\sum_{n=1}^{+\infty}L_{\mathrm{ACA12}n}\cos\left(nP_{\mathrm{r}}(\theta_{\mathrm{r}}+\frac{1}{2}\frac{2\pi}{P_{\mathrm{r}}})\right) \tag{3- 8}$$

where, L_{DCA12} is the DC component, L_{DCA12n} the n^{th} harmonics. Thus the inductance for winding A_1 can be written as:

$$L_{A1} = L_{DCA12} + L_{DCA12} + \sum_{n=1,3,5...}^{+\infty} (L_{ACA11n} - L_{ACA12n})\cos(nP_r\theta_r) + \sum_{n=2,4,6...}^{+\infty} (L_{ACA11n} + L_{ACA12n})\cos(nP_r\theta_r) \quad (3\text{-}9)$$

Also defining L_{A1} as a function of θ_r written in (3-10), L_{A2} can be expressed as (3-11).

$$L_{A1} = L(\theta_r) \quad (3\text{-}10)$$

$$L_{A2} = L\left(\theta_r + \frac{1}{2}\frac{2\pi}{P_r}\right) = L_{DCA12} + L_{DCA12} - \sum_{n=1,3,5...}^{+\infty} (L_{ACA11n} - L_{ACA12n})\cos(nP_r\theta_r) + \sum_{n=2,4,6...}^{+\infty} (L_{ACA11n} + L_{ACA12n})\cos(nP_r\theta_r) \quad (3\text{-}11)$$

The final inductance for L_A can be expressed as:

$$L_A = L_{A1} + L_{A2} = 2(L_{DCA12} + L_{DCA12}) + 2\sum_{n=2,4,6...}^{+\infty} (L_{ACA11n} + L_{ACA12n})\cos(nP_r\theta_r) \quad (3\text{-}12)$$

It is shown that the odd harmonics are eliminated with only DC component and even harmonics remained. Fig. 3. 13 and Fig. 3. 14 present the simulation results of the winding inductances and their FFT analysis. Similar to the open circuit flux, the magnitude of high order harmonics are very small, so the phase inductance waveform is almost a straight line with only DC component.

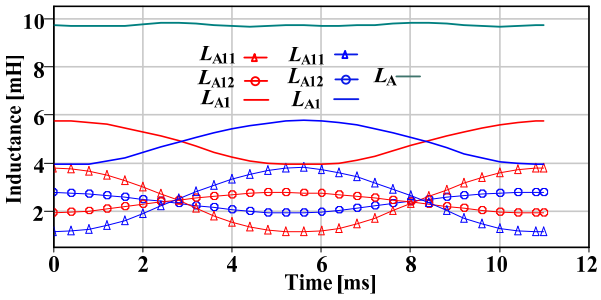

Fig. 3. 13. Simulation results of the winding inductance.

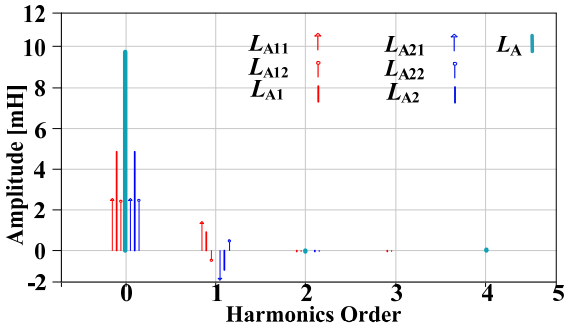

Fig. 3. 14. FFT analysis of the winding inductance.

The analysis results indicate that the inductance is a constant, so essentially, this machine has no salient effect although it has salient teeth in both stator and rotors. Its torque expression will be introduced later.

3.3.2 Principle of Constructing Multiphase with Different Rotor Poles

It is mentioned above, this machine is actually formed by three independent single phase machines. So the principle of constructing multiphase machines with different rotor poles should be addressed to reveal the general design rules of these machines.

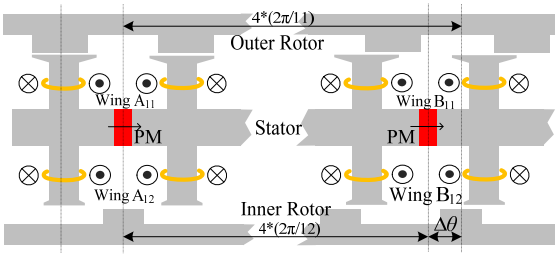

Fig. 3. 15. Diagram of the relationships between different phases.

Fig. 3. 15 shows the position relationship between the different phases. After $\Delta\theta$, the rotor teeth under winding B_1 get the same relative position of that in winding A_1, so the winding flux ψ_{mB1} can be expressed as:

$$\psi_{mB1} = \psi\left(\theta_r + 4(\frac{2\pi}{P_r} - \frac{2\pi}{N_s})\right) \tag{3- 13}$$

where N_s is the stator teeth number. Similarly, the flux in winding B_2 can be expressed as (3-14), and the final phase flux in winding B can be expressed as (3-15).

$$\psi_{mB2} = -\psi\left(\theta_r + \frac{1}{2}\frac{2\pi}{P_r} + 4(\frac{2\pi}{P_r} - \frac{2\pi}{N_s})\right) \tag{3- 14}$$

$$\psi_{mB} = 2\sum_{n=1,3,5...}^{+\infty}(\psi_{ACA11n} + \psi_{ACA12n})\cos n(P_r\theta_r + 8\pi\frac{N_s - P_r}{N_s}) \tag{3- 15}$$

In the same way, the exciting flux for winding C is derived as:

$$\psi_{mC} = 2\sum_{n=1,3,5...}^{+\infty}(\psi_{ACA11n} + \psi_{ACA12n})\cos n(P_r\theta_r + 16\pi\frac{N_s - P_r}{N_s}) \tag{3- 16}$$

Neglecting the high order harmonics, the exciting flux for phase A, B and C could be expressed by (3-17), where ψ_m is the magnitude of the fundamental harmonic.

$$\begin{cases} \psi_{mA} = \psi_m \cos P_r\theta_r \\ \psi_{mB} = \psi_m \cos(P_r\theta_r + 8\pi\dfrac{N_s - P_r}{N_s}) \\ \psi_{mC} = \psi_m \cos(P_r\theta_r + 16\pi\dfrac{N_s - P_r}{N_s}) \end{cases} \tag{3- 17}$$

According to (3-17), if the N_s and P_r are 12 and 11 applied in the built prototype, the phase difference among there three phases is 2π/3. The simulation result about exciting flux in three phases is shown in Fig. 3. 16.

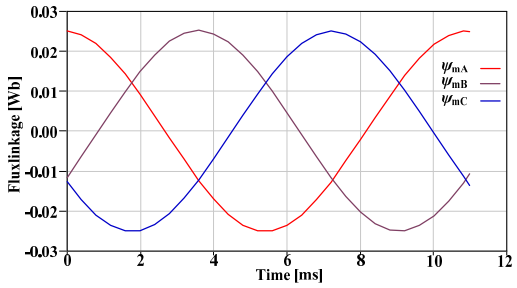

Fig. 3. 16. Simulation result of three phases exciting flux.

Furthermore, for three-phase machines, according to (3-17), the phase difference can be calculated by N_s and P_r. So the EMF vectors for the DCMs with different N_s/ N_r combinations are derived as shown in Fig. 3. 17.

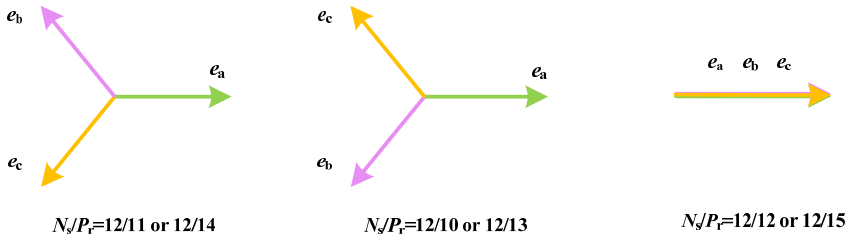

Fig. 3. 17. EMF vectors for DCM with different combinations of N_s/ N_r.

The construction of three phase DCMs is derived under the premise that there is no mutual inductance among different phases, which should be checked. So Fig. 3. 18 shows the simulation result of the self-inductance and mutual-inductances for the built machine. It is shown that the mutual-inductance is relatively small and can be neglected.

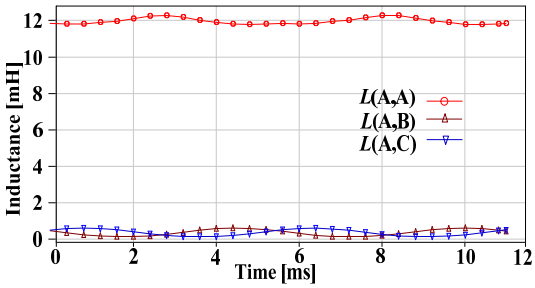

Fig. 3. 18. Simulation result of inductance for 12/11 DCM.

3.3.3 Torque Analysis for Proposed Three Phase 12-11 DCM

The basic formula to calculate the toque is presented by (3-18), taking (3-12) and (3-17) into (3-18), the torque of proposed 12/11 DCM can be expressed as (19), where I_{AC} is the amplitude of the AC current.

$$T = \frac{1}{2} i^2 \frac{\partial L}{\partial \theta} + i \frac{\partial \psi_m}{\partial \theta} \tag{3- 18}$$

$$T = T_A + T_B + T_C = -\frac{3}{2} P_r \psi_m I_{AC} \tag{3- 19}$$

The torque expression for the proposed DCM is exactly same with the non-salient permanent magnet

synchronous machines, which is different with most of the double salient machines. Essentially, this DCM has no salient effect according to the doubly complementary characteristic since the phase inductance keeps as a constant regardless of the rotor position.

3.3.4 Advantages of Doubly Complementary Characteristic

The major advantage of this machine is the high utilization of PMs contributed by the doubly complementary characteristic. To verify this idea, the other machine with same structure but no doubly complementary characteristic is given for comparison. Defining the angle between the central line of outer and inner rotor teeth is screw angle, so for the proposed DCM, the screw angle is π. The compared machine applies the structure as screw angle is 0 to remove the doubly complementary characteristic, which is marked as non-DCM. Fig. 3. 19 shows the simulation results of the back-EMF waveforms and the corresponding FFT analysis for DCM and non-DCM. It is seen that the back-EMF waveform for DCM is much better than that for non-DCM, with amplitude almost tripled and harmonics largely reduced.

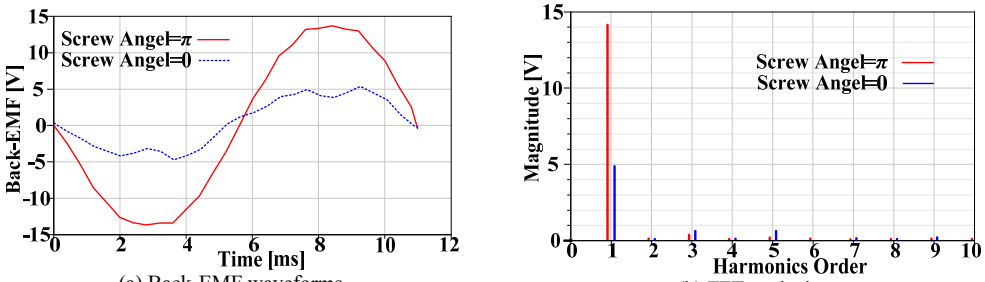

(a) Back-EMF waveforms. (b) FFT analysis.

Fig. 3. 19. Simulation results of back-EMF wavefroms of DCM and non-DCM.

The other advantage for the proposed DCM is small torque ripple since the salient effect is totally eliminated by the doubly complementary characteristic. Fig. 3. 20 presents the comparison results of output torque for DCM and non-DCM. It is shown that the peak-peak torque is 0.17 Nm for DCM while 0.42 Nm for non-DCM. By the way, the output torque for DCM is also more than double of the non-DCM because of the doubly complementary structure,

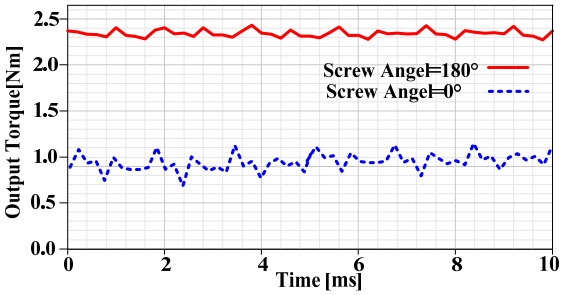

Fig. 3. 20. Simulation result of output torque for DCM and non-DCM.

3.4 Performances of the proposed DCM

3.4.1 Design Parameters and Prototype Pictures

A 12-11 DCM prototype is built to verify the feasibility of this design method and the experimental

results are presented. Table 3. 1 gives the basic design parameters of the prototype and Fig. 3. 21 presents some pictures of the stator, rotor and test bed.

Table 3. 1 Design Parameters of the Proposed Machine

Items	Value	Items	Value
Rated Speed	500 rpm	Single Air Gap	0.5 mm
Rated Current (Amplitude)	6A	PM Thickness	3.2mm
Rotor Pole Numbers	11	PM Width	5.65mm
Out Diameter	126 mm	Turns per Coil	35
Axial Length	76 mm	Conductor Diameter	0.95mm

(a) Stator.

(b) Rotor.

(c) Appearance.

(d) Test bed.

Fig. 3. 21. The prototype and test bed.

3.4.2 Back-EMF

Fig. 3. 22 gives the simulation and experiment results of the back-EMF waveforms. To explain the complementary characteristics, the waveforms for each group and final three phases are given. Fig. 3. 22 (a) and Fig. 3. 22 (b) present the waveforms in each group respectively. It is seen that there are some harmonics in each group, but these harmonics are cancelled by connecting the windings in series, as shown in Fig. 3. 22(c). Finally, the three-phase back-EMF is good sinusoidal waveform with few harmonic contents, as shown in Fig. 3. 22(d).

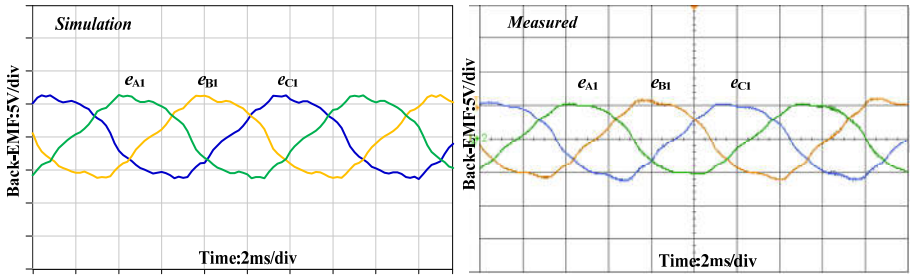

(a) For A_1, B_1 and C_1.

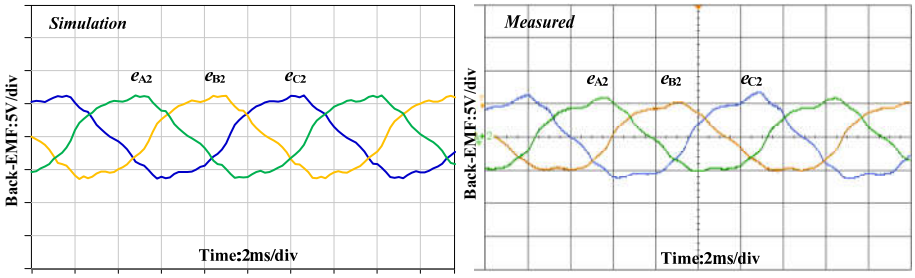

(b) For A_2, B_2 and C_2.

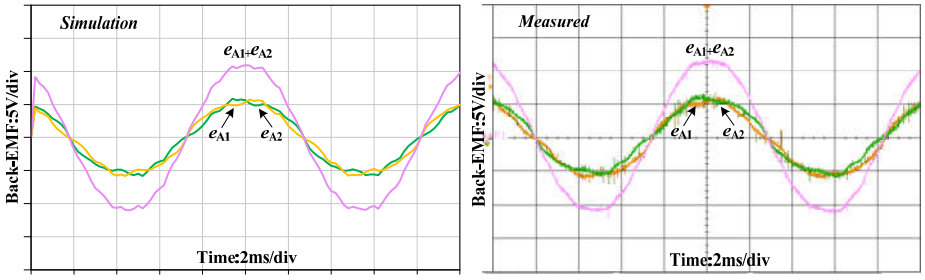

(c) For A_1, A_2 and A.

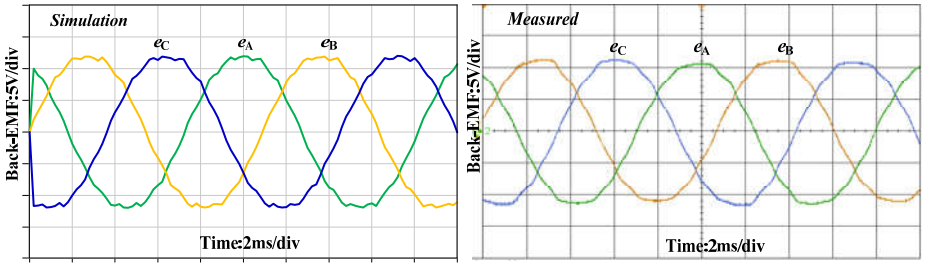

(d) For A, B, C.

Fig. 3. 22. Simulation and measured results of back-EMFs.

3.4.3 Torque Performance

To test the torque generating capability, the machine is driven by SVPWM. The relevant phase current and voltage are shown in Fig. 3. 23 when the machine operates under rated condition, with 6 A amplitude current and 500 rpm speed.

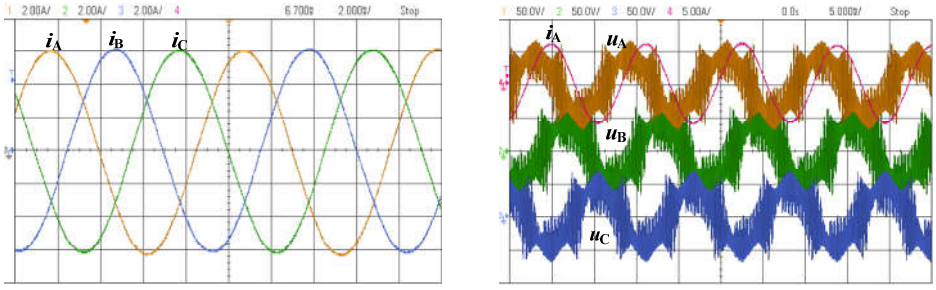

(a) Three-phase current. (b) Three-phase voltage and current for phase A.

Fig. 3. 23. Measured phase current and voltage.

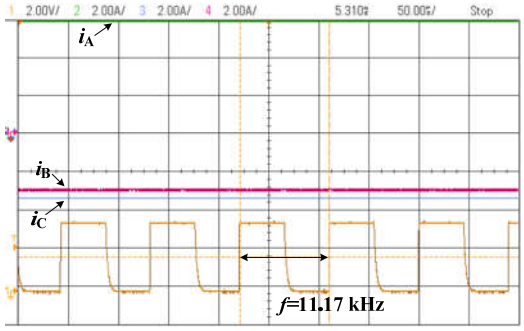

Fig. 3. 24. Measuring output torque under rated current.

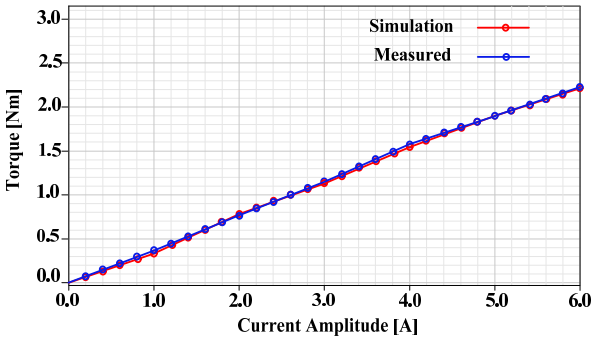

Fig. 3. 25. Measured torque generating capability.

Fig. 3. 24 shows the process of measuring the output torque. The output form of the torque sensor used is frequency, and the relationships between output frequency f and measured torque t_e is t_e=2(f-10). Under rated current, the measured torque is 2.34 Nm. Using this way, the torque generating capability of the proposed DCM is shown in Fig. 3. 25. Considering the heat dissipation condition, the experiments stops at unsaturated condition, with about 6 A/(mm)^2 in the copper core. The experiments results agree well with the finite element analysis.

3.4.4 Power Factor and Efficiency

The power factor and efficiency of the proposed DCM are also tested for evaluations. Fig. 3. 26 shows the phase relationship of the current and voltage for phase A. It is calculated the power factor is about 0.6. Because the used PM amount is limited, considering heavy armature reaction, this relatively low power factor is understandable. Fig. 3. 27 presents the tested efficiency, and it is shown that in the whole torque range, the efficiency is more than 80%. Noticeably, the efficiency is descending with the current increasing

because the iron loss is relatively low for this stator-PM low speed machines.

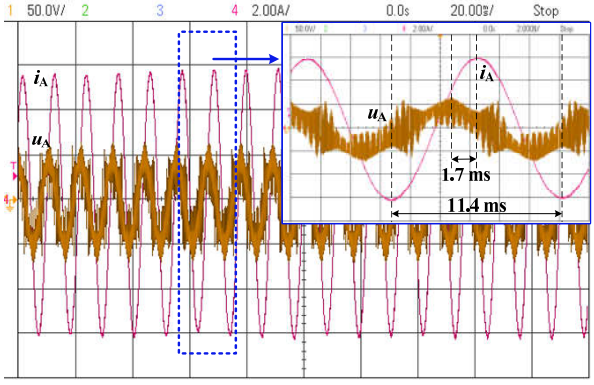

Fig. 3. 26. Measured power factor.

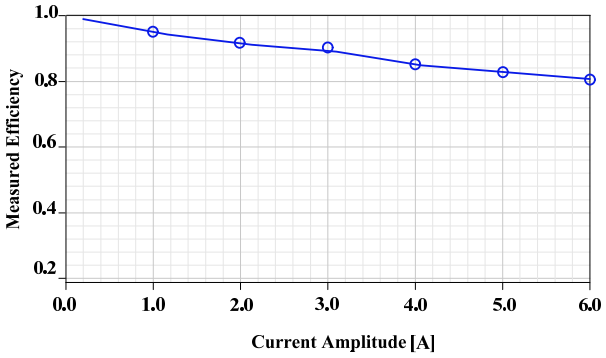

Fig. 3. 27. Measured efficiency under rated speed.

3.5 Extend the Complementary Magnetic Path into Axial flux machines

The main idea of complementary machine is to construct the complementary magnetic path to avoid short-circuit or open-circuit path. The complementary magnetic path can improve the PM utilization and reduce cogging torque for stator-PM machines. This concept could also be applied into other machines to improve the performances. A novel axial flux machines applied for direct drive applications is proposed in this part to demonstrate the design based on this concept.

The key is to employ a bilateral complementary rotors and alternative permanent magnets (PMs) with opposite magnetizing directions in the stator yoke to construct the doubly complementary structure. Therefore, the excitation flux could switch smoothly without been shorted or opened. This special design makes this machine obtain small cogging torque and high PM utilization, since the excitation flux is fully used in this way. This structure also makes this machine have the following characteristics, such as high wingding utilization factor and insignificant mutual-inductance, and the latter helps to improve the fault-tolerant capability of this machine. The topology and operation principle of the proposed machine are introduced, the major characteristics are analyzed and the electromagnetic performances are evaluated.

3.5.1 Topology and Operation Principle

The topology of this doubly complementary axial flux machine (DCDM) is shown in Fig. 3. 28. The stator has 24 slots with PMs installed in the yoke. The PMs are magnetized along circumferential direction

and the adjacent ones are with the opposite directions. The rotor applies bilateral complementary structure, which means there are double rotors, and they are staggered 180 mechanical degrees. Each rotor has the 11 salient teeth to vary the reluctance along the air-gap. The windings are wound on the stator teeth with the concentrated way, as shown in Fig. 3. 28. (b).

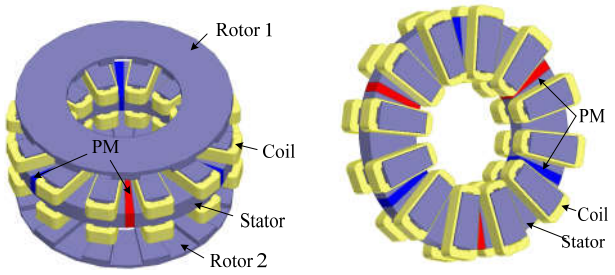

(a) Overview. (b) Stationary components.

Fig. 3. 28. Topology of DCDM.

The operation principle of this machine is shown in Fig. 3. 29. When the rotor moves to 0 electrical degree, the excitation flux created by PMs goes through Coil 3, Rotor 2 and Coil 4 to form a complete magnetic circuit, because the reluctance along this way is small. Ideally, there should be no exciting flux in Coil 1 and Coil 2. Next, when the rotor moves to 90 ° electrical degrees, the PM flux goes through the double rotors four coils. Next step, when the rotor moves to 180 ° electrical degrees, the PM flux goes through Coil 1, Rotor 1 and Coil 2, opposite to the situation Fig. 3. 29 (a). Lastly, when the rotor moves to 270° electrical degrees, the flux goes through both sides again. During this cycle, the flux in Coil 3 and Coil 4 changes from maximum to zero and then back to maximum, while the flux in Coil 1 and Coil 2 experiences from zero to negative maximum and back to zero.

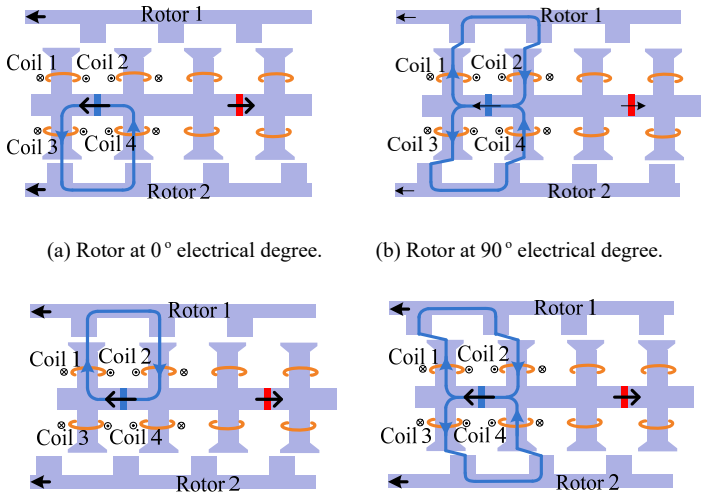

(a) Rotor at 0 ° electrical degree. (b) Rotor at 90 ° electrical degree.

(c) Rotor at 180 ° electrical degree. (d) Rotor at 270 ° electrical degree.

Fig. 3. 29. Operation principle diagram of the DCDM.

There are two distinguished characteristics for this proposed machine. Firstly, the PM flux is switched smoothly from one coil to another in the whole period, without been shorted or opened. Therefore, the PM utilization factor could be high. Secondly, the armature flux is parallel with the PM flux. Specifically, when the rotor moves to the position in Fig. 3. 29 (b) and Fig. 3. 29 (d), the drive current should get peak

since the open-circuit back-EMF gets its maximum. At these positions, the armature flux goes through the stator and rotor teeth to form a circuit, instead of through the PMs. This characteristic can increase the armature reaction to expand the flux weakening capability and avoid the risk of PMs being demagnetized.

3.5.2 Characteristics of Proposed DCDM

1) Doubly Complementary Characteristic

As the most important feature of this machine is the doubly complementary structure, to reveal this feature, the winding for phase A is taken for example. Eight coils belonging to winding A is divided into four windings, namely W_{A11}, $W_{A12,}$ W_{A21} and W_{A22}, as shown in Fig. 3. 30. W_{A11} and W_{A21} are in upper layer while W_{A12} and W_{A22} are in lower layer. W_{A11} and W_{A12} are wound on the teeth besides PM with clockwise magnetization direction while W_{A21} and W_{A22} are wound on the teeth besides the one with opposite magnetization direction. Doubly complementary feature has twofold meaning. 1) the exciting flux in the windings belonging to different layers is complementary, such as, W_{A11} and $W_{A12,}$ W_{A21} and W_{A22}, 2) the exciting flux in the windings besides PMs with opposite magnetization is complementary, for example W_{A11} and $W_{A21,}$ W_{A12} and W_{A22}.

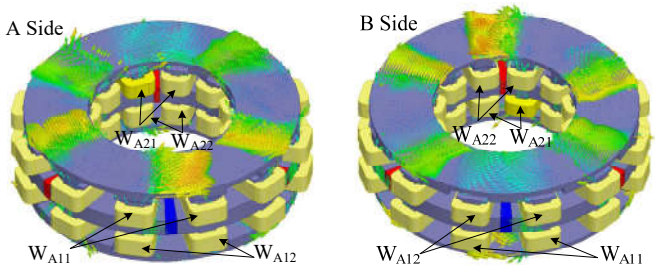

Fig. 3. 30. Open-circuit flux distribution of DCDM. (a) Top side. (b) Bottom side.

Fig. 3. 30 presents the simulation result of open-circuit flux distribution for this machine to demonstrate the doubly complementary characteristic. Fig. 3. 30 (a) and Fig. 3. 30 (b) gives the flux distribution for top side and bottom side respectively. Comparing these two pictures, it is found that the exciting flux in W_{A11} (written as ψ_{A11}) and in W_{A12} (written as ψ_{A12}) is complementary, as ψ_{A11} gets maximum, and ψ_{A12} gets minimum. This is the same for the excitation flux in W_{A21} (written as ψ_{A21}) and in W_{A12} (written as ψ_{A12}). This is caused by the complementary rotor, as the reluctance along the air-gap under these windings is complementary. This characteristic can significantly improve the PM utilization factor, as the PM flux could switch smoothly between the upper layer and lower layer without been shorted or opened. The second complementary characteristic could be verified if the windings besides different PMs are focused. It is demonstrated in Fig. 3. 30 (a) that ψ_{A11} and ψ_{A21} is complementary, and in Fig. 3. 30 (b), ψ_{A12} and ψ_{A22} is complementary. This characteristic could alleviate the even order harmonics in the final phase flux to ensure the Back-EMF has a good sinusoidal waveform. To reveal this doubly complementary characteristic, the excitation flux in these four windings is expressed in (3-20).

$$\begin{cases} \psi_{A11} = \psi_{DCA11} + \sum_{n=1,2,3...}^{+\infty} \psi_{ACA11n} \cos(n\theta_e) \\ \psi_{A12} = -\psi_{DCA11} - \sum_{n=1,2,3...}^{+\infty} \psi_{ACA12n} \cos(n\theta_e + n\pi) \\ \psi_{A21} = -\psi_{DCA21} - \sum_{n=1,2,3...}^{+\infty} \psi_{ACA21n} \cos(n\theta_e + n\pi) \\ \psi_{A22} = \psi_{DCA22} + \sum_{n=1,2,3...}^{+\infty} \psi_{ACA22n} \cos(n\theta_e) \end{cases} \quad (3\text{-}20)$$

where ψ_{DCAij} is the DC component of the ψ_{Aij} and ψ_{ACAijn} is the amplitude of n^{th} harmonics for the ψ_{Aij}. To verify the doubly complementary, the simulation results for these four windings are presented in Fig. 3. 31. It is shown that the simulation results agree with (3-20) well, as ψ_{A11} is complementary with ψ_{A12} and ψ_{A21}, ψ_{A22} is complementary with ψ_{A12} and ψ_{A21}. The leakage flux is small, only taking 11% of the AC flux amplitude, which means, it can effectively improve the PM utilization through constructing the complementary structure.

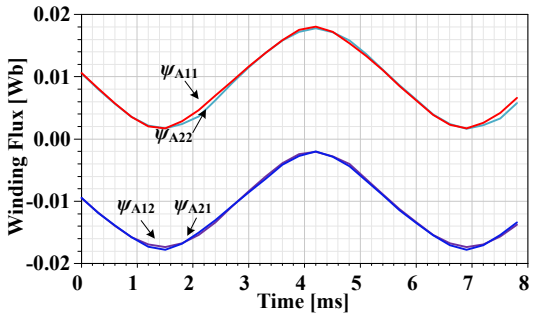

Fig. 3. 31. Simulation results of winding flux for ψ_{A11}, ψ_{A12}, ψ_{A21} and ψ_{A22}.

The final three phase flux is shown in Fig. 3. 32. It is demonstrated that the even order harmonics including the DC complements are alleviated, as the phase flux has a good sinusoidal waveforms.

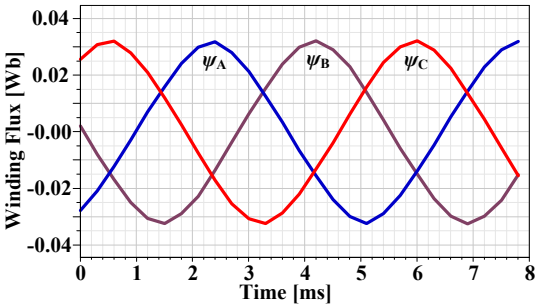

Fig. 3. 32. Simulation results of three phase flux.

2) High Winding Utilization Factor

The other characteristic of this machine is its high winding utilization factor. Because of the special design of the doubly complementary structure, the AC component of the excitation flux in four windings belonging to same phase has the same phase position, as shown in Fig. 3. 31. The rotor teeth number is also selected specifically as 11 to construct the three phase windings.

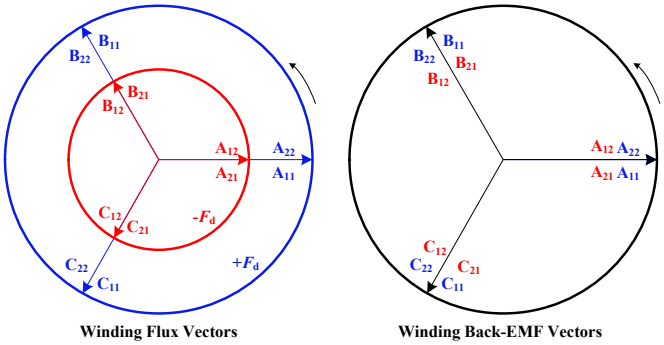

Fig. 3. 33. Winding flux vectors and winding Back-EMF vectors.

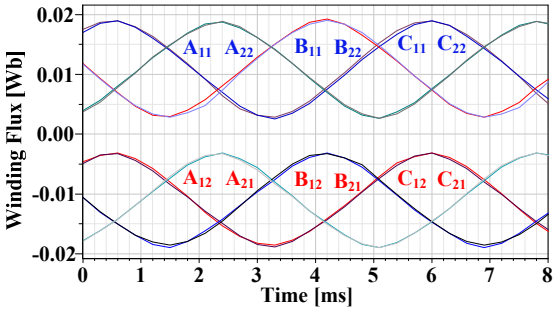

Fig. 3. 34. Simulation results of the winding flux waveforms.

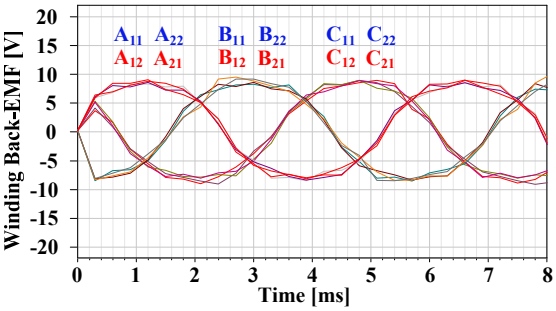

Fig. 3. 35. Simulation results of the winding Back-EMF waveforms.

Fig. 3. 33 presents the winding flux vectors and winding Back-EMF vectors to demonstrate the high winding utilization factor. Noticeably, the flux vector has DC component, so these flux vectors are divided into two groups, namely the ones with negative DC component $-F_d$ and with positive DC component $+F_d$ respectively. The former ones are drown in the inner circle while the latter ones are drown in the outer circle. However, the DC component is eliminated when it comes to the Back-EMF vectors. The phase position of the Back-EMF in four windings belonging to same phase is the same, so actually the winding utilization factor is 1.

Fig. 3. 34 and Fig. 3. 35 give the simulation results of the winding flux and Back-EMF waveforms respectively to verify the analysis above. It is shown the simulation results agree well with Fig. 3. 33 if the high order harmonics are neglected, and the winding utilization factor is 1.

3) Small Cogging Torque

Small cogging torque is another advantage of this DCDM. This is contributed from the doubly

complementary structure. Since the excitation flux could switch smoothly between the bilateral rotors, the rotor will not prefer some special positions. The cogging torque for this machine is relatively small comparing to the other stator-PM machines with double salient structure. Fig. 3. 36 presents the simulation result of the cogging torque and it is shown that the cogging torque only takes about 5.7% of the rated torque.

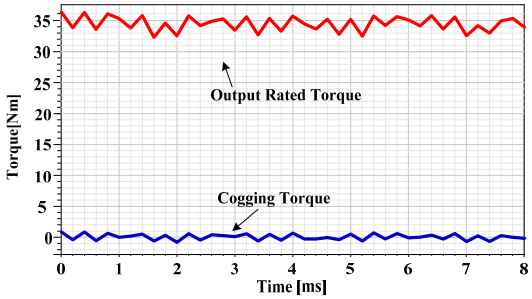

Fig. 3. 36. Simulation results of the cogging torque.

3) Without Mutual Inductance

Another interesting characteristic of this machine is that there is no mutual inductance among different phases. In other words, this machine is combined of three independent single phase machines. Fig. 3. 37 presents the simulation results of the inductance of Phase A, including the self-inductance and the mutual-inductance among Phase B and Phase C.

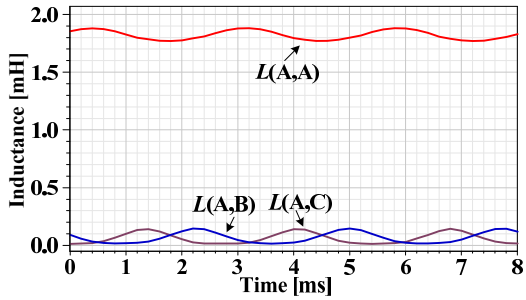

Fig. 3. 37. Simulation results of the inductance of phase A.

It is seen the self-inductance varies very small due to the complementary characteristic and the mutual inductance of phase AB and AC is relatively small comparing the self-inductance and can be neglected.

3.5.3 Electromagnetic Performance of DCDM

The characteristics of the DCDM is introduced above and in this section, the electromagnetic performance of this machine will be presented. Table 3. 2 lists the key design parameters of this DCDM.

Table 3. 2 Key Design Parameters of This DCDM

Parameters	Quantity
Rated Speed	500 rpm
Rated Torque	35 Nm
Out Diameter	300 mm
Inner Diameter	160 mm
Axial Length	84 mm
Rated Phase Current	100 A (Amplitude)
Phase Resistance	0.015 Ω
Phase Inductance	1.85 mH
Conductor Number	10
Slot Area	962.5 $(mm)^2$
Coil Space Factor	0.5
Current Density in Copper	4.5 $A/(mm)^2$
Conductor Section Area	24 $(mm)^2$

Fig. 3. 38 gives the simulation results of the final three-phase Back-EMF. It is shown that the waveform is symmetric without even order harmonics, which agrees with the theoretical analysis. Although there are some high order harmonics, the waveforms are still acceptable.

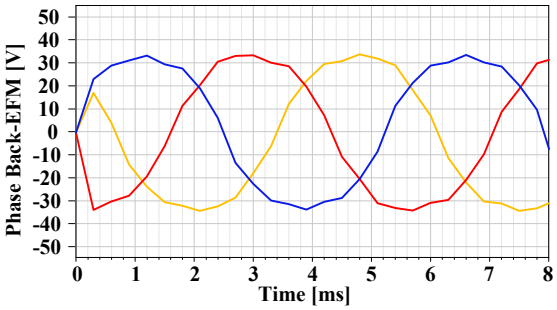

Fig. 3. 38. Simulation results of three phase Back-EMF.

Fig. 3. 39 presents the simulation results of the output torque. The torque can reach 35 Nm when the AC amplitude is 100 A. The saturation of the steel is slightly at rated torque, so the torque is not proportional to the current. Fig. 3. 40 gives the efficiency when the machine operating in rated speed with different current. It is shown that the highest efficiency could reach 93% and in the whole current range the efficiency is not less than 90%.

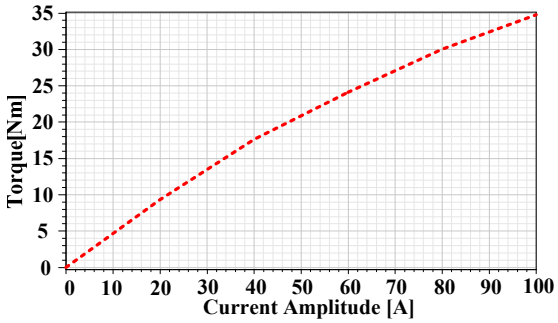

Fig. 3. 39. Simulation results of output torque.

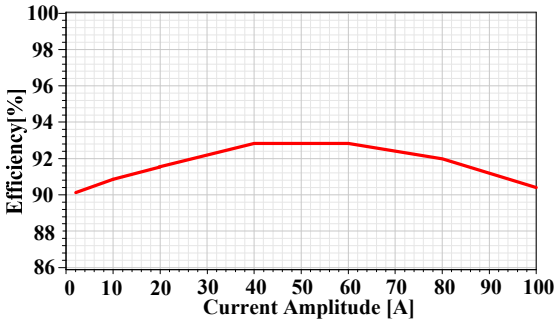

Fig. 3. 40. Simulation results of the efficiency at rated speed.

A novel axial flux machine with doubly complementary structure is introduced in this part. Its operation principle, characteristics and electromagnetic performance are introduced. Because of the doubly complementary structure, this machine obtains the advantages of small cogging torque, high PM utilization factor. The torque density and efficiency is not very high since the PM consumption is small, which is foreseeable. Nevertheless, this machine could be a strong candidate for direct-drive applications since it obtains the competitive performance with low cost.

3.6 Conclusion

From the perspective of improving PM utilization factor, a new type of doubly complementary machines are proposed, which apply the doubly complementary rotors to avoid PM flux been shorted or opened. The principle and characteristics of these machines are introduced, followed by the design methodology. It is revealed, these machine have good sinusoidal back-EMF and constant inductance, so they have the same torque form with the non-salient PMSM. A prototype is built for evaluation, and it is verified that this machine has high PM utilization and small cogging torque. Meanwhile, the torque performance is acceptable and the efficiency is more than 80% at all torque range.

The major advantage for this machine is high torque/PM because of its complementary characteristic. It is a strong candidate for low cost machine for its acceptable torque density, efficiency and small torque ripple. On the other hand, the limited space for PM may restrict the torque density and lower the power factor, which needs further study. The idea of constructing doubly complementary structure to improve electrical performance of stator-PM machines is novel, which provides a new perspective to study stator-PM machines.

A novel axial flux machine with doubly complementary structure is also proposed in this chapter. Its

operation principle, characteristics and electromagnetic performance are introduced. Because of the doubly complementary structure, this machine obtains the advantages of small cogging torque, high PM utilization factor. The torque density and efficiency is not very high since the PM consumption is small, which is foreseeable. Nevertheless, this machine could be a strong candidate for direct-drive applications since it obtains the competitive performance with low cost.

Chapter 4 Design and Analysis of Stator-PM Vernier Machines

In this chapter, one novel kind of machines is proposed for direct drive applications. These machines apply the principle of Vernier machine but obtain the paralleled magnetic path. Comparing with FSCW machines, the relationship of slots and rotor pole-pairs could be decoupled. So it is more suitable for low speed application. While comparing with other Vernier machines, the proposed machines have the following advantages. 1) These machines are mechanical reliable and endurable because of the simple structure. 2) The armature magnetic field will not pass through PMs, it is possible to get stronger armature field under same current to increase the torque. 3) The heat dissipation condition is better since the PMs are installed on stator. This chapter is organized by followings, Section 4.2 introduces the principle of this kind of machines, Section 4.3 compares the combinations of winding and rotor poles, Section 4.4 gives the simulation and experimental analysis and Section 4.5 presents the conclusions.

4.1 Principle of Slot-PM Vernier Machines

In this part, the paralleled magnetic path of slot-PM Vernier machine is introduced firstly. Then the operation principle is presented by analytical method.

4.1.1 Paralleled Magnetic Path

Fig. 4. 1 (a) shows the basic topology of the proposed slot-PM Vernier machines. It is seen that these machines have PMs with consequent poles installed in the slots and apply the non-PM rotor with salient teeth. To demonstrate the difference of paralleled magnetic path and serial magnetic path, the topology of traditional FSCW machines is presented in Fig. 4. 1(b).

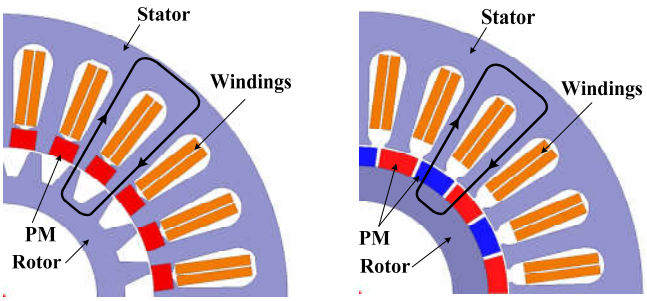

(a) slot-PM Vernier machine. (b) FSCW machine.

Fig. 4. 1. Basic topologies for slot-PM Vernier machine and FSCW machine.

It is shown that for slot-PM Vernier machine, the armature magnetic field goes through stator, air-gap and rotor to form the loop, without passing through the PMs. So the exciting magnetic path and armature magnetic path are paralleled. While for FSCW machine, the armature magnetic field goes through PMs. So FSCW machines have the serial magnetic path. For the proposed slot-PM Vernier machines, since the armature magnetic field will not pass through the high magnetoresistance PMs, the armature magnetic field could be much stronger than FSCW machines, which helps to improve the torque.

4.1.2 Operation Principle

The principle of the proposed slot-PM machines is different from the traditional synchronous PM machines. The armature field does not interact with the fundamental harmonic of the exciting field, but with the modulated harmonics. So for the analysis here, the exciting magnetic field is focused. By figuring out pole-pairs and velocity of the exciting magnetic field, the winding and drive current could be configured correspondingly.

Fig. 4. 2 gives the simplified model of the slot-PM Vernier machine. For the sake of analysis, assuming the slots have infinite depth and have equal width with the teeth. The Cartesian coordinate system is used, where *y-axis* is selected in the central line of one stator tooth. Assuming the rotor moves along *x-axis* with angular velocity ω_m and the central line of one rotor tooth is aligned with *y-axis* at t=0 moment.

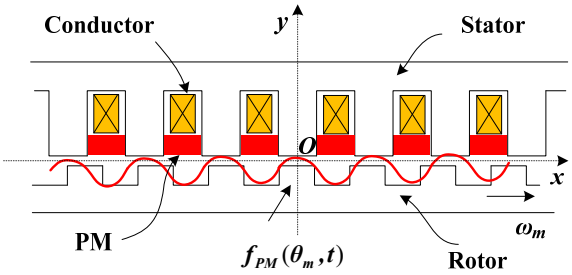

Fig. 4. 2. Simplified model of the slot-PM Vernier machine.

The air-gap permeability λ at θ_m position and t moment could be expressed as:

$$\lambda(\theta_m,t)=(\Lambda_s+\sum_{n_s=1}^{\infty}\Lambda_{sn_s}\cos n_s Z_s\theta_m)\bullet[\Lambda_r+\sum_{n_r=1}^{\infty}\Lambda_{rn_r}\cos n_r Z_r(\theta_m+\omega_m t)] \tag{4- 1}$$

Where, for stator teeth permeability, Λ_s is the average value, n_s is the harmonic order and Λ_{snS} is the magnitude of n_s order harmonic. While for rotor teeth permeability, Λ_r is the average value, n_r is the harmonic order and Λ_{rnr} is the magnitude of n_r order harmonic. Besides, Z_s and Z_r is the stator and rotor teeth number respectively.

Since PM pieces equal to the stator teeth and PMs are stationary, the magnetic motive force (MMF) of the exciting source could be expressed as:

$$f(\theta_m,t)=\sum_{n_f=1}^{\infty}F_{n_f}\cos n_f Z_s\theta_m \tag{4- 2}$$

Where F_{nf} is the magnitude of n_f order harmonic of the MMF.

The magnetic field intensity produced by PM could be expressed as:

$$\begin{aligned}
&B(\theta_m,t)=\lambda(\theta_m,t)\bullet f(\theta_m,t)=\\
&\Lambda_r\Lambda_s\sum_{n_f=1}^{\infty}F_{n_f}\cos n_f Z_s\theta_m+\\
&\Lambda_r\sum_{n_f=1}^{\infty}F_{n_f}\cos n_f Z_s\theta_m\bullet\sum_{n_s=1}^{\infty}\Lambda_{sn_s}\cos n_s Z_s\theta_m+\\
&\Lambda_s\sum_{n_f=1}^{\infty}F_{n_f}\cos n_f Z_s\theta_m\bullet\sum_{n_r=1}^{\infty}\Lambda_{rn_r}\cos n_r Z_r(\theta_m+\omega_m t)+\\
&\sum_{n_f=1}^{\infty}F_{n_f}\cos n_f Z_s\theta_m\bullet\sum_{n_s=1}^{\infty}\Lambda_{sn_s}\cos n_s Z_s\theta_m\bullet\sum_{n_r=1}^{\infty}\Lambda_{rn_r}\cos n_r Z_r(\theta_m+\omega_m t)
\end{aligned} \tag{4- 3}$$

It is seen that there are four items in the expression. The first one is produced by MMF and the average

permeability. Using B_1 to represent the field produced by n_f order harmonic of MMF, B_1 could be expressed as:

$$B_1=\Lambda_r\Lambda_s F_{n_f}\cos n_f Z_s\theta_m \tag{4- 4}$$

So B_1 has the pole-pair of n_fZ_s and its rotational speed is zero.

The second item is produced by MMF and the permeability variation of stator teeth. Using B_2 to represent field produced by n_f order harmonic of MMF and n_s order harmonic of permeability for stator slot, B_2 could be expressed as:

$$B_2=\Lambda_r\Lambda_{sn_s}F_{n_f}\cos n_f Z_s\theta_m\bullet\cos n_s Z_s\theta_m=\frac{\Lambda_r\Lambda_{sn_s}F_{n_f}}{2}\left[\cos(n_f+n_s)Z_s\theta_m+\cos(n_f-n_s)Z_s\theta_m\right] \tag{4- 5}$$

It is seen that B_2 has the pole-pairs of $(n_s\pm n_f)Z_s$ and the corresponding rotational speed is zero.

The third item is produced by MMF and the permeability variation of the rotor teeth. Using B_3 to represent the field produced by n_f order harmonic of MMF and n_r order harmonic of permeability for rotor teeth, B_3 could be expressed as:

$$\begin{aligned}B_3&=F_{n_f}\Lambda_s\Lambda_{rn_r}\cos n_f Z_s\theta_m\cos n_r Z_r(\theta_m+\omega_m t)\\&=\frac{F_{n_f}\Lambda_s\Lambda_{rn_r}}{2}\cos\left[(n_fZ_s+n_rZ_r)\theta_m+n_rZ_r\omega_m t\right]+\frac{F_{n_f}\Lambda_s\Lambda_{rn_r}}{2}\cos\left[(n_fZ_s-n_rZ_r)\theta_m-n_rZ_r\omega_m t\right]\end{aligned} \tag{4- 6}$$

It is seen that B3 has the pole-pairs of $n_fZ_s\pm n_rZ_r$ and the corresponding rotational speed is $\frac{n_rZ_r}{n_rZ_r\pm n_fZ_s}\omega_m$.

The fourth item is produced by MMF and the permeability variation of both stator and rotor teeth. Using B_4 to represent the field produced by n_f order harmonic of MMF, n_s order harmonic of permeability for stator teeth and n_r order harmonic of permeability for rotor teeth, B_4 could be expressed as:

$$\begin{aligned}B_4&=F_{n_f}\Lambda_{rn_r}\Lambda_{sn_s}\cos n_rZ_r(\theta_m+\omega_m t)\bullet\cos n_fZ_s\theta_m\bullet\cos n_sZ_s\theta_m\\&=\frac{F_{n_f}\Lambda_{rn_r}\Lambda_{sn_s}}{4}\cos\left[(n_rZ_r+n_fZ_s+n_sZ_s)\theta_m+n_rZ_r\omega_m t\right]+\\&\frac{F_{n_f}\Lambda_{rn_r}\Lambda_{sn_s}}{4}\cos\left[(n_rZ_r+n_fZ_s-n_sZ_s)\theta_m+n_rZ_r\omega_m t)\right]+\\&\frac{F_{n_f}\Lambda_{rn_r}\Lambda_{sn_s}}{4}\cos\left[(n_rZ_r-n_fZ_s+n_sZ_s)\theta_m+n_rZ_r\omega_m t)\right]+\\&\frac{F_{n_f}\Lambda_{rn_r}\Lambda_{sn_s}}{4}\cos\left[(n_rZ_r-n_fZ_s-n_sZ_s)\theta_m+n_rZ_r\omega_m t\right]\end{aligned} \tag{4- 7}$$

It is seen that B4 has the pole-pairs of $n_rZ_r+n_fZ_s\pm n_sZ_s$ and $n_rZ_r-n_fZ_s\pm n_sZ_s$, the corresponding rotational speed is $\frac{n_rZ_r}{n_rZ_r+n_fZ_s\pm n_sZ_s}\omega_m$ and $\frac{n_rZ_r}{n_rZ_r-n_fZ_s\pm n_sZ_s}\omega_m$ respectively.

According to the analysis above, the component of exciting magnetic field could be summarized in Table 4. 1.

Table 4. 1 Components of Exciting Magnetic Field

Generated by	Pole-Pair	Angular Velocity
Average permeance	$n_f Z_s$	0
Stator teeth	$(n_f \pm n_s)Z_s$	0
Rotor teeth	$n_f Z_s \pm n_r Z_r$	$\frac{n_r Z_r}{n_r Z_r \pm n_f Z_s}\omega_m$
Stator teeth and rotor teeth	$n_r Z_r + n_f Z_s \pm n_s Z_s$	$\frac{n_r Z_r}{n_r Z_r + n_f Z_s \pm n_s Z_s}\omega_m$
	$n_r Z_r - n_f Z_s \pm n_s Z_s$	$\frac{n_r Z_r}{n_r Z_r - n_f Z_s \pm n_s Z_s}\omega_m$

To generate constant torque, the armature field should have the same pole-pairs and same rotational speed with the exciting field. So the combination of winding pole-pairs, stator teeth and rotor teeth could be selected from the second row in Table I. It is found that not all the combinations can work. Firstly, the combinations listed in first and second rows have zero speed, so they could not work. Secondly, some combinations do not exist due to physical constrain as the poles of windings are greater than slots. Additionally, the combination for traditional synchronous machines-winding (poles equal with rotor poles) will not be discussed here.

Therefore, the combinations of stator teeth, rotor teeth and winding poles for slot-PM Vernier machines could be given by:

$$P_W = \begin{cases} \left| n_f Z_s - n_r Z_r \right|, n_f, n_r = 1,2,3... \\ \left| n_r Z_r - n_f Z_s - n_s Z_s \right|, n_r, n_s, n_f = 1,2,3... \end{cases} \quad (4\text{- }8)$$

All the machines agree with (4-8) could generate constant torque. So there are many selections in design this kind of machines. It is necessary to figure out which combinations could have better torque performance.

4.2 Design Stator-PM Vernier Machines with different Rotor and Winding Poles

This section compares the torque for machines with different winding and rotor poles. The machines with 24 slots are selected for analysis. Firstly, the torque factor is developed to evaluate the torque performance of different machines. Secondly, finite element simulations are conducted for verification.

According to (4-8), there are many combinations of winding and rotor poles for 24-slot machines. To limit the number of analyzed machines, the machines working with high harmonics are not considered, which means n_f, n_s, n_r equals 1 in (4-8). Besides, to eliminate the unbalanced magnetic force, the rotor teeth N_r are selected as even number. So the 24-slot machines with different combinations could be listed in Table 4. 2.

Table 4. 2 24-Slot Machines With Different Combinations

Winding Pole-Pair Number	Rotor Teeth Number
2	22, 26, 46, 50
4	20, 28, 44, 52
8	16, 32, 40, 56
10	14, 34, 38, 58
14	10, 38, 34, 62

4.3 Torque Factors for Vernier Machines

To evaluate the torque performance of the machines listed in Table II, the torque factor is defined as torque/current and its expression is developed by the following procedures. Firstly, the exciting field in terms of pole-pairs, rotational speed and intensity is figured out. Secondly, the back-EMF is calculated by synthetically considering the winding factor. Thirdly, the torque and torque factor is calculated.

Table 4. 3 Total Exciting Fields

i	$P_B^{n_r,n_s,n_f,i}$	$\omega_B^{n_r,n_s,n_f,i}$	$M_B^{n_r,n_s,n_f,i}$
1	$n_f Z_s$	0	$\frac{M_B}{n_f}$
2	$(n_f+n_r)Z_s$	0	$\frac{2M_B}{\pi Z_s n_f n_s}$
3	$(n_f-n_r)Z_s$	0	$\frac{2M_B}{\pi Z_s n_f n_s}$
4	$n_f Z_s+n_r Z_r$	$\frac{n_r Z_r}{n_f Z_s+n_r Z_r}\omega_m$	$\frac{2M_B}{\pi Z_r n_r n_f}$
5	$n_f Z_s$-$n_r Z_r$	$\frac{-n_r Z_r}{n_f Z_s-n_r Z_r}\omega_m$	$\frac{2M_B}{\pi Z_r n_r n_f}$
6	$n_r Z_r+n_f Z_s+n_s Z_s$	$\frac{n_r Z_r}{n_r Z_r+n_f Z_s+n_s Z_s}\omega_m$	$\frac{M_B}{\pi Z_s Z_r n_r n_s n_f}$
7	$n_r Z_r+n_f Z_s-n_s Z_s$	$\frac{n_r Z_r}{n_r Z_r+n_f Z_s-n_s Z_s}\omega_m$	$\frac{M_B}{\pi Z_s Z_r n_r n_s n_f}$
8	$n_r Z_r-n_f Z_s+n_s Z_s$	$\frac{n_r Z_r}{n_r Z_r-n_f Z_s+n_s Z_s}\omega_m$	$\frac{M_B}{\pi Z_s Z_r n_r n_s n_f}$
9	$n_r Z_r-n_f Z_s-n_s Z_s$	$\frac{n_r Z_r}{n_r Z_r-n_f Z_s-n_s Z_s}\omega_m$	$\frac{M_B}{\pi Z_s Z_r n_r n_s n_f}$

Eq. (4-4) to Eq. (4-7) has given the pole-pairs, rotational speed and intensity of the exciting fields. Using MB to represent the field magnitude produced by fundamental MMF and average permeability, MB could be expressed as $\Lambda_r\Lambda_s F_1$. According to Fourier transform theory, the magnitude of the MMF harmonics and the permeability harmonics could be expressed as $F_{n_s}=\frac{F_1}{n_f}$, $\Lambda_{rn_r}=\frac{4}{\pi}\frac{\Lambda_r}{N_r n_r}$ and $\Lambda_{sn_s}=\frac{4}{\pi}\frac{\Lambda_s}{N_s n_s}$. Combing

with (4-7), magnitudes of each exciting field could be determined. Table 4. 3 gives the total exciting fields including pole-pairs, rotational speed and magnitude.

There are 9 components for the exciting fields. With *i* to represent the sequence number of these components, $P_B^{n_r,n_s,n_f,i}$, $\omega_B^{n_r,n_s,n_f,i}$ and $M_B^{n_r,n_s,n_f,i}$ could represent the pole-pairs, rotational speed and magnitude of the *No.i* field.

Assuming the air-gap radius is r_g and the axial length is *l*, the back-EMF in single conductor produced by *No.i* exciting field could be expressed as:

$$e_{n_r,n_s,n_f,i}(t) = lr_g M_B^{n_r,n_s,n_f,i} \omega_B^{n_r,n_s,n_f,i} \sin(P_B^{n_r,n_s,n_f,i} \omega_B^{n_r,n_s,n_f,i} t) \tag{4- 9}$$

It is interesting to find $P_B^{n_r,n_s,n_f,i} \omega_B^{n_r,n_s,n_f,i} = \left| n_r Z_r \omega_m \right|$ from Table 4. 3. So the back-EMF frequency is independent from n_s and n_f. As long as n_r equals 1, the back-EMF caused by other harmonics has the fundamental frequency.

Combing with the winding factors for different components of exciting fields, the phase back-EMF produced by n_r order MMF, n_s and n_r order permeability could be expressed as:

$$e_{\varphi,n_r,n_s,n_f}(t) = N \sum_{i=1}^{9} k_W^{n_r,n_s,n_f,i} e_{n_r,n_s,n_f,i}(t) \tag{4- 10}$$

Where N is the number of conductors and $k_W^{n_r,n_s,n_f,i}$ is the winding factor for the field with $P_B^{n_r,n_s,n_f,i}$ pole-pairs. The winding factor can be calculated by,

$$k_W^{n_r,n_s,n_f,i} = k_y^{n_r,n_s,n_f,i} k_q^{n_r,n_s,n_f,i} \tag{4- 11}$$

where $k_y^{n_r,n_s,n_f,i}$ is the coil pitch factor and $k_q^{n_r,n_s,n_f,i}$ is the winding distribution factor. They can be calculated by (4-12) and (4-13) according to the winding theory.

$$k_y^{n_r,n_s,n_f,i} = \sin\left(\frac{y_1 P_W \pi}{Z_s} \frac{P_B^{n_r,n_s,n_f,i}}{P_W}\right) = \sin\left(\frac{y_1 P_B^{n_r,n_s,n_f,i} \pi}{Z_s}\right) \tag{4- 12}$$

$$k_q^{n_r,n_s,n_f,i} = \frac{\sin\frac{P_B^{n_r,n_s,n_f,i} q\alpha}{P_W 2}}{q \sin\frac{P_B^{n_r,n_s,n_f,i} \alpha}{P_W 2}} \tag{4- 13}$$

In Eq. (4-12), y_1 is the coil pitch. For 24-slot machines with winding pole-pairs of 2, 4, 8, 10 and 14, y_1 is 6, 3, 1, 1 and 1 respectively. In Eq. (4-13), α is the electrical phase difference of the adjacent conductors and *q* is the slots per pole and per phase, which can be calculated by,

$$q=\begin{cases}\dfrac{Z_s}{2mP_W}, \text{when } \dfrac{Z_s}{2mP_W} \text{ is integer} \\ d, \text{when } \dfrac{Z_s}{2mP_W}=\dfrac{d}{c},\ c,d \text{ is integer}\end{cases} \tag{4- 13}$$

For 24-slot machines with winding pole-pairs of 2, 4, 8, 10 and 14, q is 2, 1, 1, 2 and 2 respectively.

It has been mentioned that when n_r equals 1, the back-EMF caused other harmonics has the fundamental frequency, so it is necessary to set n_r=1 to calculate the effective back-EMF. To simplify the analysis, the order for n_s and n_f are taken up to 3. The final phase back-EMF could be expressed as:

$$e_\varphi = lr_g N \sum_{n_f=1}^{n_f=3}\sum_{n_s=1}^{n_s=3}\sum_{i=1}^{9} k_W^{1,n_s,n_f,i}\omega_B^{1,n_s,n_f,i}M_B^{1,n_s,n_f,i}\sin(Z_r\omega_m t) \tag{4- 15}$$

When AC current with amplitude of I_{ac} is injected for driven, the final electromagnetic torque could be expressed as,

$$T_e=\frac{e_a i_a+e_b i_b+e_c i_c}{\omega_m}=1.5NI_{ac}lr_g\sum_{n_f=1}^{n_f=3}\sum_{n_s=1}^{n_s=3}\sum_{i=1}^{9}k_W^{1,n_s,n_f,i}\omega_B^{1,n_s,n_f,i}M_B^{1,n_s,n_f,i} \tag{4- 16}$$

So the torque factor K_T could be obtained by,

$$K_T=\frac{T_e}{NI_{ac}}=1.5lr_g\sum_{n_f=1}^{n_f=3}\sum_{n_s=1}^{n_s=3}\sum_{i=1}^{9}k_W^{1,n_s,n_f,i}\omega_B^{1,n_s,n_f,i}M_B^{1,n_s,n_f,i} \tag{4- 17}$$

Based on Table 4. 3 and (4-17), the torque factors for 24-slot Vernier machines with different winding and rotor poles have been calculated and shown in Fig. 4. 3.

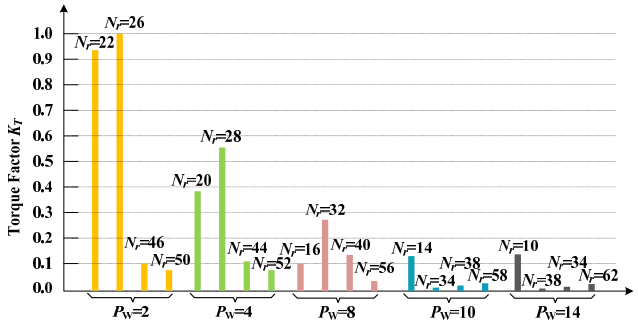

Fig. 4. 3.Torque factor for slot-PM Vernier machines with different winding and rotor poles.

It is shown that 24-2-26 machine has the highest torque value and the following is 24-2-22, 24-4-28, 24-4-20 and so on. It is easier for the machines with small winding pole number to obtain higher torque. This is because the small winding pole number helps to improve the rotational speed of the dominant exciting field component, which is the *No.5* component in Table 4. 3.

To verify the analysis of torque factor, the simulations have been conducted. According to Fig. 4. 3, the machines with winding pole-pairs of 2, 4 and 8 have better performance than others, so the simulations are conducted on these 8 machines. The torque waveforms are shown in Fig. 4. 4 and the average value are listed in Fig. 4. 5.

It is shown the simulation result agrees well with the theory analysis, the proposed torque factor is

effective to evaluate the torque performance of this kind of slot-PM Vernier machines.

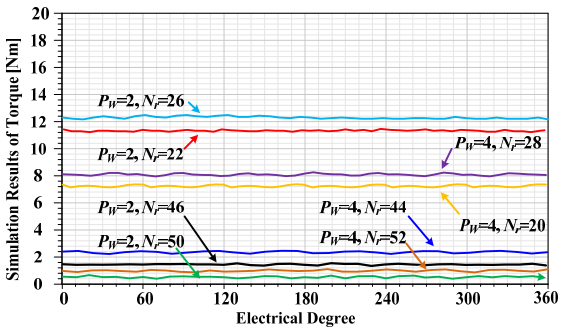

Fig. 4. 4. Simulation results of torque for slot-PM Vernier Machines with different combinations of winding and rotor poles.

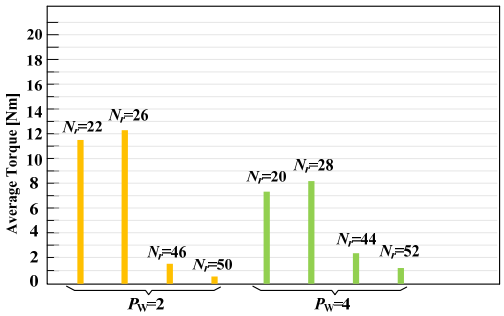

Fig. 4. 5. Average torque value for slot-PM Vernier Machines with different combinations of winding and rotor poles.

4.4 Performance of the Proposed Stator-PM Vernier Machine

To verify the paralleled magnetic path characteristic and the performance of the proposed slot-PM consequent pole Vernier machines, one prototype with 24 slots, 2 winding pole-pairs and 22 rotor teeth has been selected for case study. Simulation and experimental results are presented.

Fig. 4. 6 gives the model of the 24-2-22 machine, Table Table 4. 4 presents the mechanical dimensions and Table 4. 5 gives the operation condition. To obtain maximum torque, the parameters including PM_Embrace, PM_Thick, Angle1, Angle2 and H_Rotor have been optimized by using the toolbox in Maxwell software with the genetic algorithm.

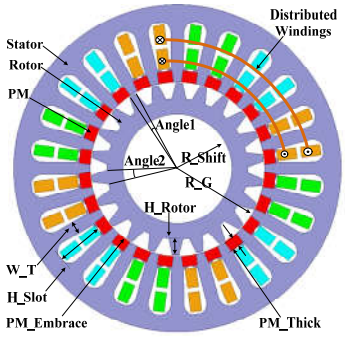

Fig. 4. 6. Simulation model of 24-2-22 slot-PM Vernier machine.

Table 4. 4 key Parameters of 24-2-22 Slot-PM Vernier Machine

Items	Value	Items	Value
Out Diameter	120 mm	H_Slot	18 mm
Axial Length	55 mm	PM_Embrace	0.63
Air Gap	0.5 mm	PM_Thick	4.1 mm
R_G	31.75 mm	Angle1	4.3 Degree
R_Shaft	20 mm	Angle2	13 Degree
W_T	4.6 mm	H_Rotor	6.7 mm

Table 4. 5 Key Design Parameters of 24-2-22 Slot-PM Vernier Machine

Items	Value	Item	Value
Rated speed	500 rpm	Number of turns	25
Rated torque	11.5 Nm	Coil space factor	0.7
Rated current	7 A (RMS)	Current density	4.2 A/(mm)^2
Rated voltage	160 V (RMS)	Heat dissipation condition	Natural

4.4.1 Simulation Analysis

The simulation results of the magnetic fields and torque for 24-2-22 slot-PM Vernier machine have been presented here to verify the theory analysis.

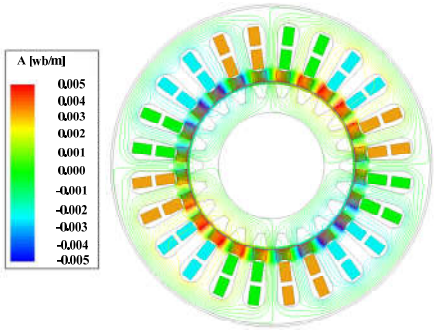

Fig. 4. 7. Exciting field distribution for 24-2-22 slot-PM Vernier machine.

Fig. 4. 7 gives the exciting field distribution for the studied machine. It is seen that due to the field modulation effect, the exciting field with 2 pole-pairs is produced in the windings. To further analyze the exciting field, the radial magnetic field intensity along air-gap is plotted in Fig. 4. 8 and its FFT analysis is given in Fig. 4. 9.

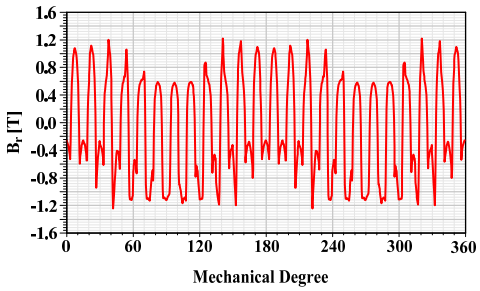

Fig. 4. 8. Radial exciting field intensity along air-gap for 24-2-22 slot-PM Vernier machine.

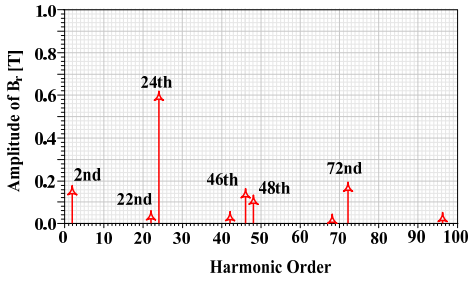

Fig. 4. 9. FFT analysis of radial exciting field intensity along air-gap for 24-2-22 slot-PM Vernier machine and 24-11 FSPM.

It is found that the dominant space harmonics are with the order of 24th, 72nd, 2nd, 46th and 48th. According to the data in Table III, the rotational speed of 24th, 72nd and 48th harmonics is zero, so they will not generate back-EMF. The magnitudes for 2nd and 46th harmonics are similar. However, their rational speeds have great difference, with -11ω_m for 2nd harmonic and 11ω_m /23 for 46th harmonic. So according to (4-9), 2nd harmonic will generate the dominant back-EMF. The highlight for Vernier machines is that the effective modulated magnetic field could have very fast speed to generate back-EMF for electromagnetic energy conversion. The other harmonics have the small magnitude or low speed, so they can be neglected almost and it is possible for back-EMF to obtain good sinusoidal waveform.

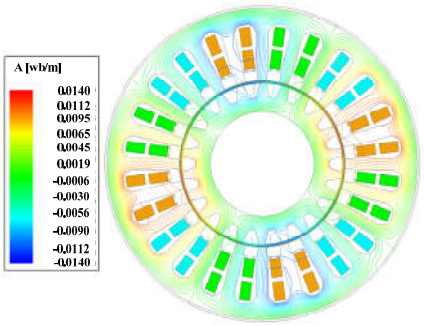

Fig. 4. 10. Armature field distribution for 24-2-22 slot-PM Vernier machine.

To demonstrate the paralleled magnetic path, the armature field is presented in Fig. 4. 10, where the PMs are removed for observation of the armature field. It is seen that the armature field goes through stator teeth, air-gap and rotor-teeth to form the loop without passing through the PMs.

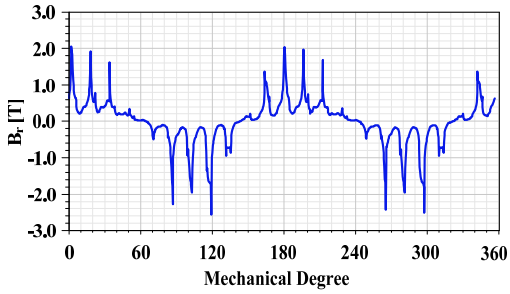

Fig. 4. 11. Radial armature field intensity along air-gap for 24-2-22 slot-PM Vernier machine.

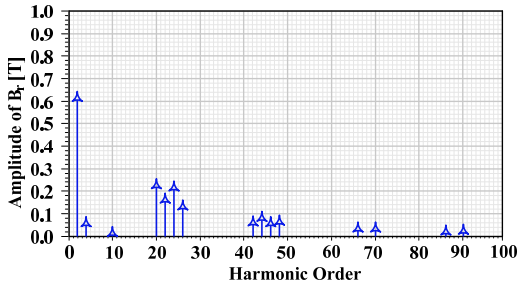

Fig. 4. 12. FFT analysis of radial armature field intensity along air-gap for 24-2-22 slot-PM Vernier machine.

Fig. 4. 11 gives the armature field intensity along air-gap and Fig. 4. 12 presents the corresponding FFT analysis. Due to the paralleled magnetic path, the armature field is much stronger than other machines. It is seen the dominant field with 2 pole-pairs could reach 0.63 T with current density of 4.2 A/(mm)^2. This strong armature field helps to improve the torque.

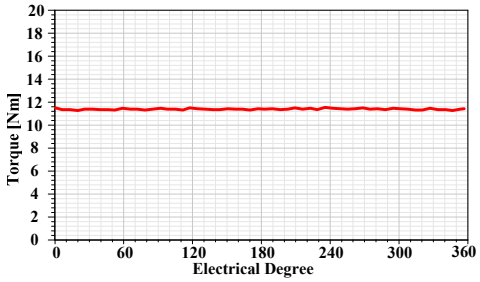

Fig. 4. 13. Simulation result of torque for 24-2-22 slot-PM Vernier machine.

Fig. 4. 13 presents the torque under rated conditions. It is shown the average value is 11.5 Nm and torque ripple (peak-peak) is 0.57 Nm, with about 5% of the average value.

4.4.2 Experimental Verification

The back-EMF, electromagnetic torque, cogging torque, power factor and efficiency for the prototype have been tested to evaluate the performance of proposed machine. Fig. 4. 14 gives the pictures of the prototype components and the testing bed. From Fig. 4. 14 (a) to Fig. 4. 14 (d), the stator, rotor, tor appearance and test bed is shown respectively. The steel lamination material is B50A470-A and PM material is NdFeB-N48SH. One aluminum shell with fins is used to package stator and rotor and to improve the heat dispassion.

(a) Stator.

(b) Rotor.

(c) Top appearance.

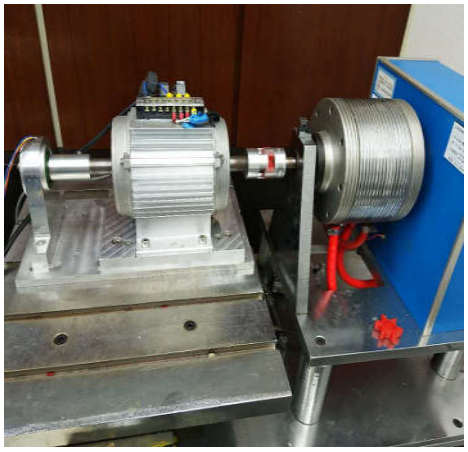

(d) Testing bed.

Fig. 4. 14. Pictures of the prototype.

Noticeably in Fig. 4. 14 (a), there is a special design in the top of the slots, where the two shoulders are shaped on both side of the teeth. The shoulders function as the holder of the PMs and as magnetic bridge to reduce flux leakage. This design makes this machine has stronger mechanical robust than other stator-PM machines which have PMs inserted in yoke or sandwiched between teeth.

More pictures are presented here to show the details of the experiments. Fig. 4. 15(a) shows the experimental field, Fig. 4. 15(b) shows the control board, Fig. 4. 15(c) shows the current sensor and Fig. 4. 15(d) shows the introductions of the power dynamometer.

(a) Experiment field.

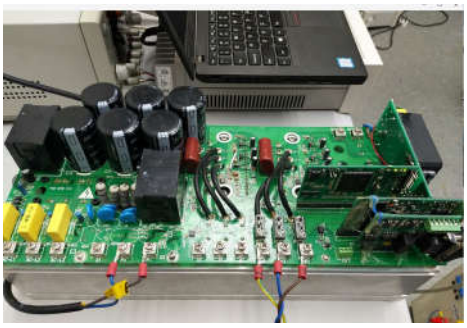

(b) Control board.

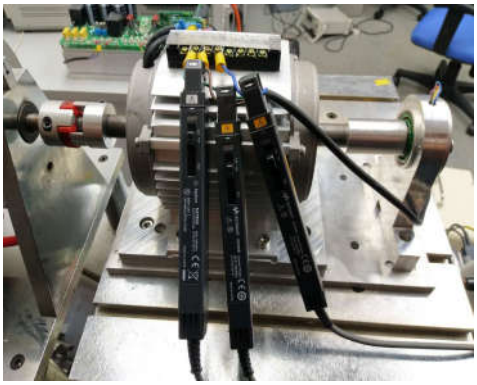

(c) Drive Current testing.

(d) Parameters of the power dynamometer.

Fig. 4. 15. Pictures of the testing field.

More pictures are given here to introduce the details of the manufacturing of the prototype. Fig. 4. 16 (a) is the shaft and bearings, Fig. 4. 16 (b) is the shell and the end plate, Fig. 4. 16 (c) shows the winding end, Fig. 4. 16 (d) shows the position sensor, Fig. 4. 17 (a) gives the appearance of the N48SH permanent magnet material and Fig. 4. 17 (b) gives the parameters of this material.

(a) Shaft and bearings.

(b) Shell and the end plate

(c) End of the winding.

(d) Position Sensor.

Fig. 4. 16. Pictures of the mechanical components and sensor.

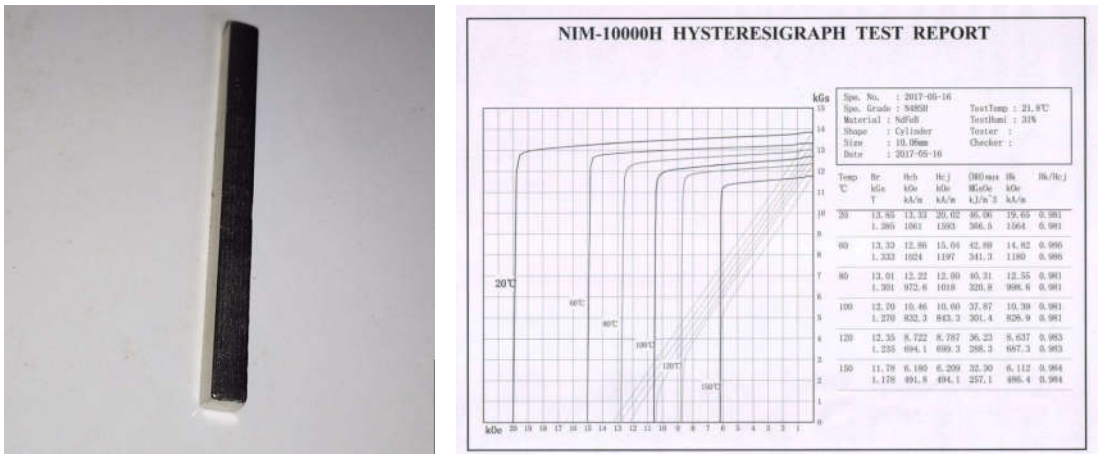

(a) Permanent Magnet. (b) Permanent Magnet B-H curve.

Fig. 4. 17. Pictures and parameters of the NdFeB permanent magnet.

Fig. 4. 18 presents the measured back-EMF and Fig. 4. 19 gives the simulation result for comparison. It is seen the tested waveform agrees well with the simulation analysis. Fig. 4. 20 gives FFT analysis for the tested data. It is shown that fundamental harmonic accounts majority of the waveform, with only about 5% THD.

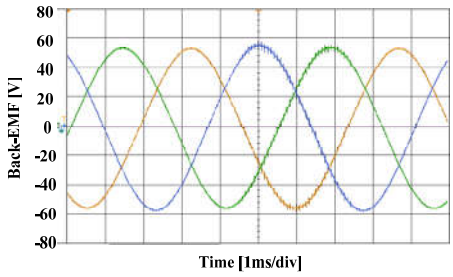

Fig. 4. 18. Measured three-phase Back-EMF waveforms.

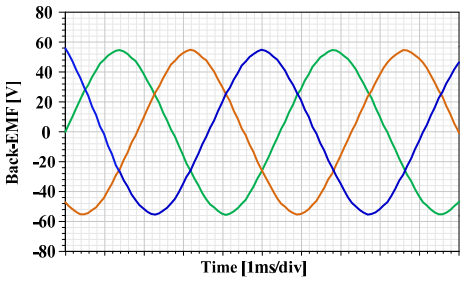

Fig. 4. 19. Simulation results of three-phase Back-EMF waveforms.

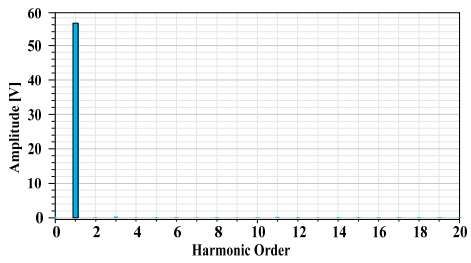

Fig. 4. 20. FFT analysis of one phase Back-EMF waveform.

Fig. 4. 21 presents the drive current and measured torque. The drive current is sinusoidal waveform

with rated 7 A (RMS) and the measured torque is about 11.5 Nm. The torque average value agrees well with simulation analysis. It is worth mentioning that the tested torque waveform could not reflect the instantaneous value because of the response delay of the power dynamometer and the interfering of the signal noise.

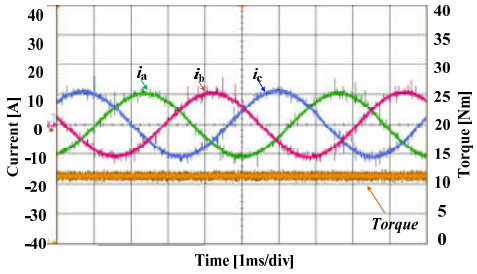

Fig. 4. 21. Measured drive current and torque waveforms.

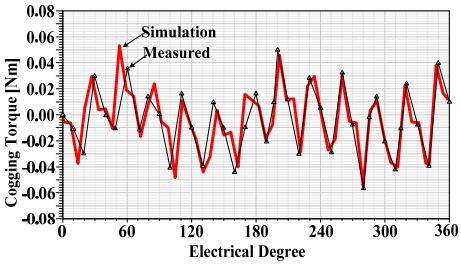

Fig. 4. 22. Measured and simulation results of cogging torque.

Fig. 4. 22 presents the simulation and experiment results of the cogging torque. The cogging torque is about 0.1 Nm (peak-peak), with only 0.8% of the rated torque. This small cogging torque is contributed by two factors. First one is the great lowest common multiple (LCM) of stator and rotor teeth. Second one is the even number of rotor teeth, which helps to eliminate the unbalanced magnetic force to avoid rotor off-centre.

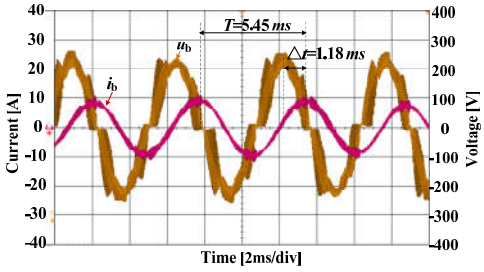

Fig. 4. 23. Measured power factor.

Fig. 4. 23 presents the tested power factor. It is seen that the phase difference for voltage and current is about 78 electrical degrees, so the power is about 0.2. The low power factor is caused by the large pole-pair number and the large inductance. For this machine, the inductance is much larger than the others with serial magnetic path because the armature filed will not the pass through the high magnetoresistance PMs.

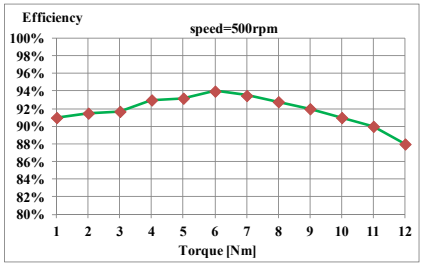

Fig. 4. 24. Measured efficiency under rated speed.

Fig. 4. 24 gives the measured efficiency under various torque and rated speed. It is seen that the average efficiency is about 90% in total torque range. This efficiency is lower than high speed machines, but has competitiveness for direct drive applications since the precise mechanical reducer such as harmonic gears and RV reducers usually have lower efficiency.

It is interesting to found that although this machine has very low power factor but has competitive efficiency. This is caused by the paralleled magnetic path. The armature field is much stronger than conventional machines under same copper loss, which helps to increase the torque. On the other hand, the heavy armature reaction will lower power factor simultaneously.

4.5 Comparison of Stator-PM Vernier Machine and FSCW Machine

In high torque and low speed applications, FSPMs are usually selected. So in this part, the performance of stator-PM Vernier machine and FSPM is compared and presented. To ensure the fairness of the comparison, the FSPM with 24 slots and 11 pole-pairs is selected. The same stator teeth with proposed machine could ensure same coil space factor, current density and heat dissipation, and 11 pole-pairs has the highest winding factor for 24 slots FSPM. Considering the drive frequency for prototype, the 24-2-22 stator-PM Vernier machine is selected for comparison, which has the second highest torque among 24 slots stator-PM Vernier machines.

Fig. 4. 25 and Table 4. 6 gives the simulation model and detailed dimensions of 24-11 FSPM. Similarly, the key parameters such as PM_Embrace, PM_Thick and Bs0 are also optimized. The other parameters such as out diameter, axial length, slot area and air-gap radius for these two machines maintain the same.

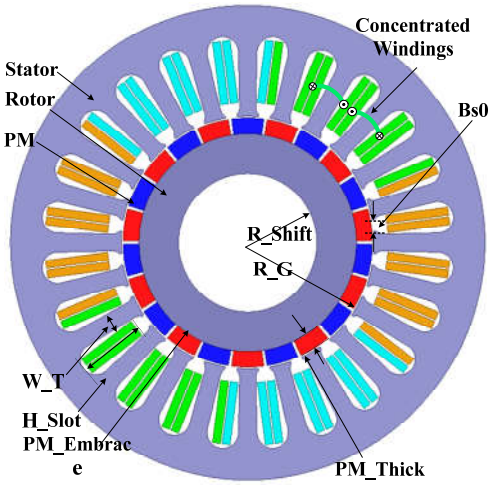

Fig. 4. 25. Simulation model of 24-11 FSPM.

Table 4. 6 key Parameters of 24-11 FSPM

Items	Value	Items	Value
Out Diameter	120 mm	W_T	4.6 mm
Axial Length	55 mm	H_Slot	18 mm
Air Gap	0.5 mm	PM_Embrace	0.9
R_G	31.75 mm	PM_Thick	4 mm
R_Shaft	20 mm	Bs0	3 mm

4.5.1 Exciting magnetic field intensity

Firstly, the exciting magnetic field intensity along air-gap of these two kinds of machines is simulated to reveal the different operation principle.

Fig. 4. 26 and Fig. 4. 27 presents the simulation results for stator-PM Vernier machine and FSPM respectively, and the Fig. 4. 28 gives the FFT analysis.

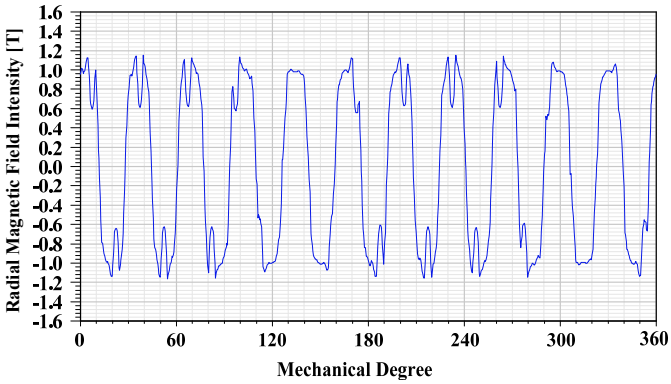

Fig. 4. 26. Radial magnetic field density along air-gap for 24-11 FSPM.

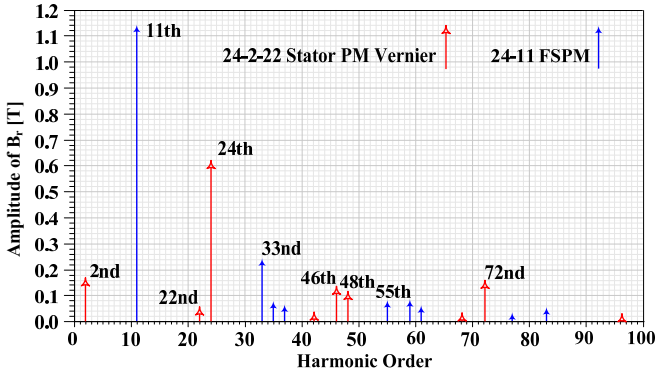

Fig. 4. 27. FFT analysis of radial magnetic field density along air-gap for 24-2-22 stator-PM Vernier machine and 24-11 FSPM.

It is found that in stator-PM Vernier machine, the dominant space harmonics are 24th, 72nd, 2nd, 46th and 48th. According to the data in Table 4. 3, the rotational speed of 24th, 72nd and 48th harmonics is zero, so they will not generate back-EMF. Although 2nd and 46th have almost the same magnitude, the rotational speeds have great difference, with -11ω_m for 2nd harmonic and 11ω_m /23 for 46th harmonic. So based on

(4-9), 2nd harmonic will generate the dominant back-EMF while the others have a marginal effect on effect.

While in 24-11 FSPM, the major space harmonics are 11th, 33rd and 55th, and they have the same rotational speed of ω_m. So they will all contribute to generate back-EMF.

4.5.2 Back-EMF

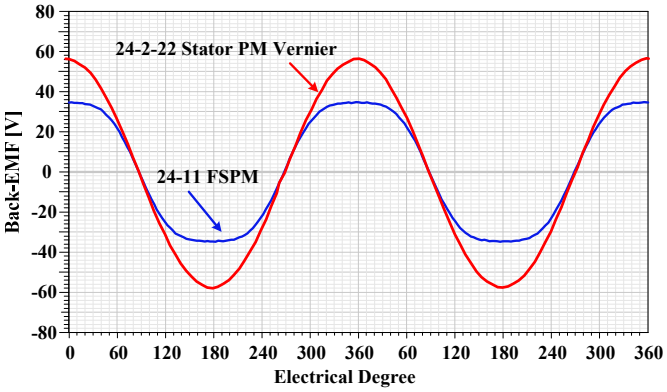

Fig. 4. 28. Simulation results of back-EMF waveforms for 24-2-22 stator-PM Vernier machine and 24-11 FSPM.

Fig. 4. 28 presents the back-EMF waveforms of these two machines under same speed. It is found that 24-2-22 stator-PM Vernier machine has higher amplitude and better waveform.

It is interesting to find that although the magnitude of 11th harmonic for FSPM is much higher than 2nd harmonic for 24-2-22 stator-PM Vernier machine, the back-EMF for FSPM is lower than stator-PM Vernier machine. This is because of the rotational speed of the harmonics, as the speed of 11th harmonic in FSPM is only 1/11 of 2nd harmonic in stator-PM machine, and according to (4-9), the rotational speed is proportional to back-EMF magnitude.

It is also found that the back-EMF harmonics for FSPM is richer than stator-PM Vernier machine. This is because of the effective components of the exciting magnetic fields. In stator-PM Vernier machine, 2nd harmonic is the dominant one and the others could be ignored basically, while in FSPM, besides 11th, 33rd and 55th will both have non-negligible effect.

4.5.3 Torque

The torque for 24-2-22 stator-PM Vernier machine and FSPM has also been compared, and the results are presented in Fig. 4. 29.

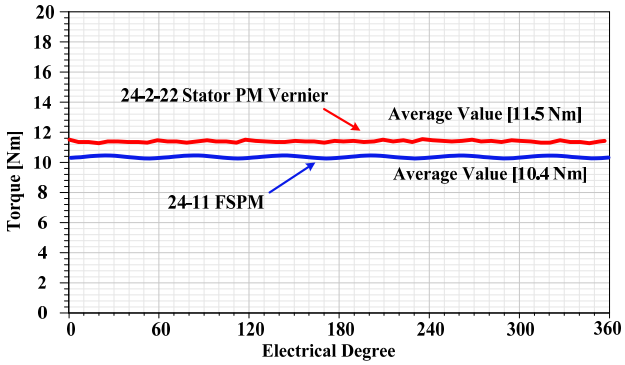

Fig. 4. 29. Simulation results of torque waveforms for 24-2-22 stator-PM Vernier machine and 24-11 FSPM.

It is seen that under same current, the torque is 11.5 Nm and 10.4 Nm for 24-2-22 stator-PM Vernier machine and 24-11 FSPM respectively. So under same volume and current, the torque for 24-2-22 stator-PM Vernier machine could be improved 10.5% over 24-11 FSPM.

Besides, without special design such as skewing slots or poles, the torque ripple for 24-2-22 stator-PM Vernier machine is about 5%, while for 24-11 FSPM, the torque ripple is 7%. So the torque ripple for the proposed stator-PM Vernier machine could be reduced 28% over 24-11 FSPM without other special torque ripple reduction techniques.

4.5.4 Power Factor

The power factor for these two machines has also been analyzed. Fig. 4. 30 presents the phase difference of drive current and voltage. It is seen that under same current, the phase difference is 78 degrees and 30 degrees for 24-2-22 stator-PM Vernier machine and 24-11 FSPM respectively. So the power factor for 24-2-22 stator-PM machine is much lower than 24-11 FSPM, with 0.21 to 0.87.

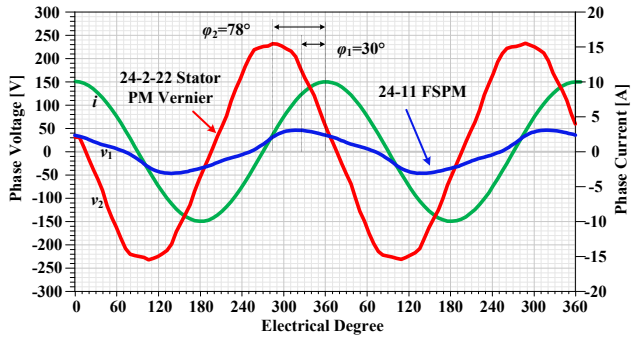

Fig. 4. 30. Simulation results of power factor for 24-2-22 stator-PM Vernier machine and 24-11 FSPM.

The factors contributing to low power factor for stator-PM Vernier machine will be analyzed blow. The vector diagram of current and voltage for PM machines is given in Fig. 4. 31. Where $\dot{\boldsymbol{E}}_0$ is the phase non-load back-EMF, $\dot{\boldsymbol{I}}_s$ is the phase current, ω_s is the angular velocity of current, L_s is the phase inductance, $\dot{\boldsymbol{U}}_s$ is the phase voltage and $\boldsymbol{\varphi}$ is the power factor angle.

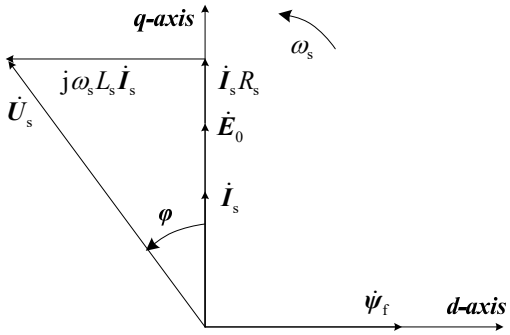

Fig. 4. 31. Voltage and current vector diagram of permanent magnet machines.

It is seen that the inductance and current frequency are the major factors which increase the power factor angle. Under same speed, the current frequency for 24-2-22 stator-PM Vernier machine is twice of the 24-11 FSPM. While for inductance, the value is about 20 mH and 5 mH for Vernier machine and FSPM respectively. The large inductance value for Vernier machine is caused by the paralleled magnetic path. Since the armature magnetic field does not pass the PMs, the inductance could be increased significantly.

It is noteworthy that low power factor for stator-PM Vernier machine did not result in the low efficiency. It is verified that under same speed and copper loss, the torque for 24-2-22 stator-PM Vernier machine is higher than 24-11 FSPM, so if core loss and mechanical loss are not considered, stator-PM Vernier machine has higher efficiency. The low power factor for stator-PM machine is caused by the strong armature magnetic field, which is a double-edge sword. On one hand, the stronger armature magnetic under same current helps to increase the torque. On the other hand, the heavy armature reaction lowers the power factor. The disadvantage for low power factor for stator-PM Vernier machine is that the high voltage power switches should be used for drive, which may increase the system cost.

4.6 Conclusion

This chapter proposes one kind of novel slot-PM consequent pole Vernier machines with paralleled magnetic path. The operation principle is introduced and the combinations of winding and rotor poles are discussed. One 24-2-22 machine prototype is built and tested. The results show that this machine has great potential in direct drive application. It is shown that the torque density could reach 3 Nm/kg under natural cooling, THD for back-EMF is only about 5%, cogging torque is only about 0.8%, electromagnetic torque ripple is merely 5% and efficiency could reach 90%. However, the power factor for this machine is low, with only about 0.2. So under same current, higher voltage is required for drive. It is suggested to reduce the winding turns and apply multi paralleled conductors to balance the drive voltage and current.

Chapter 5 Design and Verification of Dual-PM Excitation Vernier Machine for Robotic Applications

In the last three chapters, three kinds of stator-PM machines are proposed. It is found that the stator-PM Vernier machines have the large-torque and low-speed characteristics, which are most suitable for direct drive applications. In this chapter, one novel dual-PM excitation Vernier machine is investigated. Generally, this kind of machines have PMs on stator, so they belong to stator-PM machine, meanwhile, this kinds of machines also have PMs on rotor, so they also belong to rotor-PM machine. Precisely, this kind of machines lies in the intersection of rotor-PM and stator-PM machines. They have similar characteristics with stator-PM Vernier machines. Meanwhile, with the assistant PMs in the rotor, these machines have better performance than stator-PM Vernier machines. It is found that this kind of machines is the best candidate for direct-drive robotic applications.

In this Chapter, one novel dual-PM excitation Vernier Machine with short-pitch distributed windings is investigated. The operation principle is introduced and the prototype is tested. The essential issues mentioned above are addressed and the advantages of the used techniques such as paralleled magnetic path, distributed windings and short-pitch are discussed in detail.

5.1 Topology and Design Parameters of the Proposed Machine

5.1.1 Topology

Fig. 5. 1 shows the topology of the proposed machine, which has 24 slots, 22 rotor pole-pairs and 2 winding pole-pairs. The PMs with same magnetized direction are installed in the slots opening of both rotor and stator. Two special shoulders are designed in each stator tooth to fix the stator-PMs.

Fig. 5. 2 shows the winding distributions, where the 5/6 short-pitch coils is artificially applied to eliminate 3rd, 5th and 7th back-EMF harmonics so as to reduce torque ripple. The effectiveness of this design will be explained in section III when the winding factor and back-EMF waveform are discussed.

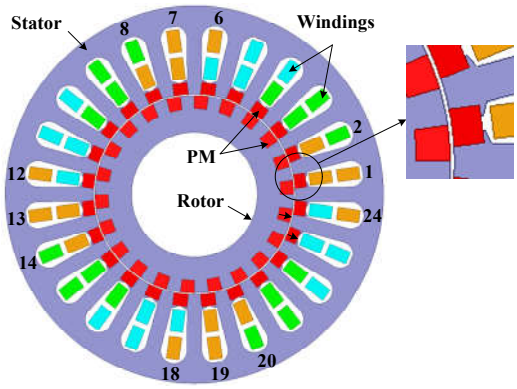

Fig. 5. 1 Topology of the proposed dual-PM excitation Vernier machine.

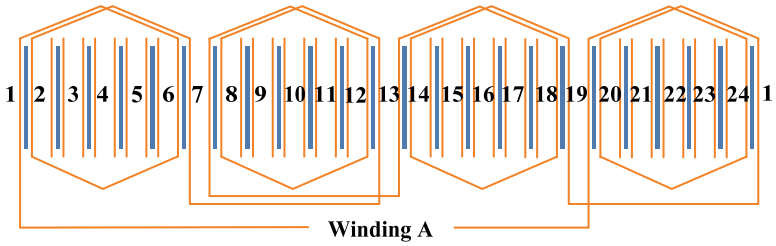

Fig. 5. 2. Winding distribution of the proposed dual-PM excitation Vernier machine.

5.1.2 Design Parameters

Fig. 5. 3 illustrates the key dimensions of the proposed machine and Table 5. 1 shows their values. To obtain maximum torque, the key dimensions such as W-SPM, H-SPM, W-RPM and H-RPM shown in Fig. 5. 3 are optimized by using the genetic algorithm toolbox in Ansoft Maxwell software.

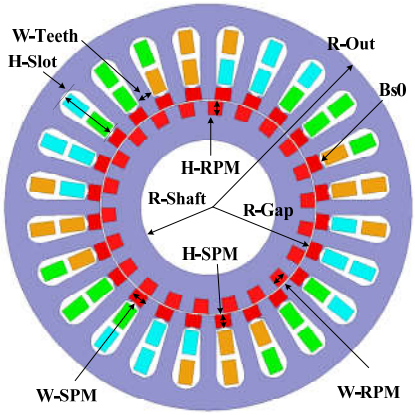

Fig. 5. 3. Key dimensions of the proposed dual-PM Vernier machine.

Table 5. 1 Key dimensions of the proposed dual-PM Vernier machine.

Items	Value	Items	Value
R-Out (mm)	60	H-Slot (mm)	18
Axial Length (mm)	55	W-SPM (mm)	4.4
Air Gap (mm)	0.5	H-SPM (mm)	4.1
R-Gap (mm)	31.75	W-RPM (mm)	4.4
R-Shaft (mm)	20	H-RPM (mm)	3.7
W-Teeth(mm)	4.6	Bs0 (mm)	1.7

Table 5. 2 shows the key design parameters of the proposed machine. The designed rated speed is 200 rpm targeting for the low-speed high-torque robotic drive applications and the current density is set as 4.1 A/(mm) ^2 under natural ventilation.

Table 5. 2 Key Design Parameters of the proposed dual-PM Vernier machine.

Items	Value	Items	Value
Rated speed (rpm)	200	Number of turns	25
Rated torque (Nm)	21.5	Coil space factor	0.7
Rated current A (RMS)	7	Current density A/(mm)^2	4.2
Rated Power (W)	450	Heat dissipation condition	Natural ventilation

5.2 Principle of the Dual-PM Exciting Vernier Machines

5.2.1 Equivalent Model

To better understand the principle of this dual-PM excitation machine, the equivalent model is proposed. Then based on the model, the components of the excitation field are analyzed, the winding factors for these field components are calculated and finally, the back-EMF and torque are analyzed.

This dual-PM excitation machine can be regarded as the integration of one rotor-PM Vernier machine and one stator-PM Vernier machine, as shown in Fig. 5. 4. The rotor-PM machine has the rotor with 22 teeth and 22 pieces of PM and the stator with 24 slots with 2 pole-pairs windings. The stator-PM machine has the same rotor but with PM removed and the same stator but with 24 pieces of PM installed in the slot openings. The excitation fields produced by the rotor-PM or the stator-PM have the same pole pair and the same rotational velocity as shown in Fig. 5. 4, so these two machines can be combined together. So figuring out the characteristics of the excitation field components produced by rotor-PM and stator-PM separately, including pole-pair, intensity and rotational velocity is the key to reveal the principle of this machine.

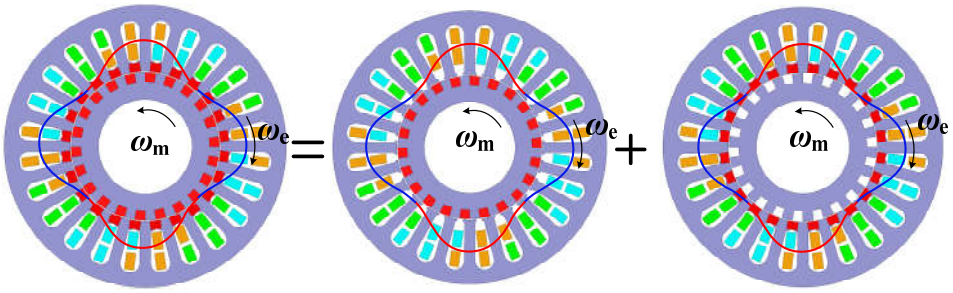

Fig. 5. 4. Basic operation principle of the proposed dual-PM excitation machine.

5.2.2 Excitation Field Components

Fig. 5. 5 shows the simulation results of the rotor-PM excitation fields, in which Fig. 5. 5(a) shows the field distribution and Fig. 5. 5(b) gives the waveform of the radial magnetic intensity along air-gap.

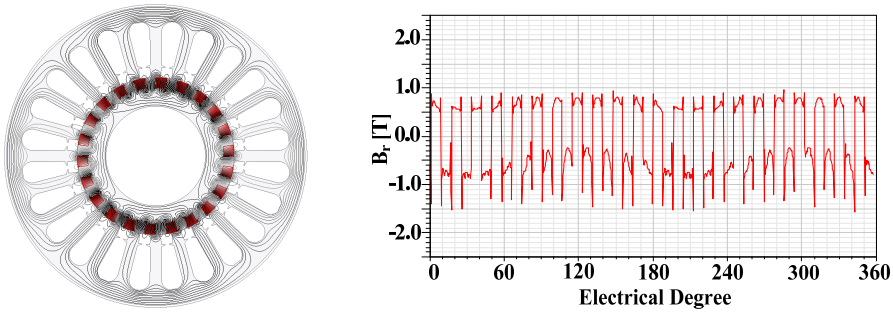

(a) Field distribution. (b) Radial magnetic intensity along air-gap.

Fig. 5. 5. Rotor-PM excitation field.

To figure out the pole-pairs of the excitation fields, the FFT analysis of the radial magnetic intensity is conducted and shown in Fig. 5. 6.

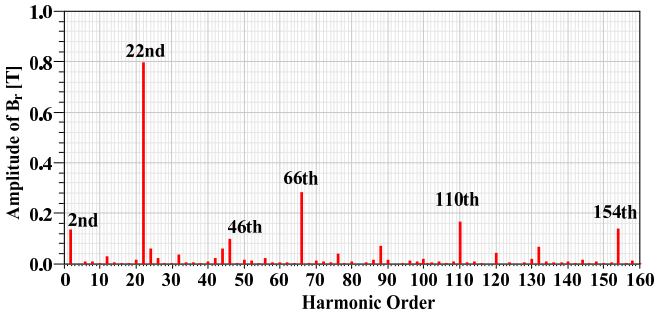

Fig. 5. 6. FFT analysis of the rotor-PM excitation field intensity.

Ignoring the harmonics with the amplitude of less than 0.1 T, it is found that rotor-PM excitation fields have the components of 22nd, 66th, 110th, 154th, 2nd and 46th harmonics. Since the fundamental harmonic of the FFT analysis is the circumference of the air-gap, the harmonic orders here represent the pole-pairs of the excitation field components. The rational velocities of these field components are also need to be figured out.

Using P_{ER} to represent the pole-pair and ω_{ER} to represent the rotational velocity of the excitation field components, according to the magnetic field modulation theory, P_{ER} and ω_{ER} can be expressed in Eq. (5-1).

$$\begin{cases} P_{ER} = \left| uP_{PMR} + vN_S \right| \\ \omega_{ER} = \dfrac{uP_{PMR}}{uP_{PMR} + vN_S}\omega_m + \dfrac{vN_S}{uP_{PMR} + vN_S}\omega_{Ns} \\ u = 1,3,5 \ldots v = 0,\pm 1,\pm 2.. \end{cases} \quad (5\text{-}1)$$

where P_{PMR} is the pole-pair number of rotor-PM, N_S is the stator teeth number, ω_m is the mechanical rotational velocity of rotor and ω_{NS} is the rotational velocity of the stator teeth.

Combing with the data in Fig. 5. 6, the pole-pairs, magnetic intensity and velocity of the field components can be figured out. The corresponding data is listed in Table 5. 3.

Table 5. 3 Pole-pairs, Intensity and Velocity of the Rotor-PM Excitation Field

P_{ER}	(u,v)	B_{ER} (T)	ω_{ER}	P_{ER}	(u,v)	B_{ER} (T)	ω_{ER}
2	(1,-1)	0.14	$-11\omega_m$	66	(3,0)	0.28	ω_m
22	(1,0)	0.8	ω_m	110	(5,0)	0.16	ω_m
46	(1,1)	0.10	$11\omega_m/23$	154	(7,0)	0.15	ω_m

The intensity and velocity determine the back-EMF generating capability simultaneously, so the velocity of the fields should be watched. It is found that the field with 2 pole-pairs has -11 times of ω_m, the fields with 22, 66, 110, 154 pole-pairs have same velocity with ω_m and the field with 46 pole-pairs has 11/23 of ω_m.

The stator-PM generated fields are also analyzed in the similar way. Fig. 5. 7(a) shows the field distribution, Fig. 5. 7(b) presents the waveform of the radial magnetic intensity along air-gap and Fig. 5. 8 shows the corresponding FFT analysis of the waveform.

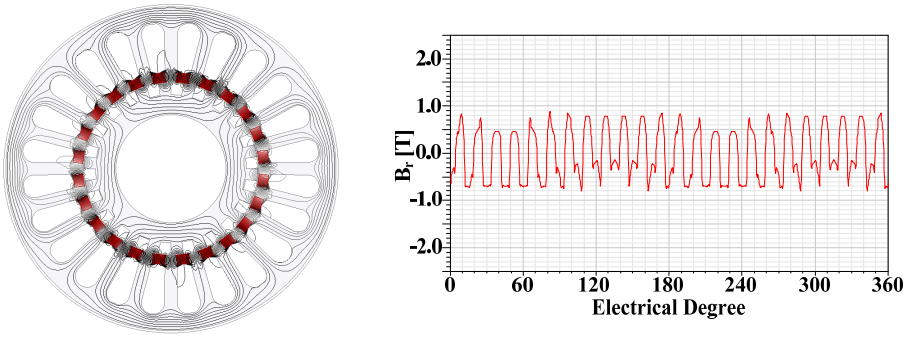

(a) Field distribution. (b) Radial magnetic intensity along air-gap.

Fig. 5. 7. Stator-PM excitation field.

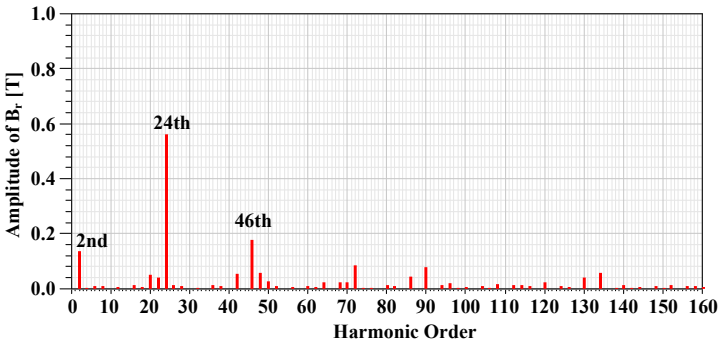

Fig. 5. 8. FFT analysis of the stator-PM excitation field intensity.

Ignoring the harmonics with amplitude of less than 0.1 T, it is observed that the main stator-PM generated fields have the pole-pairs of 2, 24 and 46. By using field modulation theory, the pole-pair P_{ES} and velocity ω_{ES} of the fields produced by stator-PM can be expressed as:

$$\begin{cases} P_{ES} = \left| mP_{PMS} + nN_R \right| \\ \omega_{ES} = \dfrac{mP_{PMS}}{mP_{PMS} + nN_R}\omega_{PM} + \dfrac{nN_R}{mP_{PMS} + nN_R}\omega_m, \\ m = 1,3,5 \ldots n = 0, \pm 1, \pm 2 \ldots \end{cases} \quad (5\text{-}2)$$

where P_{PMS} is the pole-pairs of stator-PMs, N_R is the rotor teeth and ω_{PM} is the velocity of the stator-PMs. Noticeably, the PMs here are stationary and modulators are the rotor teeth, while in (5-1), the PMs are rotary and modulators are the stator teeth.

Similarly, combing with the data in Fig. 5. 8, the pole-pairs, intensity and velocities of the stator-PM excitation fields can be figured out. The corresponding data is listed in Table 5. 4.

Table 5. 4 Pole-pairs, Intensity and Velocity of the Stator-PM Excitation Field.

P_{ES}	(m,n)	B_{ES} (T)	ω_{ES}
2	(1,-1)	0.14	$-11\omega_m$
24	(1,0)	0.56	0
46	(1,1)	0.18	$11\omega_m/23$

It is interesting to find that for the stator-PM excitation fields, the component with 2 pole-pairs also has -11 times of ω_m and the component with 46 pole-pairs also has 11/23 of ω_m, exactly same with the situation in the rotor-PM machine. Since the dominant field components produced by the rotor-PM and stator-PM have same pole-pair and same velocity, it is reasonable to integrate these two machines together, as shown in Fig. 5. 4 to intensify the field to increase torque. This reveals the basic principle of the proposed dual-PM excitation machine.

The final excitation field produced by both stator-PM and rotor-PM has also been analyzed and presented to verify the independent analysis. Fig. 5. 9(a) presents the field distribution of the dual-PM excitation field, Fig. 5. 9(b) gives the waveform of radial magnetic intensity along air-gap and Fig. 5. 10 shows the FFT analysis of the dual-PM excitation filed intensity.

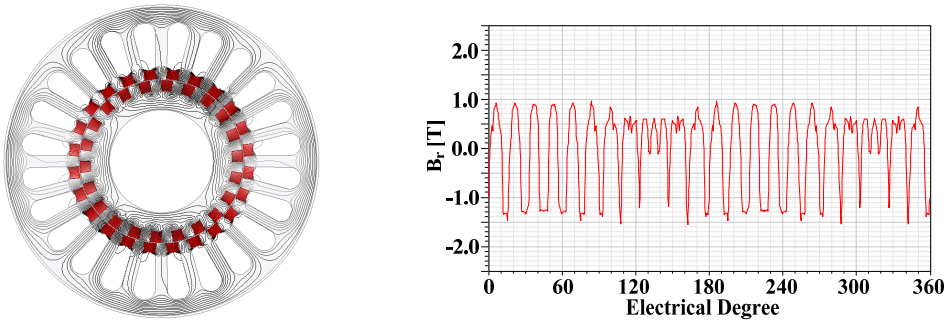

(a) Field distribution. (b) Radial magnetic intensity along air-gap.

Fig. 5. 9. Dual-PM excitation field produced.

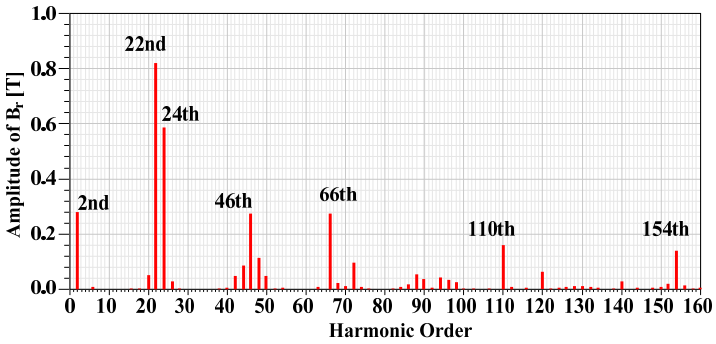

Fig. 5. 10. FFT analysis of the dual-PM excitation field intensity.

Similarly, ignoring the harmonics with amplitude of less than 0.1 T, there are main seven components of the dual-PM excitation fields. Based on the above analysis, it is known that the 2nd and 46th harmonics are produced by both rotor-PM and stator-PM, 24th harmonic is produced by stator-PM and 22nd, 66th, 110th, 154th harmonics are produced by rotor-PM. It is fund that 2nd harmonic has the maximum product of intensity and velocity, so it will be the dominant effective excitation field.

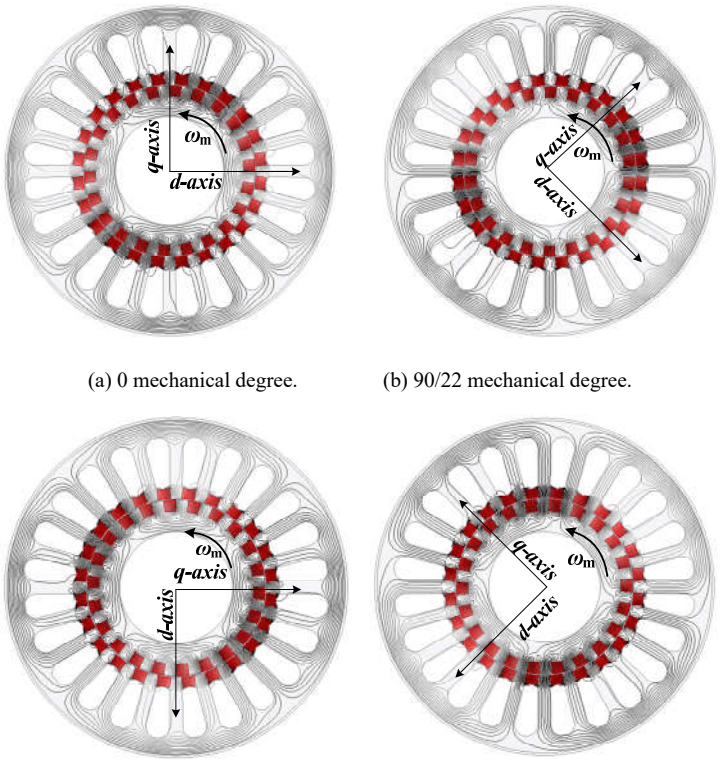

(a) 0 mechanical degree. (b) 90/22 mechanical degree.

(c) 180/22 mechanical degree. (d) 270/22 mechanical degree.

Fig. 5. 11. Excitation flux distribution of the proposed dual-PM Vernier machine when rotor at different positions.

The field distributions produced by dual-PM at different positions are presented in Fig. 5. 11 to further explain the principle. It is observed that there is the field with 2 pole-pairs in the stator area. From Fig. 5. 11(a) to Fig. 5. 11(d), the rotor moves 270/22 degrees while the *d-axis* of the rotor moves -135 degrees. So the velocity of the field with 2 pole-pairs has -11 times of ω_m, which verified the theory analysis.

It is known that in conventional PMSMs, the high order harmonics will cause back-EMF distortion and

torque ripple. However, it is found that in this dual-PM excitation Vernier machine, the excitation field has much more harmonics. So what their influences to back-EMF should be figured out.

5.2.3 Winding Factors

To analyze the influence of excitation harmonics to the final back-EMF in phase winding, the winding factors for each harmonic should be figured out.

According to the winding theory, the pole pitch τ, slot-pitch angle α, slots per pole per phase q and coil-pitch y_1 can be calculated by:

$$\begin{cases} \tau = \dfrac{Z_s}{2P_W} = 6 \\ \alpha = \dfrac{2\pi P_W}{Z_S} = \dfrac{\pi}{6} \\ q = \dfrac{Z_S}{2mP_W} = 2 \\ y_1 = 5 \end{cases} \tag{5- 3}$$

where P_W is the winding pole-pair number.

The coil-pitch factor k_{yP_E}, winding distribution factor k_{qP_E}, and winding factor k_{wP_E} for the field components with P_E pole-pairs can be expressed as:

$$\begin{cases} k_{yP_E} = \sin\left(\dfrac{y_1}{\tau}\dfrac{\pi}{2}\dfrac{P_E}{P_W}\right) \\ k_{qP_E} = \dfrac{\sin\left(\dfrac{q\alpha}{2}\dfrac{P_E}{P_W}\right)}{q\sin\left(\dfrac{\alpha}{2}\dfrac{P_E}{P_W}\right)} \\ k_{WP_E} = k_{yP_E}k_{qP_E} \end{cases} \tag{5- 4}$$

where P_E is the pole-pair number of the excitation field component.

The calculated results of coil-pitch factor, winding distribution factor and winding factor for the main excitation field components are shown in Table 5. 5.

Table 5. 5 Coil-pitch Factor, Winding Distribution Factor and Winding Factor for Main Excitation Field Components

P_E	k_y	k_q	k_W	P_E	k_y	k_q	k_W
2	0.97	0.97	0.93	66	-0.71	-0.71	0.5
22	0.97	-0.97	-0.93	110	0.26	-0.26	-0.07
24	0	-1	0	154	0.26	0.26	0.07
46	-0.97	0.97	-0.93				

5.2.4 Back-EMF and Torque

The back-EMF e_{P_E} produced by the excitation field component with P_E pole-pair number can be calculated by:

$$e_{P_E} = lr_g N k_{WP_E} B_E |\omega_E| \sin(P_E \omega_E t) \tag{5- 5}$$

where l is the axial length of the machine, r_g is the air-gap radius, N is the conductor number, B_E and ω_E is

the magnetic intensity and velocity of this field component. Noticeably, B_E is produced by both of the rotor-PM and stator-PM, which is the sum of B_{ER} and B_{ES}.

Taking the data in Table 5. 3, Table 5. 4 and Table 5. 5 into (5-7), the back-EMF component caused by the corresponding excitation field can be calculated and the results are listed in Table 5. 6.

Using the standard unitary expression, the amplitudes of each back-EMF component A_E are written as the percentage of maximum value.

Table 5. 6 Amplitude and Velocity of Different Back-EMF Components

P_E	*Back-EMF*		P_E	*Back-EMF*	
	A_E (p.u)	$\boldsymbol{P_E\omega_E}$		A_E	$\boldsymbol{P_E\omega_E}$
2	1.0	$-22\boldsymbol{\omega_m}$	66	0.05	$66\boldsymbol{\omega_m}$
22	-0.26	$22\boldsymbol{\omega_m}$	110	-0.003	$110\boldsymbol{\omega_m}$
24	0	0	154	0.003	$154\boldsymbol{\omega_m}$
46	-0.04	$22\boldsymbol{\omega_m}$			

The final back-EMF for phase A could be expressed by:

$$e_A = \sum_{i=1}^{7} A_E \sin(P_E \omega_E t) \tag{5- 6}$$

According to the data in Table 5. 4 and Eq. (5-8), it is found that the fundamental harmonic for the back-EMF has the velocity of $22\omega_m$. The excitation fields with 2, 22 and 46 pole-pairs have positive contribution to the fundamental harmonic and they account for 77%, 20% and 3% to total back-EMF respectively. The excitation field with 24 pole-pairs has no influence to the back-EMF due to either of the zero winding factor or the zero rotational velocity. The field components with 66, 110 and 154 pole-pairs produce the 3rd, 5th and 7th harmonics of the back-EMF.

By further analysis, it is found that 3rd, 5th and 7th harmonic account for 3.8%, 0.2% and 0.2% of the fundamental harmonic. The THD for the back-EMF waveform is 3.8%. This is contributed by the short pitched coil design. If the full pitch winding is used, which means y_1 equal 6 in (5), the 3nd, 5th and 7th harmonics will account 8.5%, 1.7% and 1.7% respectively and the THD will reach 8.8%. This is the purpose that the 5/6 short-pitch winding is used for this dual-PM excitation Vernier machine.

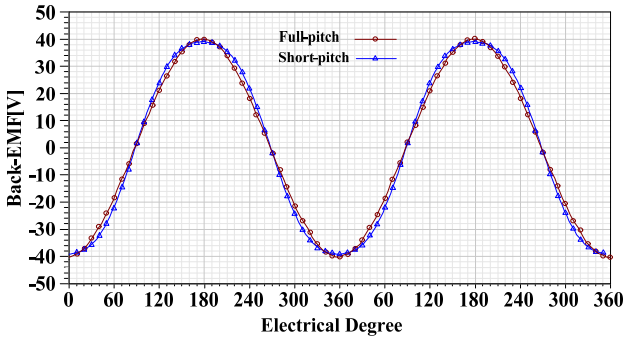

Fig. 5. 12. Simulation result of the Back-EMF for short-pitch and full-pitch coils dual-PM Vernier machine.

The simulations results of back-EMF waveforms for this machine by using short-pitch coils and full-pitch coils are presented in Fig. 5. 12 to verify the theoretical analysis. It is found that for the full-pitch

machine, the crest and trough of the waveform appears flat, which is caused mainly by the low older odd harmonics namely 3rd, 5th and 7th harmonics, while for the short-pitch machine, the back-EMF is better sinusoidal waveform.

With the data in Table 5. 3 and Table 5. 4, the contribution of the rotor-PM and stator-PM to the final back-EMF could also be figured out. It is found that rotor-PM and stator-PM contributes 59% and 41% of the final back-EMF respectively. Rotor-PM has 18% higher contribution than the stator-PM, which is mainly caused by the field component with 22 pole-pairs. This component only exists in the rotor-PM machine but not in the stator-PM machine. To verify the analysis, the simulations based on finite-element method are conducted. Fig. 5. 13 shows the phase back-EMF waveforms for rotor-PM excitation machine, stator-PM excitation machine and dual-PM excitation machine. It is found that the back-EMF amplitudes for rotor-PM excitation, stator-PM excitation and dual-PM excitation machines are 24 V, 17 V and 41 V respectively. The rotor-PM and stator-PM contributes 60% and 40% respectively to the final back-EMF, which agrees well with theory analysis.

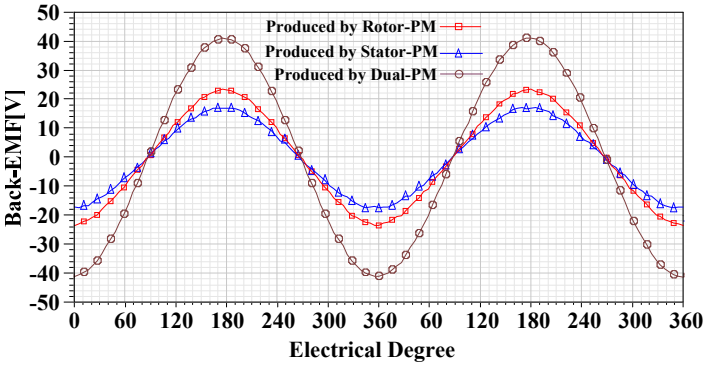

Fig. 5. 13. Simulation result of the Back-EMF produced by rotor-PM, stator-PM and dual-PM Vernier.

The torque contributed by the rotor-PM, stator-PM and dual-PM is also analyzed. It is found in Fig. 5. 14 that with only rotor-PM excitation, the average torque is 12.75 Nm, with only stator-PM excitation, the average torque is 8.8 Nm and with dual-PM excitation, the average torque is 21.5 Nm. The rotor-PM and stator-PM contribute about 60% and 40% of the total torque, which agrees with the theoretical analysis well.

In addition, since the back-EMF waveform in Fig. 5. 12 has good sinusoidal waveform, the torque ripple for dual-PM excitation machine is small. It is observed that the peak-peak torque value is about 0.8 Nm, accounting for only 3.7% of the rated torque. This small torque ripple is mainly contributed by the 5/6 short-pitch design.

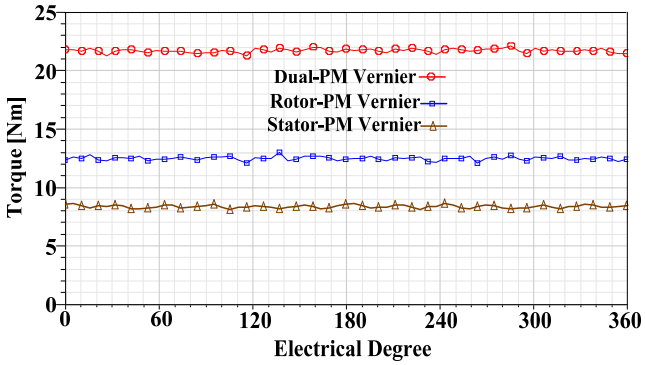

Fig. 5. 14. Simulation result of the torque for the rotor-PM, stator-PM and dual-PM Vernier machine.

Paralleled magnetic path is the major characteristic of this dual-PM excitation Vernier machine. Due to the paralleled magnetic path, the average permeability of the magnetic path is significantly improved. Consequently under the same MMF, the proposed machine could get stronger field in the air-gap, so the torque could be improved. This characteristic is introduced here and its advantage is demonstrated by comparing with conventional Vernier machine.

5.3 Characteristic of the Proposed Dual-PM Excitation Machine

5.3.1 Armature Field Strengthening Effect

To demonstrate the armature field strengthening effect of the paralleled magnetic path characteristic, the armature magnetic field of the proposed dual-PM Vernier machine and the conventional rotor-PM Vernier machine are simulated and presented in Fig. 5. 15, where the material of PMs is assigned as vacuum to remove the influence of excitation MMF. The rotor-PM Vernier machine has 22 pole-pairs of PM in rotor and 2 pole-pairs of windings. The key dimensions for these two machines maintain the same.

It is observed that for the dual-PM Vernier machine, the armature field goes through stator teeth, air-gap and rotor-teeth to form the loop, without passing the PMs. While for the conventional rotor-PM Vernier machine, the armature filed has to pass the PMs to form the loop. Since the permeability of the PMs is as small as vacuum, so under same MMF, the magnetic field in air-gap of dual-PM Vernier machine could be much stronger than conventional rotor-PM Vernier machine.

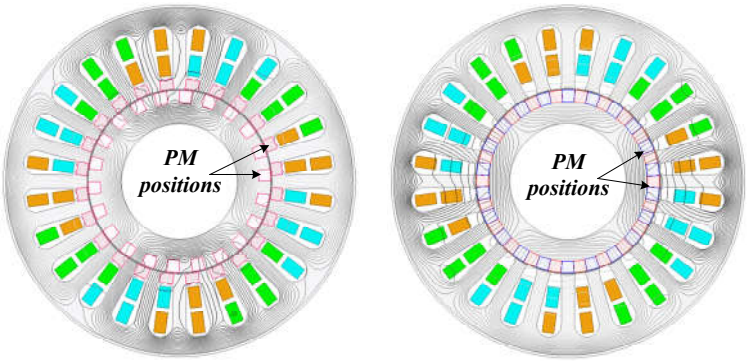

(a) For proposed dual-PM Vernier machine. (b) For rotor-PM Vernier machine.

Fig. 5. 15. Armature magnetic field distribution.

Fig. 5. 16 shows the simulation results of the armature magnetic field intensity along air-gap for the proposed dual-PM Vernier machine and the conventional rotor-PM Vernier machine, and Fig. 5. 17 presents the FFT analysis of the waveforms.

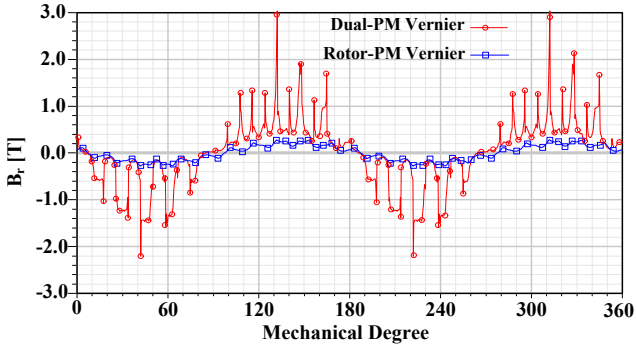

Fig. 5. 16. Radial armature magnetic field intensity along air-gap of the proposed dual-PM Vernier machine and rotor-PM Vernier machine.

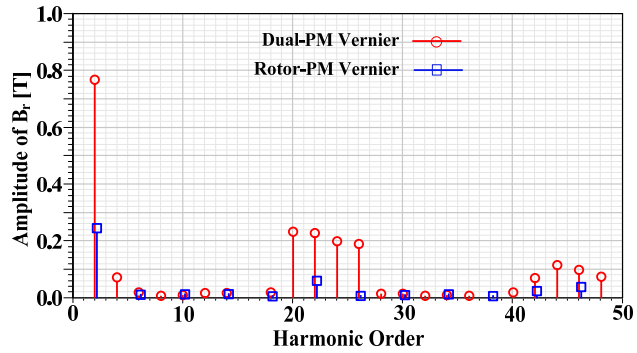

Fig. 5. 17. FFT analysis of the armature magnetic field intensity in air-gap for the proposed dual-PM Vernier machine and rotor-PM Vernier machine.

It is observed that under same MMF, for the dominant effective harmonic with the pole-pairs of 2, the amplitude for dual-PM and conventional Vernier machine is 0.76 T and 0.24 T respectively. The paralleled magnetic path generates much stronger field intensity under same MMF. From the other perspective, the half-closed slot structure for rotor and stator actually increases the average permeance of the air-gap, which is equivalent to reduce the air-gap. So naturally, the field intensity and the torque of the proposed machine could be improved.

5.3.2 Torque Improvement Advantage

To verify the advantage of the proposed dual-PM Vernier machine over conventional rotor-PM Vernier machine, Fig. 5. 18 gives the simulation results of the torque for them. It is found that the average torque for the proposed machine and conventional machine is 21.5 Nm and 11.5 Nm respectively. The torque density for the proposed machine is about 1.87 times of the conventional Vernier machine.

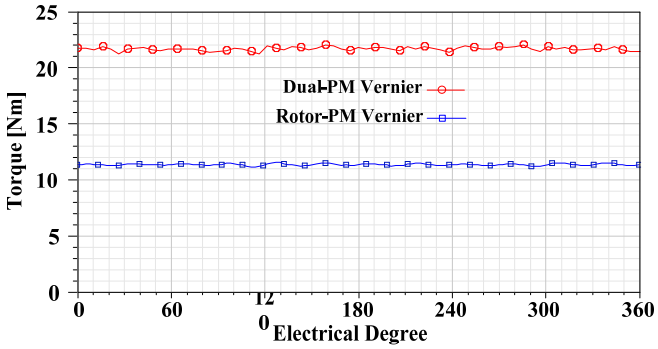

Fig. 5. 18. Simulation results of torque for the proposed dual-PM Vernier machine and rotor-PM Vernier machine.

5.4 Experimental Verification of the Dual-PM Excitation Machine

To verify the performance of the dual-PM excitation Vernier machine, the prototype has been built and tested. The data in terms of back-EMF, torque and efficiency have been tested.

(a) Stator. (b) Rotor.

(c) Appearance of the prototype. (d) Testing system.

Fig. 5. 19. Pictures of the prototype and testing bed.

Fig. 5. 19 (a) to Fig. 5. 19 (d) gives the pictures of the stator, rotor, prototype appearance and testing system. The steel lamination material is B50A470-A and PM material is NdFeB-N38EH. One aluminum shell with fins is used to package stator and rotor and to improve the heat dispassion. The total weight of the machine is about 3.6 kg.

Fig. 5. 20 gives the no-load back-EMF waveforms when the prototype operates at rated 200 rpm. It is seen that the measured back-EMF has good sinusoidal waveform. To find out the THD of the waveform, the FFT analysis is conducted based on the measured data and the result is shown in Fig. 5. 21. It is seen

that the 3rd harmonic has the amplitude of 1.5 V, accounting 3.6 % of the fundamental harmonic. The 5th and 7th harmonics have the neglectable influence contributed by the short-pitch design. The total THD for the measured back-EMF is about 3.6%, which agrees well with the analysis.

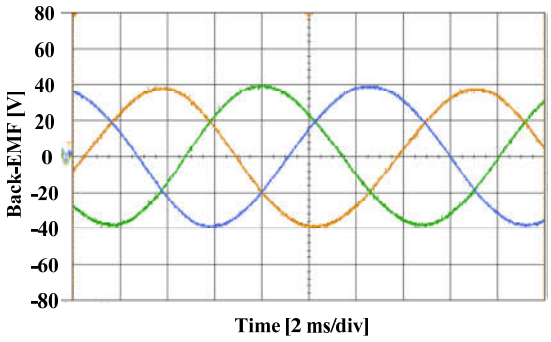

Fig. 5. 20. Measured three-phase Back-EMF waveforms.

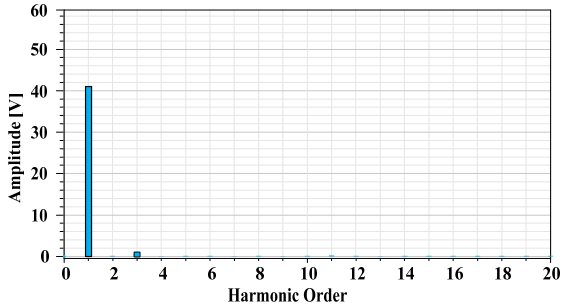

Fig. 5. 21. FFT analysis of one phase Back-EMF waveform.

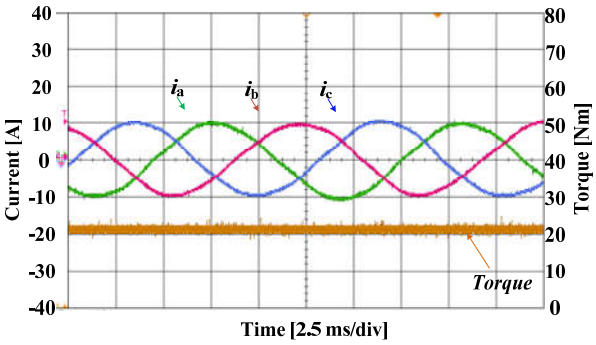

Fig. 5. 22. Measured drive current and torque waveforms.

Fig. 5. 22 gives the drive current and measured torque. The drive current is sinusoidal waveform with 10A amplitude and the measured torque is about 21.5 Nm. The average torque value agrees well with simulation analysis. It is worth mentioning that the tested torque waveform could not reflect the instantaneous value because of the response hysteresis of the power dynamometer and the interfering of the signal noise.

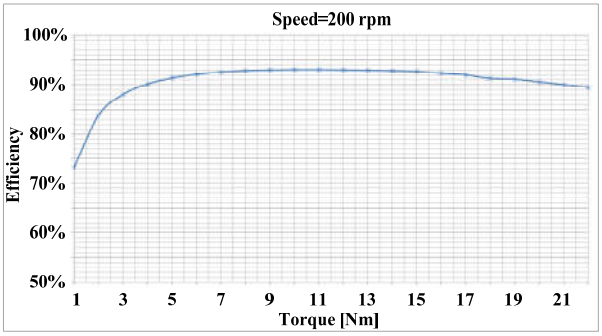

Fig. 5. 23. Measured efficiency under rated speed.

Fig. 5. 23 gives the measured efficiency under various torque and rated speed. It is seen that the average efficiency is about 90% in total torque range. This efficiency is lower than high speed machines, but has competitiveness for direct-drive applications since the precise mechanical reducer such as harmonic gears and RV reducers usually have lower efficiency.

5.5 Conclusion

Aiming for robotic direct-drive applications, one novel dual-PM excitation Vernier machine with short-pitch distributed winding is investigated in this chapter. Some essential issues were investigated. It is concluded that 1) for the proposed machine, the excitation fields with pole-pairs of 2, 22 and 46 have generated the effective back-EMF and constant torque and their contribution percentages are 77%, 20% and 3% respectively; 2) rotor-PM and stator-PM contribute 59% and 41% of the torque respectively; 3) with the 5/6 short-pitch design, the 3rd, 5th and 7th back-EMF harmonics are reduced by 55%, 88% and 88% respectively and the THD of back-EMF is reduced 56.8%; 4) the proposed machine has 1.87 times of the conventional machine due to dual-PM and paralleled magnetic path structure. The tested data has shown that the torque density for the proposed machine could reach 6 Nm/kg under natural ventilation, the THD for back-EMF waveform is less than 4%, the torque ripple is less than 4% and efficiency could reach 90% under rated speed. This machine has great potential in robotic direct drive applications due to its torque density, low-speed characteristic and high efficiency.

Chapter 6 Summary and Further Work

This chapter summarizes the work of this thesis and looks forward to the fulture research topics for stator-PM machines.

6.1 Summary

This thesis investigated the design, analyze and control of novel stator-PM electrical machines. The contents of this thesis are listed as below.

First chapter is the backgrounds and challenges of stator-PM machines.

The backgrounds of this research are introduced. The history and developing trends of four types of stator-PM machines are analyzed and presented. The challenges of stator-PM machines are summarized and the research topics for this thesis are given.

Second chapter is about the biased flux stator-PM machines.

1) The biased flux phenomenon in stator-PM machines is focused, and based on biased flux characteristics the biased flux machine is defined.

2) The advantages of biased flux machine are introduced and what kinds of machines belonging to biased flux machine are summarized.

3) Two design methodologies for biased flux machine are proposed, one is based on magnetic circuit construction and the other one is based on magnetic field modulation theory.

4) One prototype for biased flux machine, naming 12/11 NNSS double stator biased flux machine is built and tested.

5) The novel control for biased flux machines using zero-sequence current is proposed. The implementation of this method by 3D-SVPWM is introduced.

6) The biased flux concept is expanded into other stator-PM machines to eliminate the additional DC exciting windings.

The third chapter is about the doubly complementary machine to improve the PM utilization.

1) To overcome the disadvantages of some stator-PM machines with short-circuit or open-circuit magnetic path, a complementary magnetic path for stator-PM machines is proposed.

3) Based on the complementary magnetic path, one novel doubly complementary machine is proposed and analyzed.

3) The prototype of doubly complementary machine is built and tested. The detailed performances such as back-EMF, torque, power factor and efficiency are measured.

4) The doubly complementary concept has also been applied in one axial flux machine for direct drive applications.

The fourth and fifth chapter is about the high torque density Vernier machines.

1) One novel stator-PM Vernier machine is investigated, the principle is introduced, the combination of stator and rotor teeth is analyzed, the prototype is built and the performances are tested. It is proved that the

torque density for this kind of machines can reach higher than FSCW rotor-PM machines.

2) To meet the large-torque and low-speed application, one dual-PM exciting machine with distributed winding and short-pitch coil is proposed. It is proved that this kind of machine can obtain higher torque density than rotor-PM machine or traditional stator-PM machines.

6.2 Further Work

Although this thesis has done some researches for stator-PM machines, there are many challenges still are still left for future work.

1) For the biased flux machines, by using the biased current, it is true that the exciting flux can be modulated. However, by using the traditional d-axis current control, the exciting flux can also be controlled. Indeed, the biased current control could increase the control freedom, but whether this control has advantage over traditional control still need to be verified. Similarly, whether the hybrid exciting control has advantages over traditional control still need to be verified.

2) It is found that the stator-PM Vernier machine could have much higher torque density than the other stator-PM machines. But the theory behind this phenomenon still needs to be found. Whether there is one general method to compare different machine topologies still needs to be answered, and if there is, what is the method.

3) It is found that the major advantage for stator-PM machines is that they are suitable for linear motion. However, the linear machines have not been studied here.

4) It is found that the dual-PM machines have the largest torque density, how to further improve the torque density for electrical machines still needs future research.

References

[1] W. Lee, D. Han and B. Sarlioglu, "Comparative performance analysis of reference voltage-controlled pulse width modulation for high-speed single-phase brushless dc motor drive," *IEEE. Trans. Power. Electron*., vol. 33, no. 5, pp. 4560-4568, May 2018.

[2] D. Jiang, Q. Li and Z. Shen, "Model predictive PWM for AC motor drives," *IET. Electr. Power. Appl*., vol. 11, no. 5, pp. 815-822, 5 2017.

[3] R. Cao, Y. Jin, M. Lu and Z. Zhang, "Quantitative comparison of linear flux-switching permanent magnet motor with linear induction motor for electromagnetic launch system," *IEEE Trans. Ind. Electron.*, vol. PP, no. 99, pp. 1-1.

[4] D. Carpenter and S. Deleanu, "Parameter determination of synchrnous machine with radial permanent magnets using analytical calculation and standstill tests," *2012 25th IEEE Canadian Conference on Electrical and Computer Engineering (CCECE)*, Montreal, QC, 2012, pp. 1-6.

[5] S. G. Min, G. Bramerdorfer and B. Sarlioglu, "Analytical modeling and optimization for electromagnetic performances of fractional-slot pm brushless machines," *IEEE Trans. Ind. Electron.*, vol. 65, no. 5, pp. 4017-4027, May 2018.

[6] T. Raminosoa *et al*., "Sinusoidal reluctance machine with dc winding: an attractive non-permanent-magnet option," *IEEE Trans. Ind. Appl.*, vol. 52, no. 3, pp. 2129-2137, May-June 2016.

[7] M. Cheng, W. Hua, J. Zhang and W. Zhao, "Overview of stator-permanent magnet brushless machines," *IEEE Trans. Ind. Electron*., vol. 58, no. 11, pp. 5087-5101, Nov. 2011.

[8] Z. Q. Zhu and D. Evans, "Overview of recent advances in innovative electrical machines — with particular reference to magnetically geared switched flux machines," *Electrical Machines and Systems (ICEMS), 2014 17th International Conference on*, Hangzhou, 2014, pp. 1-10.

[9] C. Cui, G. Liu and K. Wang, "A novel drive method for high-speed brushless DC motor operating in a wide range," *IEEE Trans. Power. Electron*., vol. 30, no. 9, pp. 4998-5008, Sept. 2015.

[10] S. Niu, S. L. Ho, and W. N. Fu, “A novel direct-drive dual-structure permanent magnet machine,” *IEEE Trans. Magn*., vol. 46, no. 6, pp. 2036-2039, 2010.

[11] Liao Y, Liang F, Lipo T A. "A novel permanent magnet motor with doubly salient structure," *IEEE Trans. Ind. Appl.*, vol. 31, no. 5, pp. 1069-1074,1995.

[12] B. C. Mecrow, "New winding configurations for doubly salient reluctance machines," *IEEE Trans. Ind. Appl.* , vol. 32, no. 6, pp. 1348-1356, Nov./Dec. 1996.

[13] Li Yongbin, Chunting Chris Mi. "Doubly salient permanent-magnet machine with skewed rotor and six-state commutating mode," *IEEE Trans. Magn.*, vol. 43, no. 9, pp.3623-3629,2007.

[14] Sekhar Babu1 A R C, Rajagopal K R. FE, "Analysis of multiphase doubly salient permanent magnet motors," *IEEE Trans. Magn.*, vol. 41, no. 10, pp. 3955-3957, 2005.

[15] Z. Q. Zhu, Z. Wu, D. Evans, and W. Chu, "Novel electrical machines having separate PM excitation stator", *IEEE Trans. Magn*., vol. 51, no. 4, pp. 1-9, April 2015.

[16] M. Y. Lin, M. Cheng, and E. Zhou, "Design and performance analysis of new 12/8-pole doubly salient permanent-magnet motor," in *Proc. 6th Int. Conf. Electron. Mach. Syst.*, vol. 1. Beijing, China, Nov. 2003, pp. 21–25.

[17] Y. Wang, Z. Zhang, R. Liang, W. Yuan and Y. Yan, "Torque density improvement of doubly salient electromagnetic machine with asymmetric current control," *Trans. Ind. Electron*., vol. 63, no. 12, pp. 7434-7443, Dec. 2016.

[18] Z. Z. Wu, Z. Q. Zhu and J. T. Shi, "Novel doubly salient permanent magnet machines with partitioned stator and iron pieces rotor," *IEEE Trans. Magn.*, vol. 51, no. 5, pp. 1-12, May 2015.

[19] L. Gu, W. Wang, B. Fahimi and M. Kiani, "A novel high energy density double salient exterior rotor permanent magnet machine," *IEEE Trans. Magn.*, vol. 51, no. 3, pp. 1-4, March 2015.

[20] G. J. Li, X. Ojeda, E. Hoang, M. Gabsi and C. Balpe, "Design of double salient interior permanent magnet machine based on mutually coupled reluctance machine for increasing the torque density and flux-weakening capability," *2010 IEEE International Symposium on Industrial Electronics*, Bari, 2010, pp. 1253-1258.

[21] F. Leonardi, T. Matsuo, Y. Li, T. A. Lipo, and P. McCleer, "Design considerations and test results for a doubly salient PM motor with flux control," in *Proc. Conf. Rec. IEEE Ind. Appl. Conf., 31st IAS Annu*. Meeting, Oct. 1996, pp. 458–463.

[22] I. A. A. Afinowi, Z. Q. Zhu, Y. Guan, J. C. Mipo, P. Farah, "Hybrid-excited doubly salient synchronous machines with permanent magnets between adjacent salient stator poles," *IEEE Trans.Magn,* vol. 51, no. 10, Oct. 2015.

[23] Z. Zhang, Y. Tao, and Y. Yan, "Investigation of a new topology of hybrid excitation doubly salient brushless DC generator," *IEEE Trans. Ind. Electron.*, vol. 59, no. 6, pp. 2550–2556, Jun. 2012.

[24] H. Liu, L. Quan, X. Zhu, D. Chen and B. Zhang, "Dual-mode operations of new stator-permanent-magnet double salient flux memory motor drive," *2011 International Conference on Electrical Machines and Systems*, Beijing, 2011, pp. 1-4.

[25] Boldera. I, Serban. E and Babau. R, “Flux reversal stator-PM single-phase Generator with controlled DC output”. Record of OPTIM-96, Brasov, Romania, 1996, pp. 1123-1137.

[26] S. E. Rauch and L. J. Johnson, "Design principles of flux-switch alternators [includes discussion]," in *Transactions of the American Institute of Electrical Engineers. Part III: Power Apparatus and Systems*, vol. 74, no. 3, Jan. 1955.

[27] R. P. Deodhar, S. Andersson, I. Boldea and T. J. E. Miller, "The flux-reversal machine: a new brushless doubly-salient permanent-magnet machine," *IEEE Trans. Ind. Appl.*, vol. 33, no. 4, pp. 925-934, Jul/Aug 1997.

[28] C. Wang, S. A. Nasar and I. Boldea, "Three-phase flux reversal machine (FRM)," in *IEE Proceedings - Electric Power Applications*, vol. 146, no. 2, pp. 139-146, Mar 1999.

[29] T. H. Kim, "A study on the design of an inset-permanent-magnet-type flux-reversal machine," *IEEE Trans.Magn.*, vol. 45, no. 6, pp. 2859-2862, June 2009.

[30] D. S. More and B. G. Fernandes, "Modelling and performance of three-phase 6/14 pole flux reversal machine," *IET. Electr. Power. Appl.*, vol. 7, no. 2, pp. 131-139, Feb. 2013.

[31] I. Boldea, Jichun Zhang and S. A. Nasar, "Theoretical characterization of flux reversal machine in low-speed servo drives-the pole-PM configuration," *IEEE Trans. Ind. Appl.*, vol. 38, no. 6, pp. 1549-1557, Nov/Dec 2002.

[32] D. Li, Y. Gao, R. Qu, J. Li, Y. Huo and H. Ding, "Design and analysis of a flux reversal machine with evenly distributed permanent magnets," *IEEE Trans. Ind. Appl.*, vol. 54, no. 1, pp. 172-183, Jan.-Feb. 2018.

[33] D. S. More and B. G. Fernandes, "Analysis of flux-reversal machine based on fictitious electrical gear," *IEEE Trans.Energy. Convers.*, vol. 25, no. 4, pp. 940-947, Dec. 2010.

[34] Z. Wu, Z. Q. Zhu and H. Zhan, "Comparative analysis of partitioned stator flux reversal pm machine and magnetically geared machine operating in stator-pm and rotor-pm modes," *IEEE Trans.Energy. Convers.*, vol. 32, no. 3, pp. 903-917, Sept. 2017.

[35] L. Xu, G. Liu, W. Zhao, J. Ji, H. Zhou and T. Jiang, "Design and analysis of a new linear wound-field flux reversal machine based on magnetic gear effect," *IEEE Trans.Magn.*, vol. 51, no. 11, pp. 1-4, Nov. 2015.

[36] Z. Z. Wu, Z. Q. Zhu and H. L. Zhan, "Comparative analysis of partitioned stator flux reversal pm machines having fractional-slot nonoverlapping and integer-slot overlapping windings," *IEEE Trans.Energy. Convers.*, vol. 31, no. 2, pp. 776-788, June 2016.

[37] Z. Z. Wu and Z. Q. Zhu, "Partitioned stator flux reversal machine with consequent-pole pm stator," *IEEE Trans.Energy. Convers.*, vol. 30, no. 4, pp. 1472-1482, Dec. 2015.

[38] D. S. More and B. G. Fernandes, "Novel three phase flux reversal machine with full pitch winding," *2007 7th Internatonal Conference on Power Electronics*, Daegu, 2007, pp. 1007-1012.

[39] D. S. More and B. G. Fernandes, "Power density improvement of three phase flux reversal machine with distributed winding," *IET. Electr. Power. Appl.*, vol. 4, no. 2, pp. 109-120, February 2010.

[40] Y. Yang, J. Zhang, L. Ma, X. Wang and N. Wang, "The electromagnetic performance calculation and comparison of flux reversal machine with different winding topologies," *2014 17th International Conference on Electrical Machines and Systems (ICEMS)*, Hangzhou, 2014, pp. 605-609.

[41] M. Ghasemian, F. Tahami and G. Rezazadeh, "A comparative analysis of permanent magnet flux reversal generators with distributed and concentrated winding," *IECON 2017 - 43rd Annual Conference of the IEEE Industrial Electronics Society*, Beijing, 2017, pp. 1657-1661.

[42] D. S. More, H. Kalluru and B. G. Fernandes, "d-q equivalent circuit representation of three-phase flux reversal machine with full pitch winding," *2008 IEEE Power Electronics Specialists Conference*, Rhodes, 2008, pp. 1208-1214.

[43] W. Hua, X. Zhu and Z. Wu, "Influence of coil pitch and stator-slot/rotor-pole combination on back-emf harmonics in flux-reversal permanent magnet machines," *IEEE Trans.Energy. Convers.*, vol. PP, no. 99, pp. 1-1.

[44] C. Shi, R. Qu, Q. B. Kou, D. Li, Y. Gao and Y. Zhou, "A novel hts flux-reversal linear permanent magnet machine with a lower number of mover teeth and higher thrust density," *IEEE Trans.Applied. Superconduc.*, vol. PP, no. 99, pp. 1-1.

[45] W. Li, K. T. Chau, T. W. Ching and C. Liu, "A phase-decoupled flux-reversal linear generator for low-speed oscillatory energy conversion using impedance matching strategy," *IEEE Trans. Ind. Electron.*, vol. PP, no. 99, pp. 1-1.

[46] Q. Wang, W. Huang and D. Dong, "Force ripples suppression of tubular transverse flux and flux reversal linear permanent magnet motor based on ADRC," *2017 20th International Conference on Electrical Machines and Systems (ICEMS)*, Sydney, NSW, 2017, pp. 1-5.

[47] K. Guo, S. Fang, H. Lin, H. Yang, Y. Huang and P. Jin, "3-D analytical analysis of magnetic field of flux reversal linear-rotary permanent-magnet actuator," *IEEE Trans.Magn.*, vol. 53, no. 6, pp. 1-5, June 2017.

[48] J. Luo, B. Kou, Y. Zhou and L. Zhang, "Analysis and design of an E-core transverse-flux flux-reversal linear motor," *2016 19th International Conference on Electrical Machines and Systems (ICEMS)*, Chiba, 2016, pp. 1-5.

[49] B. Kou, J. Luo, X. Yang and L. Zhang, "Modeling and analysis of a novel transverse-flux flux-reversal linear motor for long-stroke application," *IEEE Trans. Ind. Electron.*, vol. 63, no. 10, pp. 6238-6248, Oct. 2016.

[50] W. Li, K. T. Chau and T. W. Ching, "A six-phase transverse-flux-reversal linear machine for low-speed reciprocating power generation," *2015 IEEE International Electric Machines & Drives Conference (IEMDC)*, Coeur d'Alene, ID, 2015, pp. 618-623.

[51] S. U. Chung, H. J. Lee and S. M. Hwang, "A novel design of linear synchronous motor using frm topology," *IEEE Trans.Magn.*, vol. 44, no. 6, pp. 1514-1517, June 2008.

[52] S. U. Chung, K. W. Kim, J. W. Kim, J. Y. Lee and B. C. Woo, "Dynamic simulation and experimental validation of flux reversal linear synchronous motor," *Digests of the 2010 14th Biennial IEEE Conference on Electromagnetic Field Computation*, Chicago, IL, 2010, pp. 1-1.

[53] A. L. Shuraiji, Z. Q. Zhu and Q. F. Lu, "A novel partitioned stator flux reversal permanent magnet linear machine," *IEEE Trans.Magn.*, vol. 52, no. 1, pp. 1-6, Jan. 2016.

[54] X. Zhu, W. Hua and Z. Wu, "Cogging torque suppression in flux-reversal permanent magnet machines," *IET. Electr. Power. Appl.*, vol. 12, no. 1, pp. 135-143, 1 2018.

[55] X. Zhu and W. Hua, "An improved configuration for cogging torque reduction in flux-reversal permanent magnet machines," *IEEE Trans.Magn.*, vol. 53, no. 6, pp. 1-4, June 2017.

[56] Tae Heoung Kim, Sung Hong Won, Ki Bong and Ju Lee, "Reduction of cogging torque in flux-reversal machine by rotor teeth pairing," *IEEE Trans.Magn.*, vol. 41, no. 10, pp. 3964-3966, Oct. 2005.

[57] Y. Gao, R. Qu, D. Li and J. Li, "Torque performance analysis of three-phase flux reversal machines," *IEEE Trans. Ind. Appl.*, vol. 53, no. 3, pp. 2110-2119, May-June 2017.

[58] E. Hoang,A. H. Ben·Ahmed，J. Lucidarme. “Switching flux permanent magnet polyphased synchronous machines," The 7th European Conference on Power Electronic and Applications EPE’97-1997, 903-908.

[59] Z. Q. Zhu, J. T. Chen, Y. Pang, D. Howe, S. Iwasaki and R. Deodhar, "Analysis of a novel multi-tooth flux-switching pm brushless ac machine for high torque direct-drive applications," *IEEE Trans.Magn.*, vol. 44, no. 11, pp. 4313-4316, Nov. 2008.

[60] Y. J. Zhou and Z. Q. Zhu, "Torque density and magnet usage efficiency enhancement of sandwiched switched flux permanent magnet machines using v-shaped magnets," *IEEE Trans.Magn.*, vol. 49, no. 7, pp. 3834-3837, July 2013.

[61] A. Gandhi and L. Parsa, "Double-rotor flux-switching permanent magnet machine with yokeless stator," *IEEE Trans.Energy. Convers.*, vol. 31, no. 4, pp. 1267-1277, Dec. 2016.

[62] D. Kim, H. Hwang, S. Bae and C. Lee, "Analysis and design of a double-stator flux-switching permanent magnet machine using ferrite magnet in hybrid electric vehicles," *IEEE Trans.Magn.*, vol. 52, no. 7, pp. 1-4, July 2016.

[63] L. Shao, W. Hua, Z. Q. Zhu, X. Zhu, M. Cheng and Z. Wu, "A novel flux-switching permanent magnet machine with overlapping windings," *IEEE Trans.Energy. Convers.*, vol. 32, no. 1, pp. 172-183, March 2017.

[64] Z. Wang, W. Xu, G. Lei and J. Zhu, "Multilayer winding effect on performance of flux-switching permanent magnet machines," *IEEE Trans.Applied. Superconduc.*, vol. 26, no. 7, pp. 1-4, Oct. 2016.

[65] Y. Li, D. Bobba and B. Sarlioglu, "A novel 6/4 flux-switching permanent magnet machine designed for high-speed operations," *IEEE Trans.Magn.*, vol. 52, no. 8, pp. 1-9, Aug. 2016.

[66] S. M. Kazemi Sangdehi, S. E. Abdollahi and S. A. Gholamian, "Analysis of a novel transverse laminated rotor flux switching machine," *IEEE Trans.Energy. Convers.*, vol. PP, no. 99, pp. 1-1.

[67] L. Shao *et al*., "Influence of rotor-pole number on electromagnetic performance in 12-phase redundant switched flux permanent magnet machines for wind power generation," *IEEE Trans. Ind. Appl.*, vol. 53, no. 4, pp. 3305-3316, July-Aug. 2017.

[68] Z. Xiang, L. Quan, X. Zhu, J. Huang and D. Fan, "Investigation of optimal split ratio in brushless dual-rotor flux-switching permanent magnet machine considering power allocation," *IEEE Trans.Magn.*, vol. PP, no. 99, pp. 1-4.

[69] W. Fei, P. C. K. Luk, D. M. Miao and J. X. Shen, "Investigation of torque characteristics in a novel permanent magnet flux switching machine with an outer-rotor configuration," *IEEE Trans.Magn.*, vol. 50, no. 4, pp. 1-10, April 2014.

[70] F. Li, W. Hua, M. Tong, G. Zhao and M. Cheng, "Nine-phase flux-switching permanent magnet brushless machine for low-speed and high-torque applications," *IEEE Trans.Magn.*, vol. 51, no. 3, pp. 1-4, March 2015.

[71] C. H. T. Lee, J. L. Kirtley and M. Angle, "A Partitioned-stator flux-switching permanent-magnet machine with mechanical flux adjusters for hybrid electric vehicles," *IEEE Trans.Magn.*, vol. 53, no. 11, pp. 1-7, Nov. 2017.

[72] H. Hua and Z. Q. Zhu, "Novel partitioned stator hybrid excited switched flux machines," *IEEE Trans.Energy. Convers.*, vol. 32, no. 2, pp. 495-504, June 2017.

[73] H. Yang *et al*., "Design synthesis of switched flux hybrid-permanent magnet memory machines," *IEEE Trans.Energy. Convers.*, vol. 32, no. 1, pp. 65-79, March 2017.

[74] W. Ding, Y. Hu, T. Wang and S. Yang, "Comprehensive research of modular e-core stator hybrid-flux switched reluctance motors with segmented and nonsegmented rotors," *IEEE Trans.Energy. Convers.*, vol. 32, no. 1, pp. 382-393, March 2017.

[75] W. Hua, P. Su, M. Tong and J. Meng, "Investigation of a five-phase e-core hybrid-excitation flux-switching machine for ev and hev applications," *IEEE Trans. Ind. Appl.*, vol. 53, no. 1, pp. 124-133, Jan.-Feb. 2017.

[76] H. Yang *et al*., "Novel high-performance switched flux hybrid magnet memory machines with reduced rare-earth magnets," *IEEE Trans. Ind. Appl.*, vol. 52, no. 5, pp. 3901-3915, Sept.-Oct. 2016.

[77] H. Hua and Z. Q. Zhu, "Novel hybrid-excited switched-flux machine having separate field winding stator," *IEEE Trans.Magn.*, vol. 52, no. 7, pp. 1-4, July 2016.

[78] D. Kim, H. Hwang, S. Bae and C. Lee, "Analysis and design of a double-stator flux-switching permanent magnet machine using ferrite magnet in hybrid electric vehicles," *IEEE Trans.Magn.*, vol. 52, no. 7, pp. 1-4, July 2016.

[79] A. Dupas, S. Hlioui, E. Hoang, M. Gabsi and M. Lecrivain, "Investigation of a new topology of hybrid-excited flux-switching machine with static global winding: experiments and modeling," *IEEE Trans. Ind. Appl.*, vol. 52, no. 2, pp. 1413-1421, March-April 2016.

[80] W. Zhang, X. Liang, M. Lin, L. Hao and N. Li, "Design and analysis of novel hybrid-excited axial field flux-switching permanent magnet machines," *IEEE Trans.Applied. Superconduc.*, vol. 26, no. 4, pp. 1-5, June 2016.

[81] X. Zhu, W. Hua, Z. Wu, W. Huang, H. Zhang and M. Cheng, "Analytical approach for cogging torque reduction in flux-switching permanent magnet machines based on magnetomotive force-permeance model," *IEEE Trans. Ind. Electron.*, vol. 65, no. 3, pp. 1965-1979, March 2018.

[82] D. Xu, M. Lin, X. Fu, L. Hao, W. Zhang and N. Li, "Cogging torque reduction of a hybrid axial field flux-switching permanent-magnet machine with three methods," *IEEE Trans.Applied. Superconduc.*, vol. 26, no. 4, pp. 1-5, June 2016.

[83] L. Hao, M. Lin, D. Xu, N. Li and W. Zhang, "Analysis of cogging torque reduction techniques in axial-field flux-switching permanent-magnet machine," *IEEE Trans.Applied. Superconduc.*, vol. 26, no. 4, pp. 1-5, June 2016.

[84] L. Hao, M. Lin, D. Xu, N. Li and W. Zhang, "Cogging torque reduction of axial-field flux-switching permanent magnet machine by rotor tooth notching," *IEEE Trans.Magn.*, vol. 51, no. 11, pp. 1-4, Nov. 2015.

[85] C. Sikder, I. Husain and W. Ouyang, "Cogging torque reduction in flux-switching permanent-magnet machines by rotor pole shaping," *IEEE Trans. Ind. Appl.*, vol. 51, no. 5, pp. 3609-3619, Sept.-Oct. 2015.

[86] L. Hao, M. Lin, D. Xu and W. Zhang, "Cogging torque reduction of axial field flux-switching permanent magnet machine by adding magnetic bridge in stator tooth," *IEEE Trans.Applied. Superconduc.*, vol. 24, no. 3, pp. 1-5, June 2014.

[87] S. E. Abdollahi and S. Vaez-Zadeh, "Reducing cogging torque in flux switching motors with segmented rotor," *IEEE Trans.Magn.*, vol. 49, no. 10, pp. 5304-5309, Oct. 2013.

[88] J. Yan, H. Lin, Y. Feng, Z. Q. Zhu, P. Jin and Y. Guo, "Cogging torque optimization of flux-switching transverse flux permanent magnet machine," *IEEE Trans.Magn.*, vol. 49, no. 5, pp. 2169-2172, May 2013.

[89] D. Wang, X. Wang and S. Y. Jung, "Reduction on cogging torque in flux-switching permanent magnet machine by teeth notching schemes," *IEEE Trans.Magn.*, vol. 48, no. 11, pp. 4228-4231, Nov. 2012.

[90] Q. Liu *et al*., "Cogging force reduction of double-sided linear flux-switching permanent magnet machine for direct drives," *IEEE Trans.Magn.*, vol. 49, no. 5, pp. 2275-2278, May 2013.

[91] Linear L. Huang, M. Hu, J. Liu, H. Yu, C. Zeng and Z. Chen, "Electromagnetic design of a 10-kw-class flux-switching linear superconducting hybrid excitation generator for wave energy conversion," *IEEE Trans.Applied. Superconduc.*, vol. 27, no. 4, pp. 1-6, June 2017.

[92] R. Cao, Y. Jin, Y. Zhang and M. Cheng, "A new double-sided hts flux-switching linear motor with series magnet circuit," *IEEE Trans.Applied. Superconduc.*, vol. 26, no. 7, pp. 1-5, Oct. 2016.

[93] W. Zhong, H. Yu, M. Hu, Z. Shi and Q. Liu, "Study on a novel pseudo-six-phase linear flux-switching permanent-magnet machine for direct drive," *IEEE Trans.Applied. Superconduc.*, vol. 26, no. 4, pp. 1-4, June 2016.

[94] L. Huang, J. Liu, H. Yu, R. Qu, H. Chen and H. Fang, "Winding configuration and performance investigations of a tubular superconducting flux-switching linear generator," *IEEE Trans.Applied. Superconduc.*, vol. 25, no. 3, pp. 1-5, June 2015.

[95] A. Gandhi and L. Parsa, "Thrust optimization of a flux-switching linear synchronous machine with yokeless translator," *IEEE Trans.Magn.*, vol. 49, no. 4, pp. 1436-1443, April 2013.

[96] C. F. Wang and J. X. Shen, "A method to segregate detent force components in permanent-magnet flux-switching linear machines," *IEEE Trans.Magn.*, vol. 48, no. 5, pp. 1948-1955, May 2012.

[97] M. J. Jin, C. F. Wang, J. X. Shen and B. Xia, "A modular permanent-magnet flux-switching linear machine with fault-tolerant capability," *IEEE Trans.Magn.*, vol. 45, no. 8, pp. 3179-3186, Aug. 2009.

[98] C. F. Wang, J. X. Shen, Y. Wang, L. L. Wang and M. J. Jin, "A new method for reduction of detent force in permanent magnet flux-switching linear motors," *IEEE Trans.Magn.*, vol. 45, no. 6, pp. 2843-2846, June 2009.

[99] Y. Shen, Q. Lu, H. Li, J. Cai, X. Huang and Y. Fang, "Analysis of a novel double-sided yokeless multitooth linear switched-flux pm motor," *IEEE Trans. Ind. Electron.*, vol. 65, no. 2, pp. 1837-1845, Feb. 2018.

[100] Q. Lu, Y. Yao, J. Shi, Y. Shen, X. Huang and Y. Fang, "Design and performance investigation of novel linear switched flux pm machines," *IEEE Trans. Ind. Appl.*, vol. 53, no. 5, pp. 4590-4602, Sept.-Oct. 2017.

[101] Z. Z. Wu and Z. Q. Zhu, "Analysis of air-gap field modulation and magnetic gearing effects in switched flux permanent magnet machines," *IEEE Trans.Magn.*, vol. 51, no. 5, pp. 1-12, May 2015.

[102] Z. Z. Wu and Z. Q. Zhu, "Analysis of magnetic gearing effect in partitioned stator switched flux pm machines," *IEEE Trans.Energy. Convers.*, vol. 31, no. 4, pp. 1239-1249, Dec. 2016.

[103] Y. Du *et al*., "Comparison of flux-switching pm motors with different winding configurations using magnetic gearing principle," *IEEE Trans.Magn.*, vol. 52, no. 5, pp. 1-8, May 2016.

[104] Z. Q. Zhu and D. Evans, "Overview of recent advances in innovative electrical machines — With particular reference to magnetically geared switched flux machines," *2014 17th International Conference on Electrical Machines and Systems (ICEMS)*, Hangzhou, 2014, pp. 1-10.

[105] K. Atallah and D. Howe, "A novel high-performance magnetic gear," *IEEE Trans.Magn.*, vol. 37, no. 4, pp. 2844-2846, Jul 2001.

[106] M. Johnson, M. C. Gardner and H. A. Toliyat, "Design comparison of ndfeb and ferrite radial flux surface permanent magnet coaxial magnetic gears," *IEEE Trans. Ind. Appl.*, vol. PP, no. 99, pp. 1-1.

[107] G. Kronacher, "Design, performance and application of the Vernier resolver," *in The Bell System Technical Journal*, vol. 36, no. 6, pp. 1487-1500, Nov. 1957.

[108] C. H. Lee, "Vernier motor and its design," *IEEE Trans. Power App*. Syst., vol. 82, no. 66, pp. 343-349, June 1963.

[109] K. C. Mukherji and A. Tustin, "Vernier reluctance motor," *in Electrical Engineers, Proceedings of the Institution of*, vol. 121, no. 9, pp. 965-974, September 1974.

[110] S. Jia, R. Qu, J. Li, D. Li and H. Lu, "Design considerations of stator DC-winding excited Vernier reluctance machines based on the magnetic gear effect," *IEEE Trans. Ind. Appl.*, vol. 53, no. 2, pp. 1028-1037, March-April 2017.

[111] S. Jia, R. Qu, J. Li and D. Li, "Principles of stator DC winding excited Vernier reluctance machines," *IEEE Trans. Energy Convers.*, vol. 31, no. 3, pp. 935-946, Sept. 2016.

[112] S. Tabi, A. Tounzi and F. Piriou, "Study of a stator current excited Vernier reluctance machine," *IEEE Trans. Energy Convers*., vol. 21, no. 4, pp. 823-831, Dec. 2006.

[113] A. Toba and T. A. Lipo, "Generic torque-maximizing design methodology of permanent magnet Vernier machine," *Electric Machines and Drives, 1999. International Conference IEMD '99, Seattle, WA*, 1999, pp. 522-524.

[114] S. L. Ho, S. Niu, and W. N. Fu, “Design and comparison of Vernier permanent magnet machines,” IEEE Trans. Magn., vol. 47, no. 10, pp. 3280-3283, 2011.

[115] D. Jang and J. Chang, "Effects of flux modulation poles on the radial magnetic forces in surface-mounted permanent-magnet Vernier machines," *IEEE Trans. Magn.*, vol. 53, no. 6, pp. 1-4, June 2017.

[116] Y. Chen, W. Fu and X. Weng, "A concept of general flux-modulated electric machines based on a unified theory and its application to developing a novel doubly-fed dual-stator motor," *IEEE Trans. Ind. Electron*., vol. PP, no. 99, pp. 1-1.

[117] S. Niu, S. L. Ho, and W. N. Fu, “A novel direct-drive dual-structure permanent magnet machine,” *IEEE Trans. Magn.*, vol. 46, no. 6, pp. 2036-2039, 2010.

[118] S. U. Chung, J. W. Kim, B. C. Woo, D. K. Hong, J. Y. Lee and D. H. Koo, "A novel design of modular three-phase permanent magnet Vernier machine with consequent pole rotor," *IEEE Trans. Magn*., vol. 47, no. 10, pp. 4215-4218, Oct. 2011.

[119] D. Li, R. Qu, J. Li and W. Xu, "Consequent-pole toroidal-winding outer-rotor Vernier permanent-magnet machines," *IEEE Trans. Ind. Appl*., vol. 51, no. 6, pp. 4470-4481, Nov.-Dec. 2015.

[120] S. Jia, R. Qu, J. Li, D. Li and W. Kong, "A stator-PM consequent-pole Vernier machine with hybrid excitation and dc-biased sinusoidal current," *IEEE Trans. Magn.*, vol. 53, no. 6, pp. 1-4, June 2017.

[121] S. Jia *et al*., "Hybrid excitation stator pm vernier machines with novel dc-biased sinusoidal armature current," *IEEE Trans. Ind. Appl.*, vol. PP, no. 99, pp. 1-1.

[122] W. Zhao, J. Zheng, J. Wang, G. Liu, J. Zhao and Z. Fang, "Design and analysis of a linear permanent-magnet Vernier machine with improved force density," *IEEE Trans. Ind. Electron*., vol. 63, no. 4, pp. 2072-2082, April 2016.

[123] X. Liu, C. Zou, Y. Du and F. Xiao, "A linear consequent pole stator permanent magnet vernier machine," *2014 17th International Conference on Electrical Machines and Systems (ICEMS), Hangzhou,* 2014, pp. 1753-1756.

[124] F. Xiao, Y. Du, Y. Wang, M. Chen, T. W. Ching and X. Liu, "Modeling and Analysis of a Linear Stator Permanent-Magnet Vernier HTS Machine," *IEEE Trans.Applied. Superconduc.*, vol. 25, no. 3, pp. 1-4, June 2015.

[125] T. Yao, W. Zhao, F. Bian, L. Chen and X. Zhu, "Design and analysis of a novel modular-stator tubular permanent-magnet vernier motor," *IEEE Trans.Applied. Superconduc.*, vol. PP, no. 99, pp. 1-1.